Control of nanometric Copper and Cobalt layers by electrodeposition for the metallization used in microelectronic interconnections

Amine Lakhdari

Thèse de doctorat

NNT : 2021UPAST075

université PARIS-SACLAY

Maitrise de l'électrodépôt de couches nanométriques de Cuivre et Cobalt pour la métallisation des interconnexions en microélectronique

Control of nanometric copper and cobalt layers by electrodeposition for the metallization used in microelectronic interconnections

Thèse de doctorat de l'université Paris-Saclay

École doctorale n° 573 Interfaces : matériaux, systèmes, usages
Spécialité du doctorat : Chimie
Unité de recherche : Université Paris-Saclay, UVSQ, CNRS, Institut Lavoisier de Versailles, 78000, Versailles, France
Référent : Université de Versailles-Saint-Quentin-en-Yvelines

Thèse présentée et soutenue à Paris-Saclay, le 15/04/2021, par

Amine LAKHDARI

Composition du Jury

Frédéric KANOUFI Directeur de recherche, ITODYS	Président
Paul-Henri HAUMESSER Chercheur, CEA-Leti	Rapporteur
Daniel LINCOT Directeur de recherche, CNRS	Rapporteur
Laure FILLAUD Maître de conférences, Sorbonne université	Examinatrice

Direction de la thèse

Anne-Marie GONCALVES Maître de conférences, UVSQ, ILV	Directrice de thèse
Dominique SUHR R&D technical Fellow, aveni	Co-Encadrant
Arnaud ETCHEBERRY Directeur de recherche émérite, ILV	Invité

À mes Parents

À mon grand-père

Remerciements

Ce travail de thèse a été réalisé sur le site de l'entreprise aveni et sur le site de l'Institut Lavoisier de Versailles.

Je tiens à remercier en premier lieu ma directrice de thèse Anne-Marie GONCALVES et mon encadrant Dominique SUHR. Merci à Anne-Marie de m'avoir choisi et confié cette thèse et pour son soutien continu durant ces trois années. Je la remercie aussi pour son implication & sa disponibilité, pour m'avoir accueilli au sein de l'ILV et m'avoir guidé dans le monde de l'électrochimie. Je tiens également à te remercier Anne-Marie pour tous tes conseils et de m'avoir motivé à combiner la rédaction et la recherche d'emploi. Ensuite, je tiens à remercier Dominique de m'avoir transmis son amour de la recherche et développement et la rigueur. Je te remercie pour ton suivi tout au long de cette thèse, ta disponibilité permanente pour répondre à mes questions et à surmonter toutes les problématiques scientifiques et techniques. Merci aussi à vous pour votre bonne humeur et votre bienveillance, vous êtes comme une famille pour moi.

J'ai eu aussi un excellent jury de thèse : Daniel LINCOT, Paul-Henri HAUMESSER, Laure FILLAUD et Frédéric KANOUFI, avec qui j'ai eu l'honneur d'échanger ; je les remercie pour leurs apports à ce manuscrit.

Je souhaite adresser mes remerciements à toute l'équipe EPI de l'ILV pour l'excellente ambiance de travail, pour les discussions scientifiques et amicales à la plateforme CEFS2 : Mathieu FREGNAUX, Muriel BOUTTEMY, Damien AUREAU, Solène BECHU, Nathalie SIMON et Jackie VIGNERON. Un remerciement spécial à Arnaud ETCHEBERRY pour tout le savoir qui m'a transmis dès le premier jour de mon stage de M2 et de m'avoir formé à l'utilisation de beaucoup d'équipements. Je te remercie aussi pour ton soutien et tes conseils.

Un grand merci à l'équipe des doctorants : Cendra RAKOTOARIMANANA, Jean-Claude MELEDJE et Arcadie FLUOR. Merci pour votre soutien.

Une deuxième partie de ma thèse a été réalisée au sein de aveni, Je voudrais remercier tous les membres : Frédéric RAYNAL, Vincent MEVELLEC, Louis CAILLARD et Bruno MOREL. Je voudrais remercier spécialement Mikaïlou THIAM avec qui j'ai beaucoup travaillé. Merci à vous pour l'occasion que vous m'aviez donnée pour intégrer la best team aveni.

En dehors du cadre professionnel, je remercie mes amis : Amine CHEKIREB, Amine GUERBOUKHA, Karim MEDJOUBI, Raid BAGHDOUCHE et Brahim GUERIANE pour leur soutien aussi bien durant les moments difficiles de cette thèse que dans les moments de joie, merci à vous.

Plus que tout, je remercie ma grande famille et ma belle-famille pour leurs soutien et encouragements à chaque étape de ma vie. Un remerciement spécial à Djamel, Sonia, Imad, Walid, Hadjira et Saadia.

Je remercie beaucoup mes frères, d'être toujours présents à mes côtés : Karim, Adel, Ayoub et Ramdane. Vous êtes ma force !

A ma Binôme : Inès ma femme, merci pour toutes les nuits blanches que tu as passé à mes côtés en période de rédaction, merci pour tes motivations. Merci d'avoir toujours cru en moi, de m'avoir toujours épaulé, tu es mon inspiration !

Mes parents ! Papa je te remercie pour ton encouragement continu, tes motivations et d'avoir toujours cru en moi. Maman je te serai éternellement reconnaissant pour tout ce que tu as fait pour moi. Merci pour ton acharnement lors de mes études. Merci de m'avoir toujours motivé, soutenu dans mes choix et su me recadrer quand j'avais tort. Merci d'être toujours présente à mes côtés. Tu es la lumière de ma vie !

Summary

GENERAL INTRODUCTION 8

CHAPTER I THEORETICAL BACKGROUND OF METALLIZATION IN INTERCONNECTS... 18

I.1 INTRODUCTION 19

I.2 MICROELECTRONICS 20

I.2.1. Interconnects scaling and limitations 20

I.2.1.1 Temporary solutions of overcoming these limitations 22

I.2.1.2 Interconnection network organization 23

I.2.1.3 Damascene process 25

I.2.2. Electromigration 28

I.3 METALLIZATION 34

I.3.1. Electrochemical cells 34

I.3.2. Electroplating and film growth 35

I.3.2.1 Deposition techniques 37

I.3.2.2 Film growth 39

I.3.2.3 Effect of additives 40

I.3.2.4 Factor effecting electroplating 43

I.4 REFERENCES 46

CHAPTER II COBALT ELECTROCHEMICAL INVESTIGATION AND MECHANISM COMPREHENSION 48

II.1 INTRODUCTION 49

II.2 COBALT ELECTROCHEMICAL INVESTIGATION 52

II.2.1. Cyclic voltammetry 52

II.2.2. Cobalt concentration impact 60

II.3 COBALT ELECTRODEPOSITION MECHANISM 70

II.3.1. Current efficiency 70

II.3.2. Nucleation and growth 74

II.3.3. Bath temperature impact 77

II.4 CONCLUSION 79

II.5 REFERENCES 81

CHAPTER III COBALT THIN FILM BEHAVIOR 84

III.1 INTRODUCTION 85

III.2 ANNEALING AND BATH PH IMPACT ON DEPOSITED COBALT FILM 88

III.2.1. Impact of Annealing 89

III.2.2. Impact of bath pH 92

III.3 COBALT FILM REACTIVITY TOWARD AIR-EXPOSURE 94

III.4 COBALT FILM REACTIVITY IN CHEMISTRIES 100

III.4.1. Reactivity vs copper plating chemistries 100

III.4.2. Reactivity in acidic solutions 107

III.4.3. Reactivity vs alkaline solutions 109

III.5 CONCLUSION 114

III.6 REFERENCES 115

GENERAL CONCLUSION 118

LIST OF FIGURES 122

LIST OF TABLE 126

LIST OF ACRONYMS

APPENDICES

General Introduction

The integrated circuit (IC), also known as a microchip or microelectronic circuit, is an electronic component reproducing one or several complex electronic functions. They are fabricated as a single unit, in which miniaturized active devices (e.g., transistors and diodes) and their interconnections are built up on a thin substrate of semiconductor material (silicon).

Jack Kilby (1923 - 2005) is the inventor of the integrated circuit. In 1958, while employed at Texas Instruments, he created the very first integrated circuit, which led to the foundation for modern computer hardware. At the time, Kilby had simply connected different transistors together by wiring them together by hand. It would then take only a few months to go from prototype to mass production of silicon chips containing multiple transistors. These interconnected sets of transistors in the same block, allowed the realization of memory, but also logical and arithmetic units.

Semiconductor industry components are at the heart of all electrical and electronic equipment. They are a growing part of the objects that surround and accompany us, objects to which they confer functions of information, storage, transmission or restitution (cameras, smartphones, TV, ...), control and command, decision support and security. The Semiconductor Industry Association (SIA) announced in September 2020 that worldwide sales of semiconductors were $35.2 billion in July 2020, 4.9 percent more than the July 2019 total of $33.5 billion and 2.1% greater than the June 2020 total of $34.5 billion. Monthly sales are compiled by the World Semiconductor Trade Statistics (WSTS) organization and are typically displayed as a three-month moving average. Memory chips are expected to continue to maintain the largest market share through 2022. Every application market is likely to grow through 2022, led by the automotive and data processing markets. With competition from new startups and entrants from other corners of the tech world, the race to capture the market is only intensifying[1].

The chip types produced by semiconductor manufacturers can be classified in two ways. Generally, chips are identified according to their functionality. But sometimes they are divided into types according to the integrated circuits used. The four main categories according to functionality of semiconductors are memory chips, microprocessors (CPU), standard chips and complex systems-on-a-chip (SoCs). When assorted by types of integrated circuitry, the three types of chips are digital, analog, and mixed.

[1] DanRosso, "Global Semiconductor Sales Increase 4.9 Percent Year-to-Year in July," *Semiconductor Industry Association*, Sep. 03, 2020.

The two basic operations performed by a memory chip are "read", in which the data contents of a memory word is read out, and "write" in which data is stored in a memory word, replacing any data that was previously stored there. Memory is organized in three levels: cache memory, random access memory (RAM) and hard disc drive (HDD). Cache memory is faster and closer to the hardware requesting the data, it is smaller, and it serves as an intermediary. RAM is used to store computer programs and data that CPU needs in real time, it has a small read/write time compared to HDD. In addition, RAM is volatile and is erased once the device is switched off, while the hard disk has permanent storage, and it is used to store user specific data and files[2].

The most important logic circuits are 'AND', 'OR', 'NOT', 'NOT AND', 'NOT OR', 'MEMORY', and 'TIME' delay units. There are two ways of representing the same logic function. If the inverters (NOT) are combined with the basic AND and OR units, then the symbols that are produced are equivalent. The basic component of logic and memory elements is the transistor. Transistors are made of materials known as semi-conductors, such as germanium or silicon. It is possible to change the electrical characteristics of these materials by adding closely controlled amounts of certain impurities. The difference between logic and memory is the way that transistors are distributed and connected[3].

As the technology is improving continuously, the number of transistors incorporated in a single IC chip is also increasing. Depending upon the number of transistors incorporated in a single chip, the ICs are categorized in five groups, starting from 100 transistors for the Small Scale Integration (SSI) and going up to billions transistors for the Ultra Large Scale Integration (ULSI)

Down-scaling was among Moore's predictions, based on doubling the transistor density in the chip every 18 months, which causes the transistors to become smaller in size and consumes less power while performing at a higher speed. For several decades, a key question for semiconductor technologists has been: What are the ultimate limits on Moore's law or what is the maximum density of transistors on a chip? Manufacturers worked hard on miniaturization of interconnects, but they faced several challenges, among them, the lower efficiency of chips after shrinking. In 2003, when the transistor size shrunk to sub 100 nm, the nano-electronic era was unveiled. The continuation of down-scaling lead to the parasitic capacitance and the

[2] Investopedia team, 2020, "The Main Types of Chips Produced by Semiconductor Companies" www.investopedia.com
[3] D. Gray, "CHAPTER 11 - Logic Circuits" in *Centralized and Automatic Controls in Ships* 1966

resistance increased. Lastly, the 2D transistors were abandoned and 3D FinFETs were introduced. This is considered as a revolutionary design in the transistor world, which paved the path for sub 22 nm FinFETs with high performance and full control on the carrier transport in the channel[4].

Choice of materials is an essential key for chip efficiency improvement. In 1997, IBM announced chips with copper interconnects that could make microprocessors faster, smaller, and less expensive than chips made with aluminum interconnects. Copper connections conduct electricity with about 40 percent less resistance than aluminum wires, which results in an additional 15 percent burst in microprocessor speed. Copper wires are also significantly more durable and 100 times more reliable over time. They can also be minimized to smaller sizes than aluminum[5]. Copper also offered an opportunity to add more layers of interconnects.

In addition, copper has low resistivity, high electromigration reliability and few hillocks (see Figure I-1). Hence, lower resistor–capacitor (RC) delay, high lifetime and less shorts between levels were obtained as compared to aluminum. Nevertheless, unlike aluminum, copper atoms have the capability to diffuse into the insulating layers of the chips. Also, copper cannot be dry etched by reactive ion etching like aluminum. So, new materials such as TiN and TaN have been introduced to control diffusion. Chemical Mechanical Planarization (CMP) appeared as a new technique of copper wet etching. Cu seed layer was also added between the barrier and the filling metal (copper) to initiate electroplating.

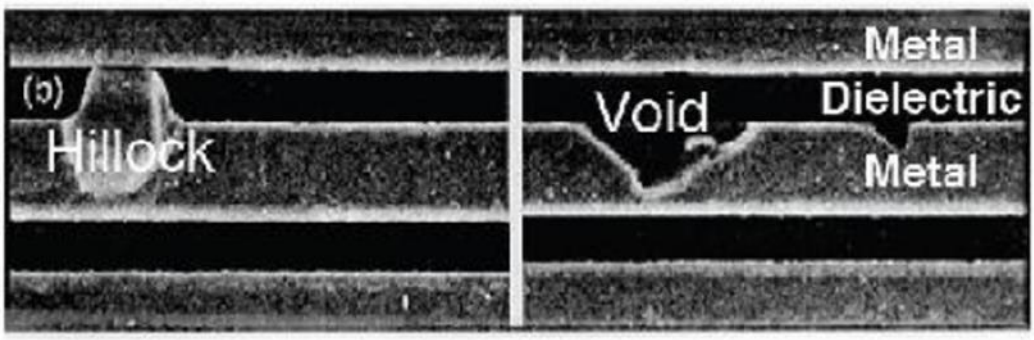

Figure I-1. *Hillocks and voids induced by electromigration*[6].

Copper filling film is deposited generally on the seed layer by electrodeposition. Before bulk copper deposition on a dielectric layer, it is always necessary to deposit a thin seed layer.

[4] H. H. Radamson *et al.*, "Miniaturization of CMOS," *Micromachines*, vol. 10, no. 5, Apr. 2019
[5] IBM100 - Copper Interconnects: The Evolution of Microprocessors
[6] Kyung-Hoae Koo "Comparison study of future on-chip interconnects for high performance VLSI applications" 2011.

Seeds are often deposited by either Physical Vapor Deposition (PVD) or Atomic Layer Deposition (ALD)[7]. Additionally, a liner layer has been added between the copper seed and the TiN barrier for sub 22 nm technology: Cobalt is the preferred material, and its purpose is to improve wettability of the copper seed on the TiN barrier layer thus allowing the former to be significantly thinner and more uniform. Cobalt liner is deposited using CVD.

Today, advancements in the technology have led to interconnects that are 10 times smaller, allowing up to 13-15 levels of interconnects to be placed on a chip. Seed layers impact the filling material behavior. They also must have an excellent electrical continuity to guarantee homogeneous metal deposition.

Tungsten was the preferred material for metallization contact as it has good reliability and ease of integration. However, by downscaling interconnects W presents a bottleneck. This is due to the thickness of the TiN barrier that does not scale proportionally to the reduction in critical dimensions (CD). TiN barrier is required before tungsten filling to avoid fluorine diffusion that can occur because of the type of precursor that is used during the dry deposition (WF_6). Consequently, this leads to an increase in contact resistance. The replacement of the W contact and local interconnects with cobalt removes this scaling bottleneck. Another advantage is that the cobalt CVD allows a thinner TiN layer and seamless fill compared to CVD tungsten. Finally, W replacement by Co allows the wet filling of vias and trenches at small critical dimensions.

Copper has a lower resistivity than aluminum, tungsten, and cobalt. However, due to the difficulty of thinning the structures, the thicknesses of the high-resistivity liner and barrier for the copper interconnects stayed almost the same. This implies that as the wires scale down, the barrier and the liner take up a larger portion of interconnect cross section area. Consequently, they begin to dominate the resistivity of the wire itself. The other issue affecting the wire scaling is the mean free path, which is the average distance the electron travels between collisions. The mean free path of copper is almost 40 nm. As the Cu interconnect approach 40 nm, the copper electrons will begin to scatter from different surfaces and grain boundaries due to the restricted area. This excessive scattering will increase the copper resistivity. Even though transistors have higher performances, there is a mismatch between the transistor and the wire efficiencies. So, copper wires have turned into a serious bottleneck.

[7] Kyung-Hoae Koo "Comparison study of future on-chip interconnects for high performance VLSI applications" PhD dissertation, Stanford university 2011.

Although cobalt has a higher resistivity, it is a potential replacement material for copper as it has a lower resistivity at low dimensions. In addition, contrary to copper, only single film as thin as 1 nm of Co is sufficient to serve as both the liner and barrier for cobalt. This leads to a new scaling path forward for cobalt interconnects.

Nowadays, cobalt is used for only the first two metal layers where narrow pitches are present (M0 and M1), but some companies like Intel®, are using cobalt for the Metal 2 through Metal 5 to also improve electromigration. Finally, Intel also introduced cobalt fill at the trench contact, replacing the tungsten contact metal which was used previously due to the narrow line widths, reducing resistance.

Unlike the cobalt seeds that are often deposited by CVD or ALD, the cobalt filling metal can be electrochemically deposited. As the Co process is a new approach, research and development engineers spend most of their time on the electroplating chemistries development and cost optimization. But the major drawback of using cobalt interconnections and interlayers for device integration is that Co is easily oxidized, especially when cobalt thickness is critical (few nanometers). During the filling process, several steps exist between the input and the output of the wafer in the electroplating tool, during which Co is exposed to air for a short time. This period could be critical for the oxidation of the cobalt seed layer. It is also essential to determine the cobalt oxidation rate when exposed to air.

Mastering the thin films technology is related to the physico-chemistry of the film/air interface. The understanding and the control of seed layers will be determining to obtain a perfect and reliable filling process of high aspect-ratio structures. Even though cobalt is less prone to electromigration compared to copper, and due to lack of expertise, in September 2020 semiconductor industries announced that cobalt was not compatible to replace copper due to corrosion issues in filling. Therefore, Co film behavior as well as cobalt reactivity are key parameters that need to be understood at a fundamental level. Comparison with copper is also essential because the latter is well understood.

Cobalt electrochemical investigation and electrodeposition mechanism comprehension

In interconnects, almost all the cobalt filling chemistries are acidic to prevent the formation of Co hydroxides. The chemistries used are composed generally of a cobalt salt and additives.

In this chapter, the cobalt electroplating process is investigated using a three-electrode electrochemical cell by voltammetry techniques. The electrolyte used is the Cowave aveni® solution. The impact of cobalt concentration and bath temperature on the cobalt electrodeposition are explored. As cobalt's growth mechanism is essential, the Scharifker–Hills model is used to study the nucleation type of cobalt deposited with Cowave. The electrochemical quartz crystal microbalance has been used firstly to evaluate the parasitic reactions during cobalt electrodeposition and secondly to evaluate and control the thickness of the cobalt films. This tool allowed us to perform the reactivity study in the chapter II.

Cobalt thin films behavior

During electroplating, the coupon is immersed in the cobalt solution and the seed layer is in contact with the bath. The queue time between immersing and launching the electrodeposition process is important. At the end of the process, the time spent between rinsing, drying, and packaging the coupon is also critical because of the exposure time to air.

In this thesis, in addition to the study of the filling process and the characterization of the electrodeposited cobalt film, the quantification of the reactivity of cobalt to air exposure and chemistry exposure is performed.

To form the interconnect structure, trenches and vias are fabricated by patterning an insulating layer; typically, a low-k dielectric. A material barrier layer, typically titanium nitride or tantalum nitride TiN or TaN, is deposited over the wafer surface to prevent copper diffusion into the dielectric during post-process annealing. A conformal seed layer (e.g., copper) is then deposited with a dry technique to prevent oxidation of the barrier layer, and to create a conductive surface on which an electrodeposition process can be performed. A thick, dry-deposited in situ copper seed layer is necessary when electrochemically depositing copper directly on TaN; otherwise, the lack of wettability creates a discontinuous seed layer and leaves the underlying TaN unprotected. When the copper seed is too thick, the structure becomes too aggressive and cannot be filled without defect: this approach is not compatible with most advanced technologies. Therefore, a cobalt layer called a “liner” is introduced between the copper seed and barrier layers to enhance the copper wettability and avoid discontinuity of the seed.

To obtain void-free filling of the patterned structures, copper electrodeposition is typically performed using an acidic chemistry (pH<2) that uses a combination of additives to serve specific purposes in the metallization process. The integrity of the dry deposited thin films

before and during electrodeposition is a key parameter to achieve defect-free copper filling with a high-quality interface. With this aspect in mind, a new, innovative chemistry has been developed to achieve void-free filling of aggressive structures while preserving the interface quality between each layer of the metal stack. This chemistry is alkaline and relies on organometallic complexes (copper ligands) for bottom-up filling. Such an approach enables the elimination of the copper seed layer and allows plating directly onto the cobalt liner.

In this thesis, considering different integration schemes, samples with cobalt and copper (typical seeds) planar film stacks were exposed to alkaline and acidic plating chemistries for a short time. The exposure time is typical of the actual processes to assess their stability. The objective of this study is to highlight the different chemical and physical mechanisms occurring during the first steps of an electroplating process. Blanket coupon samples with a thin layer of either cobalt or copper, deposited on a thin layer of TaN, were analyzed using XPS before and after exposure to the electroplating solutions. Moreover, time dependencies of the open circuit potential of these coupons are also recorded to provide in situ information of the stacked layer. This study is published in the Journal of the Electrochemical Society[8].

To evaluate the Co/air interface reactivity, a new method using XPS is employed. By investigating Co2p and O1s spectra, the nature and coverage of the cobalt oxides are determined.

The impact of immersing time on the Co seed is unknown. It is worth noting that the seed physico-chemistry could affect the filling process. A confirmiration that the surface morphology, adhesion, and roughness of the deposited copper are influenced by the thickness of the Cu seed layer. As cobalt is more reactive than copper, some fundamental questions regarding the behavior of the cobalt need to be answered. **How long can the Co seed be left in contact with air? What is the thickness of the cobalt oxides? How long can the Co seed be left in the electroplating bath?**

To answer these questions an analysis strategy is set up. This consists of investigating a 400 nm Co film. The Co layer is deposited electrochemically using aveni's cobalt chemistry *Cowave*©. Inside the XPS chamber the sample is etched to obtain a metallic cobalt by the argon sputtering process. The obtained layer is defined as a reference, and it is then exposed to air in

[8] L. Caillard, et. al, "Investigation of Cu/TaN and Co/TaN Barrier-Seed Oxidation by Acidic and Alkaline Copper Electroplating Chemistry for Damascene Applications," *J. Electrochem. Soc.* 2018.

a dedicated chamber with varying exposure times. The fully automatic venting chamber of the Nexsa spectrometer allowed us to precisely control the air exposure time. A published paper in Electrochemical Society is dedicated to this study[9].

To assess the cobalt behavior inside *Cowave*© chemistry, a study was done using a Electrochemical Quartz Crystal Microbalance. The investigation consists of tracking the mass variation as a function of time of the electrodeposited cobalt on a gold working electrode. These experiments allowed us not only to define best the electrodeposition conditions, but also to assess the deposit stability. A more detailed analysis follows this study by exploring the behavior of Co thin film during immersion in different acidic and alkaline buffers and under different conditions of oxygen concentration.

To evaluate the cobalt oxides, amount and nature, a deposited Co film is immersed in acidic aqueous solutions. After immersion, the sample is rinsed, dried, and then introduced in the XPS entrance chamber and immediately analyzed.

[9] A. Etcheberry *et al.*, "X-Ray Photoelectron Spectroscopy Estimation of Cobalt Seed Layer Reactivity Toward Air Exposure: A Challenge?," *ECS Trans.*, 2020

CHAPTER I Theoretical Background of Metallization in Interconnects

CHAPTER I THEORETICAL BACKGROUND OF METALLIZATION IN INTERCONNECTS... 18

I.1 INTRODUCTION....19

I.2 MICROELECTRONICS....20

I.2.1. Interconnects scaling and limitations....20

I.2.1.1 Temporary solutions of overcoming these limitations....22

I.2.1.2 Interconnection network organization....23

I.2.1.3 Damascene process....25

I.2.2. Electromigration....28

I.3 METALLIZATION....34

I.3.1. Electrochemical cells....34

I.3.2. Electroplating and film growth....35

I.3.2.1 Deposition techniques....37

I.3.2.2 Film growth....39

I.3.2.3 Effect of additives....40

I.3.2.4 Factor effecting electroplating....43

I.4 REFERENCES....46

I.1 Introduction

As explained in the general introduction, the interconnects in microelectronic face extreme challenges whether during their manufacture or during the metallization process.

In the first part of this chapter, the fundamental concepts of interconnect structures are presented. The network organization of interconnects as well as their limitations will be also discussed. As the dimensions of interconnects continue to scale down, microelectronic structures challenge several characteristics parameters (Resistivity, Electromigration phenomenon…). These limits and challenges are essential because they are at the heart of this thesis work. An overview of fabrication processes of Back-End-Of-Line (BEOL) and Front-End-Of-Line (FEOL) will be presented using the damascene process. On narrow features below 10nm, copper filling film shows limitations. For that reason, we will study the cobalt as a potential candidate for the replacement of copper in the damascene process.

The second part of this chapter is dedicated to the description of the metallization process of interconnects. Starting from the electrodeposition techniques and the bath composition, up to the film growth. Numerous are the parameters affecting electroplating, among them, pH, bath additives and temperature, these parameters will be briefly presented and illustrated in this chapter. The experimental part of the thesis is situated in this context. The need of a post-annealing step will be also discussed.

I.2 Microelectronics

I.2.1. Interconnects scaling and limitations

The origin of microelectronics dates to the 1950s with the discovery of the transistor effect by Shockley. A current flowing through a forward-biased NP junction and a reverse-biased PN junction, very close together, can be modulated by the potential applied across the reverse-biased junction. So, it is possible to obtain a smart "switch" commutable by an electrical signal. This discovery has led to the development of solid-state electronics as an alternative to the vacuum tubes previously used [1], [2].

Nowadays, logic functions are based on the integration of MOS (Metal Oxide Semiconductor) transistors, the feasibility of which was later demonstrated in 1960 [3]. This type of transistor owes its name to the stack of materials located at its gate: The Metal contact, the insulator, initially made of Silicon Oxide, and finally the Semiconductor substrate. Here, the switching function is provided by a field effect at the gate; the voltage applied between the gate metal and the substrate will allow the creation or not of a conduction path between the source and the drain of the transistor (see Figure I-1).

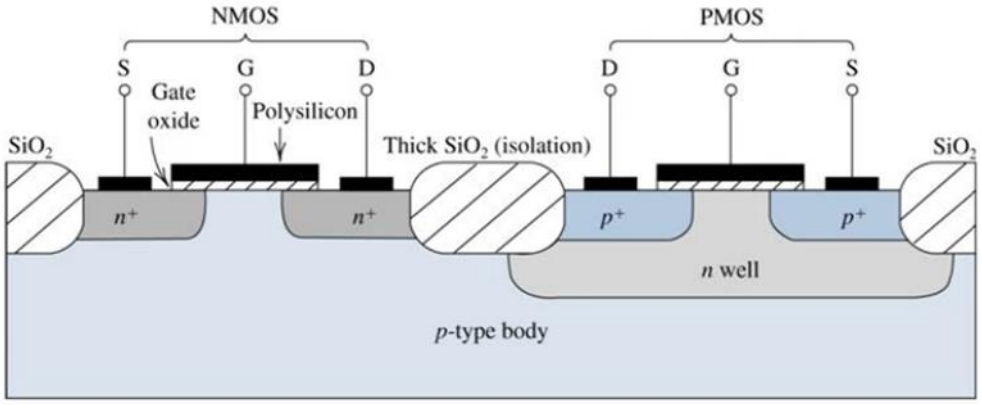

Figure I-1. Complementary Metal-Oxyde-Semiconductor (CMOS) cross section diagram. S: source, G: gate, D: drain.

The appearance of these electronic components, smaller and more reliable than electronic tubes, is the first link allowing the miniaturization of circuits. This is how Feynman in 1960 in his famous speech ≪ There's Plenty of Room at the Bottom ≫ describes a miniaturization of all systems up to a factor of 25000 and describes some techniques used in microtechnology. In a more pragmatic way, Gordon Moore has established an empirical law on the increase of the number of components in an integrated circuit as a function of time [4]. The principle of this

law, known as ≪ Moore's law ≫, is based on the essentially economic advantages of integrated electronics over conventional electronics based on isolated components. It describes that the number of components integrated in a microchip is multiplied by a factor of 2 every year. This law was revised in 1975 in a version where the number of transistors integrated in a microprocessor doubles every two years. From a realizations point of view, if we look at the number of transistors per integrated circuit for Intel since 1971, we can see that this number follows the revision of Moore's law (see Figure I-2).

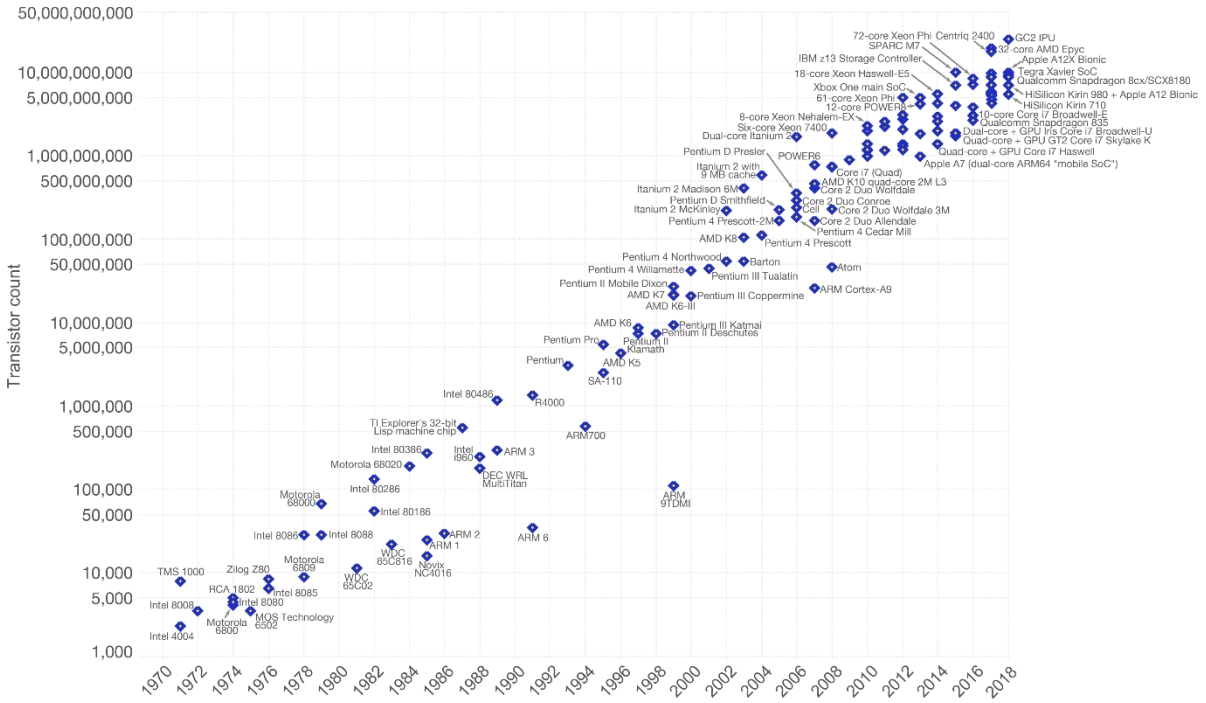

Figure I-2. *Evolution of MOS transistor counts over the years [credit: Licensed under CC-BY the author Max Roser* [10]*].*

Moore's law is strongly related to the dimensions of integrated transistors. It does not directly consider the geometry factors. For example, to reduce the switching time of MOS transistors, their gate length must be reduced, which corresponds to the length travelled by the electrons between the drain and the source. This reduction is accompanied by a general miniaturization of these components. This is necessary to maintain with Moore's law, because if the size of the transistors had not changed since 1971, the size of a chip would be around 400,000 times bigger nowadays. A roadmap is defined concerning the evolution of the dimensions in the circuits. This reference is established by the ITRS (International Technology Roadmap for Semiconductors) in partnership with numerous industry players (manufacturers,

[10] www.ourworldindata.org

academic partners, and research institutes) to ensure progress in this field by limiting the financial risks involved [5]. The reference length in logic circuits, the grid length, has been the subject of attention for many years now and its evolution is programmed.

Whereas in a circuit, the active part that allow the production of an electrical signal is provided by the transistors, the signal is transmitted between the different functions by interconnections. These interconnections consist of a network of metal lines separated from each other by an insulator.

These metal lines developments are affecting the performance of interconnects, which now impose limitations on energy dissipation, delay and signal integrity in an integrated circuit [6]. In a more general and systematic way, Meindl defined in 1995 a hierarchy of limitations for future integrated circuits [7]. Divided into five categories: fundamental, hardware, devices, circuit, and system. Without going into detail, it appears that for each of them, two types of limitations are to be considered, one theoretical, the other practical. Theoretical limitations are generated by physical laws and technological innovations. Practical limitations cover constraints related to manufacturing costs and market trends.

I.2.1.1 Temporary solutions to overcome these limitations

Reduce interconnection delay consists, at first, in minimizing the value of its time constant or resistance-capacitance (RC) product. Technological solutions have been implemented in this area. For that reason, aluminum, a metal previously used for interconnections, has been replaced by copper, which is less resistive. However, the width of copper lines trends to reach lower values than the mean free path of electrons, resulting in a sharp increase in the resistivity of the lines. The dielectric permittivity of interline insulators decreases due to the introduction of porosity. But, here again, the maximum porosity rate is already under study and cannot be increased indefinitely. These technological improvements are reaching their physical limits, making it difficult to continue the miniaturization of conventional 2D circuits as foreseen by Moore's law [4]. Therefore, at constant dimension, to reduce these values, the investigation of a new materials is essential.

To understand the whole issue of the interconnection network, it is necessary to describe its hierarchy precisely, and to understand how the distribution of the different lengths of interconnections can be anticipated. All these issues are of prime importance today because the circuits are becoming extremely complex, and traditional integrations are likely to be too cumbersome to implement soon, both technically and financially.

I.2.1.2 Interconnection network organization

The node technology is a semiconductor manufacturing process. The smaller the technology node means the smaller the feature size, producing smaller transistors which are faster and more efficient. The term node refers to several parameters of a transistor such as the gate length but recently the number itself lost the exact meaning due to diversity of marketing of different foundries. For example, Intel's 10 nm is comparable to foundries 7 nm while Intel's 7 nm is comparable to foundries 5 nm. The CMOS structure presented in Figure I-3 is composed of two portions BEOL and FEOL. The RED square represents the heart area of this work.

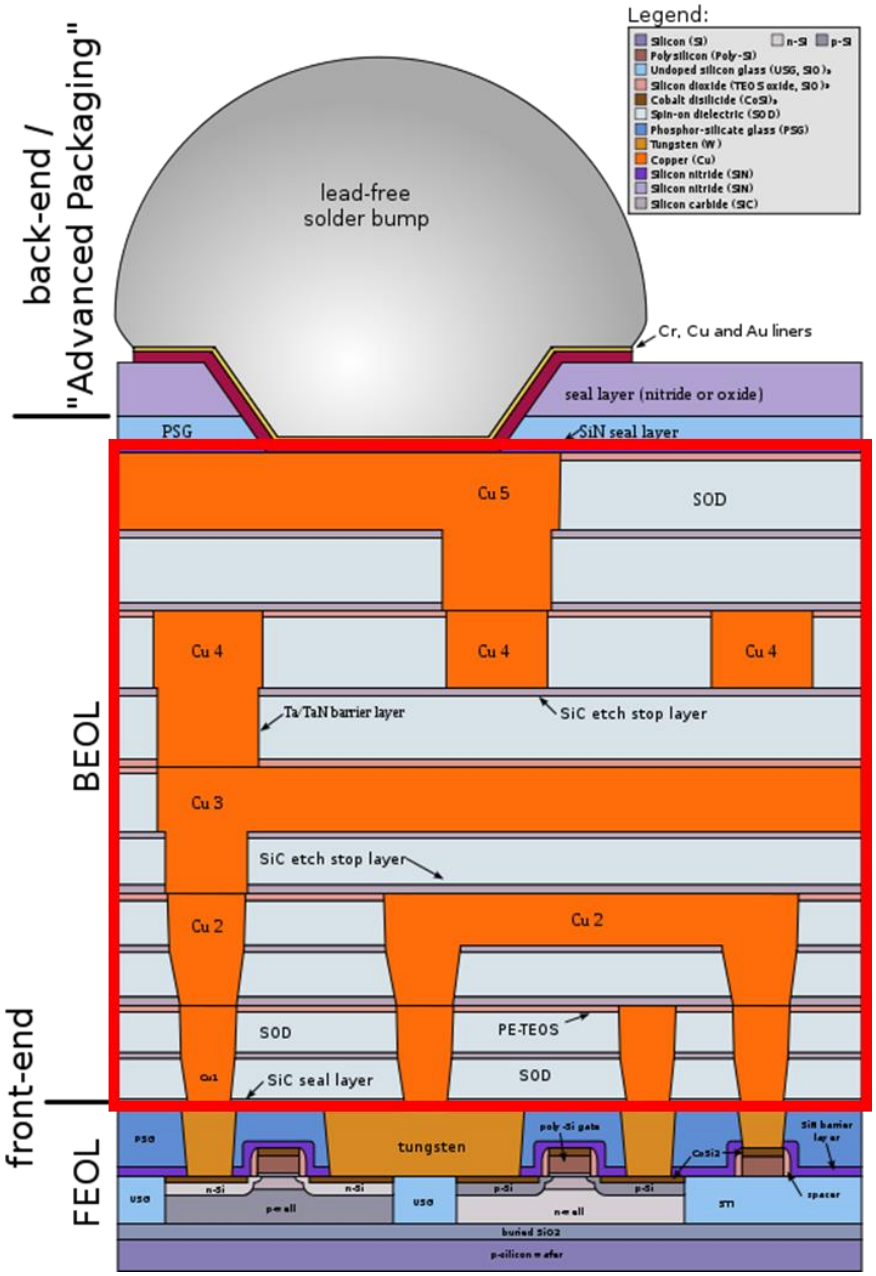

Figure I-3. *CMOS global structure.*

BEOL in an integrated circuit responds to a logic of prioritization of the physical levels of interconnections (metallization levels). This categorization of interconnections is defined according to factors such as metal line spacing, cross-section, maximum signal propagation time and communication mode (e.g. intra-block, inter-block, power distribution, clock frequency). A level contains one or more layers of metal lines with the same spacing (pitch). The level closest to the active parts FEOL, called the local level, is mostly responsible for short distance intra-block communications. The metal lines in this level are the shortest and the thinnest spaced. The level furthest from the active parts is called the global level. It is used for long-distance inter-block communications and for power and clock frequency distribution. Since this level contains the longest lines, the spacing of the lines is as wide as possible to minimize signal propagation delays. A modern interconnection architecture typically has two levels of hierarchy: local and global, comprising up to 10 metal levels named from M0 - M10 where M0 is the first interconnection of transistors. Generally, it is performed with tungsten (see Figure I-4) [8].

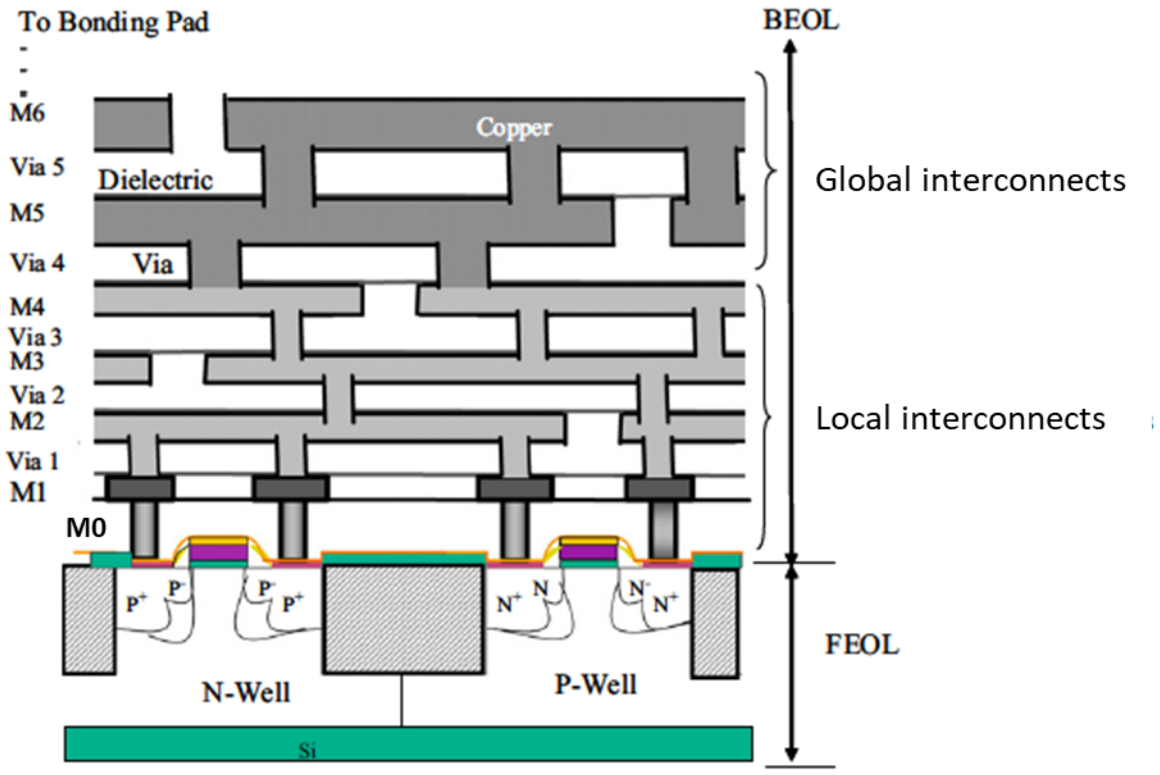

Figure I-4. *Metallization layers in interconnections.*

The interconnects close to the transistors need to be small because they connect tiny components. These components are often tightly packed together. These lower-level lines, called local interconnects, are usually thinner and shorter in length. Global interconnects are

structurally higher; they move between different modules of the circuit, so they are usually thicker, longer, and far apart. The connections between interconnect layers are called vias, which can transmit signals and power from one layer to the next.

I.2.1.3 Damascene process

The term "Damask" refers to a patterned silk fabric woven in Damascus (Syria). The city is known for manufacturing of damascened steel sword blades, which are extremely hard and flexible. In French, damascene is “damasquiner”, which means to decorate in the way of Damascus blades. Therefore, the word damascene can be understood literally as the process of decorating metal with wavy patterns of gold, silver, or copper.

Copper is integrated in a new way in microelectronic structures. This is due to the difficulty of shaping copper by conventional methods. The new integration procedure was developed by IBM in 1990’s. This method is called “Damascene process”.

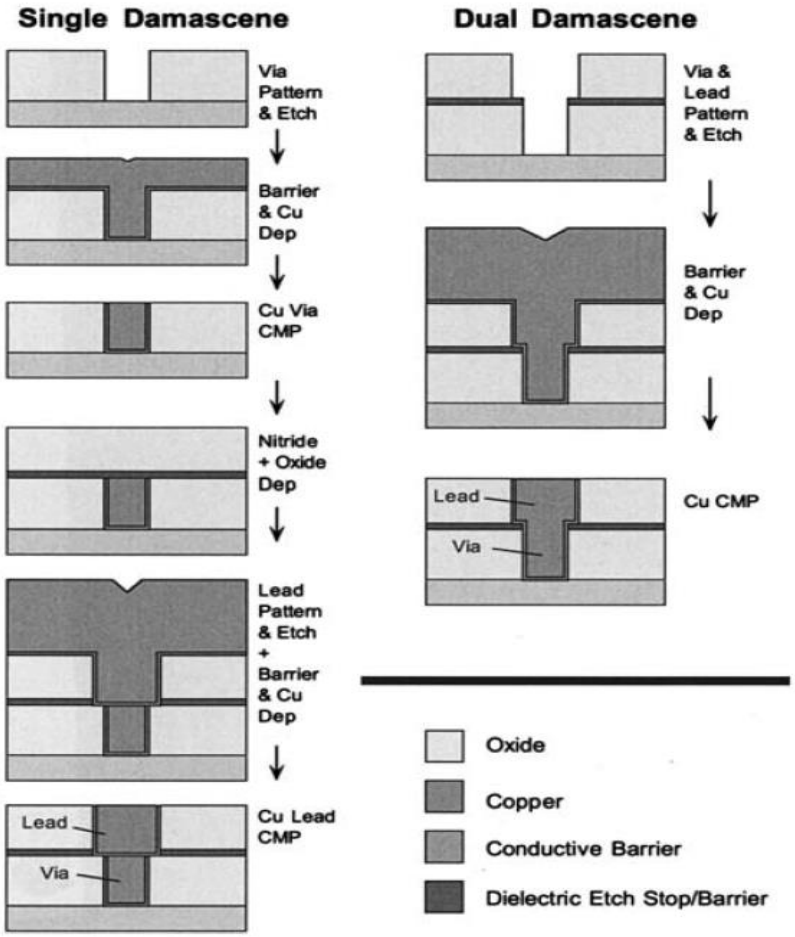

Figure I-5. *Single and dual damascene process.*

The copper damascene process involves etching trenches in the dielectric layer and fill the trench with a barrier layer to prevent Cu diffusion, and then deposit a Cu seed layer as the nucleation center of electroplated Cu. Finally, the overburden metal is removed by chemical mechanical polishing (CMP). Figure I-5 shows that the damascene process can be either single damascene (SD) or double damascene (DD). The difference between the single damascene (SD) process and the dual damascene (DD) process is that in the dual process, one metal deposition step and one CMP are eliminated. The reduction in the number of processing steps makes DD more attractive than its single damascene process counterpart. In the SD process, the plug is usually tungsten (W), while in the DD process, most of the via holes are filled with Cu, although some industrial houses use Al in the DD process [9].

In the dual damascene process, the trenches and vias in the dielectric layer can be performed by various methods. They are mainly classified into trench first or via first. Each method has its advantages and disadvantages, but the via first approach is widely used in industry due to its reliability.

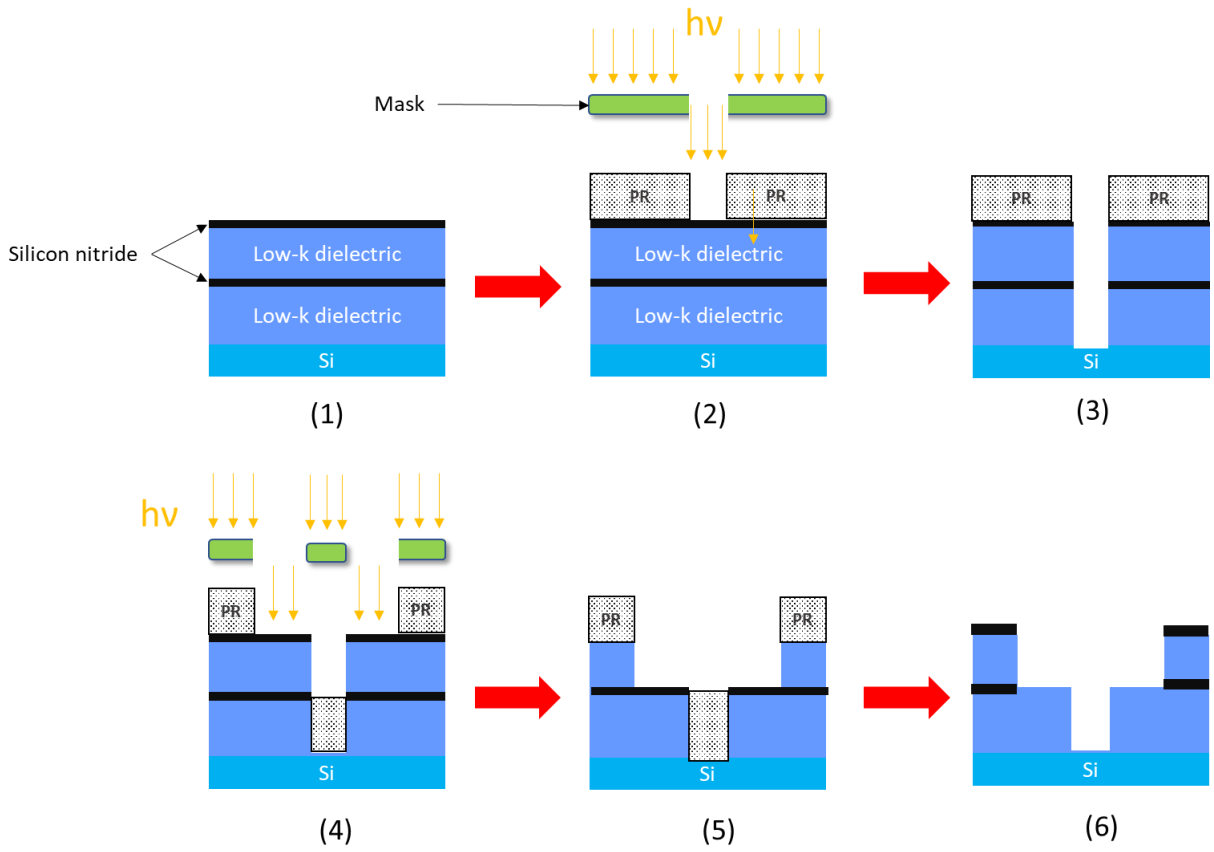

Figure I-6. *Dual damascene patterning - Via first approach.*

In the Via-first approach method (see Figure I-6), the wafer is coated with a photoresist (PR), and then a photolithographic patterning process is applied (see Figure I-6.2). Next, one must perform an anisotropic etching to cut through the hard mask surface (silicon nitride) extending down through the dielectric, the embedded etch stop, and finally stops on the bottom silicon nitride barrier. The most important thing is that the via etch does not penetrate the bottom layer. Otherwise, the via etch will sputter the copper into the barrier. This will cause Cu atoms to diffuse into the dielectric and eventually lead to device failure. Next, the via photoresist is stripped (see Figure I-6.3) and the trench photoresist is applied. A second photolithographic patterning is performed. Some photoresists will remain on the bottom of the via (see Figure I-6.4). this photoresist will prevent the lower via from being over-etched during the trench etching process.

An anisotropic etch is then performed, which etches the surface hard mask and down through the dielectric. It stops at the embedded hard mask and this will form trenches. The photoresist is then stripped and the silicon nitride barrier at the bottom of the via is opened (Figure I-6.6) by a very soft etch, which does not cause copper diffusion into the via.

After patterning vias and trenches, a thin film of tantalum nitride or titanium nitride is added by chemical vapor deposition. This thin layer will serve as a barrier against copper diffusion. The thinnest thickness of this layer (~2 nm) makes the vacuum-based deposition process the suitable one. A second layer is added, it is a thin layer of Ta, Ti or Co deposited by CVD. This layer is called liner, it will serve as an adhesion layer between the barrier (TaN or TiN) and the copper seed. This metal seed is deposited by physical vapor deposition (PVD) and the thickness of the metal seed layer is about 3 nm. Cu seed layer will serve as an electrical contact for electroplating; thus, it should be continuous and uniform all over the via or the trench.

After patterning the structure, copper is electrochemically deposited (ECD) to fill the interconnection structures. The copper deposition is followed by CMP to remove the excess of copper overburden. After CMP, annealing process is performed to reduce the line resistance of copper. The interconnect level is completed by the deposition of the dielectric diffusion barrier, over the entire plate [10].

The resistance of the wire increases as the cross section of the wire becomes smaller. Narrower wires have greater resistance, dissipate more power, and generate more waste heat. In the case of copper interconnects, there are two other factors that make the problem worse.

One is the relationship between resistivity and line width. The mean free path of electrons in copper is about 40 nm [11]. Which is the average distance travelled by electron between successive impacts (collisions). When the line width is close to this value, sidewall scattering begins to contribute, and the resistivity rises sharply. This phenomenon is illustrated in Figure I-7.

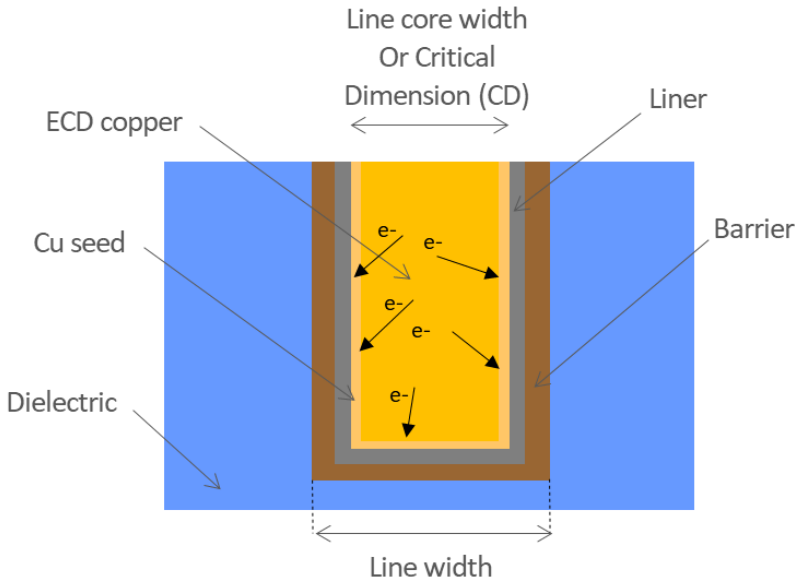

Figure I-7. *Sidewall electron scattering in copper wires (CD < 55 nm).*

Making the problem worse, the copper wire is wrapped in a barrier layer to prevent diffusion into the dielectric. If these layers are too thin, they will not fully function: as the line width decreases, the thickness of the barrier layer will remain relatively constant. A part of the wire made of copper shrinks. In turn, this affects line width-related characteristics such as grain structure and resistivity.

I.2.2. Electromigration

After a first observation in 1861 by M. Girardin, a French researcher, the interest in electromigration remained purely scientific for a long time. The arrival of the first integrated circuits (1958) marked a turning point. Their lifetime did not exceed a few weeks and thus prevented their commercialization. Manufacturers then began reliability studies to understand the degradation mechanism and delay failure.

Electromigration is a material transport phenomenon in metals, induced by a high current density and strongly influenced by temperature and mechanical stress.

When the current flows, two forces are exerted on the atoms [12]. The first is the electrostatic force and the second is related to the flow of electrons. The electrons transfer momentum to the atoms when they impact it. For copper interconnections, the TaN/Ta barrier layers at the bottom of the via act as blocking boundaries. Thus, during an electromigration stress, the metal atoms will be exhausted on the upstream side of the wire and voids will be formed (see Figure I-8). If the voids become large enough across the via, the resistance will increase considerably, and the circuit will fail. At the downstream end of the wire, metal accumulate and causes hydrostatic stress [13], [14].

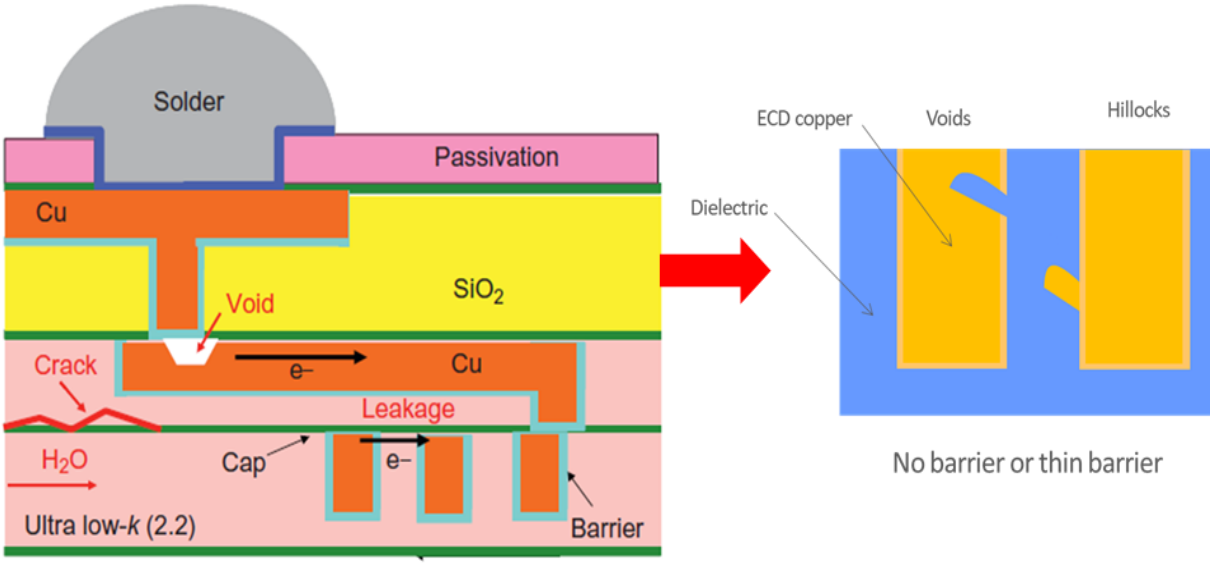

Figure I-8. *Failure mechanisms for Cu interconnects.*

As the wire critical dimension (CD) shrinks below 30nm, the Cu line resistance is expected to increase dramatically due to the increasing Cu resistivity. This resistivity increases because of electron scattering at the sidewalls and grain boundaries, and the diminishing of wire volume that Cu occupies because of the need for thick barrier and liner. Scaling down the barrier/liner is difficult so replacement metal, although with larger bulk resistivity than Cu, could result in lower wire resistance if they do not require thick barrier/liner and if they exhibit smaller resistivity increase than Cu as the wire CD decreases. Applied Materials put a comparison (see Figure I-9) of tungsten, aluminum, copper, and cobalt. Notably, they made a distinction between narrow metal and wide metal features.

Figure I-9. *Materials comparison for narrow and wide features made by Aplied Materials.*

On narrow features, the ability to fill trenches with high-aspect-ratio is higher with cobalt than copper. Resistance is also lowest with cobalt, and reliability is high. That reliability is largely relates to electromigration (EM). After a comparison cobalt shows line resistance benefit compared to copper for the CD bellow 10nm as presented in Figure I-10 [15].

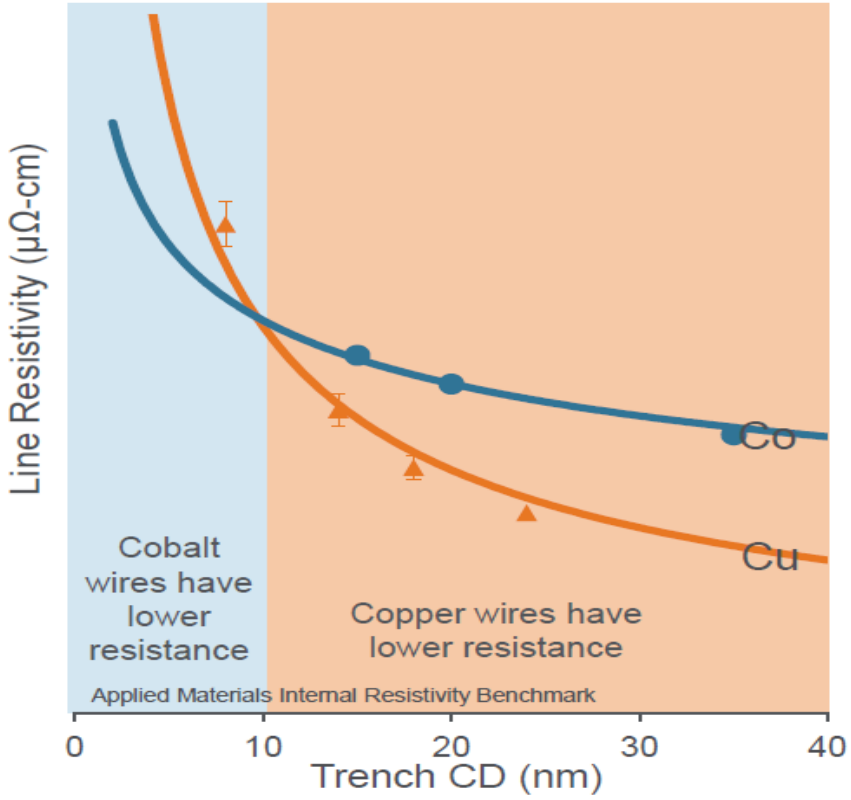

Figure I-10. *Copper vs cobalt line resistivity as a function of CD, (Applied Materials[11]).*

[11] www.appliedmaterials.com

One of the fundamental components of a semiconductor, the interconnect, is undergoing radical changes as chips scale below 7 nm. Some of the most pronounced shifts are occurring at the lowest metal layers. As more and smaller transistors are packed onto a die, and as more data is processed and moved both on and off a chip or across a package, the materials used to make those interconnects, the structures themselves, and the entire approach for utilizing those structures is changing.

At the most fundamental level, the challenge is ensuring a good connection between different layers. The problem is that copper, which has been used been used for those interconnects since 130 nm technology, has largely run out of steam. Therefore, at 10nm, Intel made a switch. The local interconnect layers—M0 and M1—incorporate cobalt or tungsten, not copper, due to the proximity of these levels to the dielectric. The remaining layers use traditional copper metal. Others are exploring the idea.

One of the problems with copper is that at the most advanced nodes it can diffuse into surrounding materials. That requires a barrier layer, but as scaling continues to 5 nm and 3 nm, those barrier layers need to be thinner. But they also need to be conductive.

Cobalt is a potential candidate to replace copper in the damascene process. Due to its low line resistivity in narrow features which is lower than copper's one. Cobalt does not need a liner (Ta or Ti), this leads to lower the line resistivity. The major disadvantage is the **lack of fundamental and technological knowledge of cobalt**. This lack comprises 2 topics, the first is the development and the control of cobalt deposition process and chemistry. The second concern the reactivity of the cobalt seed layer. As the Co seed is only 3 nm in thickness, its stability becomes a key parameter of the filling process. The problematics of this thesis are illustrated in Figure I-11 and are described as follows:

In step (3): Since it is impossible to use thinner barriers in the copper damascene process at narrow features, a new approach will be investigated. In this approach firstly a new chemistry for copper-zinc electroplating is developed. Then, an electrochemical and an annealing process are designed to allow the zinc migration. Zinc migration will serve as a barrier in copper damascene process.

In step (4): Cobalt seed is only 3 nm in thickness. The stability of this layer in the electroplating chemistry is a key parameter. Understanding the behavior of this seed layer when exposed to air is also important. XPS and RQCM are used to assess the evolution of this seed layer in chemistry and when exposed to air.

In step (5): Electrodeposition of cobalt is investigated by studying the different parameters impact on film formation. Starting from nucleation mode and deposition mechanism. Bath temperature, additives, and pH are key criteria for co electrochemical deposition. In this thesis all these parameters are investigated using an electrochemical cell coupled with quartz µ-balance.

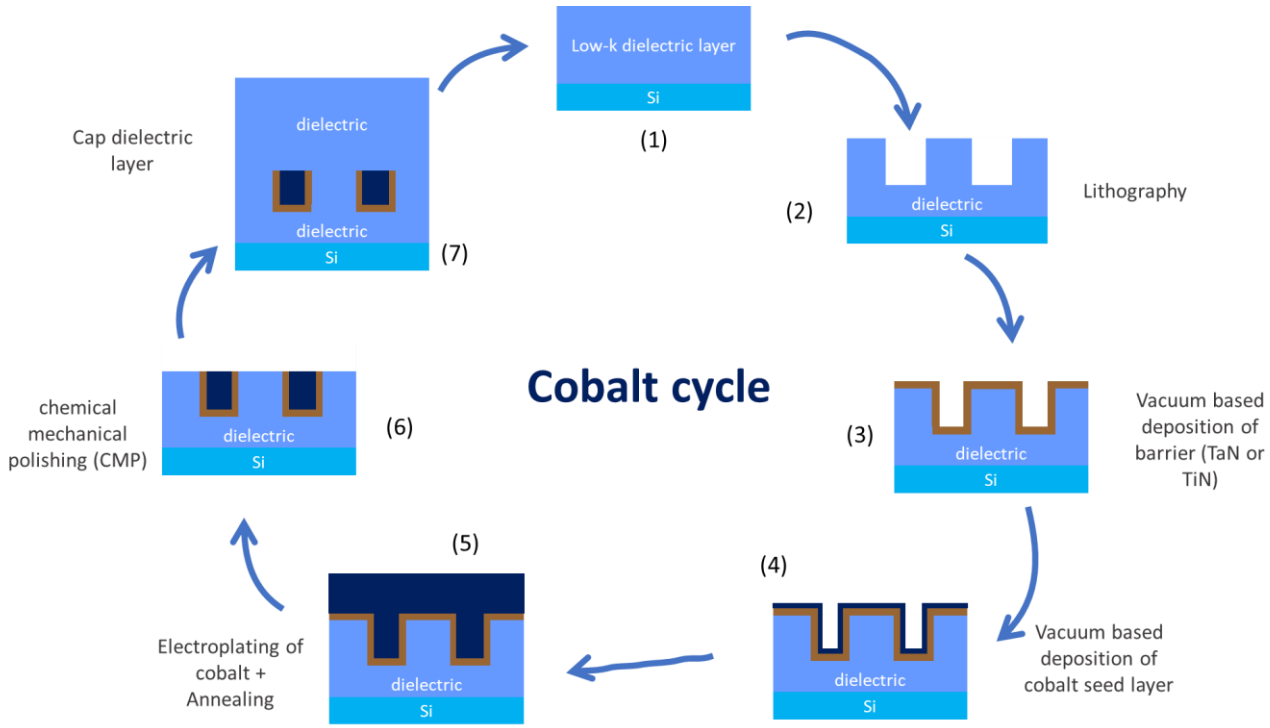

Figure I-11. *Cobalt process cycle.*

The important role of the Co-seed led us to ask questions about the stability of this layer, and therefore its reactivity. To evaluate its reactivity in air, cobalt was compared to copper which is well known material. Figure I-12 shows the Ellingham diagram of copper and cobalt. After calculating the corrosion pressure at room temperature of cobalt and copper oxides equilibrium CoO and Cu_2O, respectively. Both P^{Cu} and P^{Co} are found less than P_{O2}= 0.2 bar, which means that the Cu_2O and CoO are the more stable forms of Cu and Co. However, the P_{Co} is low compared to P_{Cu} which means that only a smaller air pressure is sufficient to form CoO. This shows that Co is more unstable than copper in presence of air.

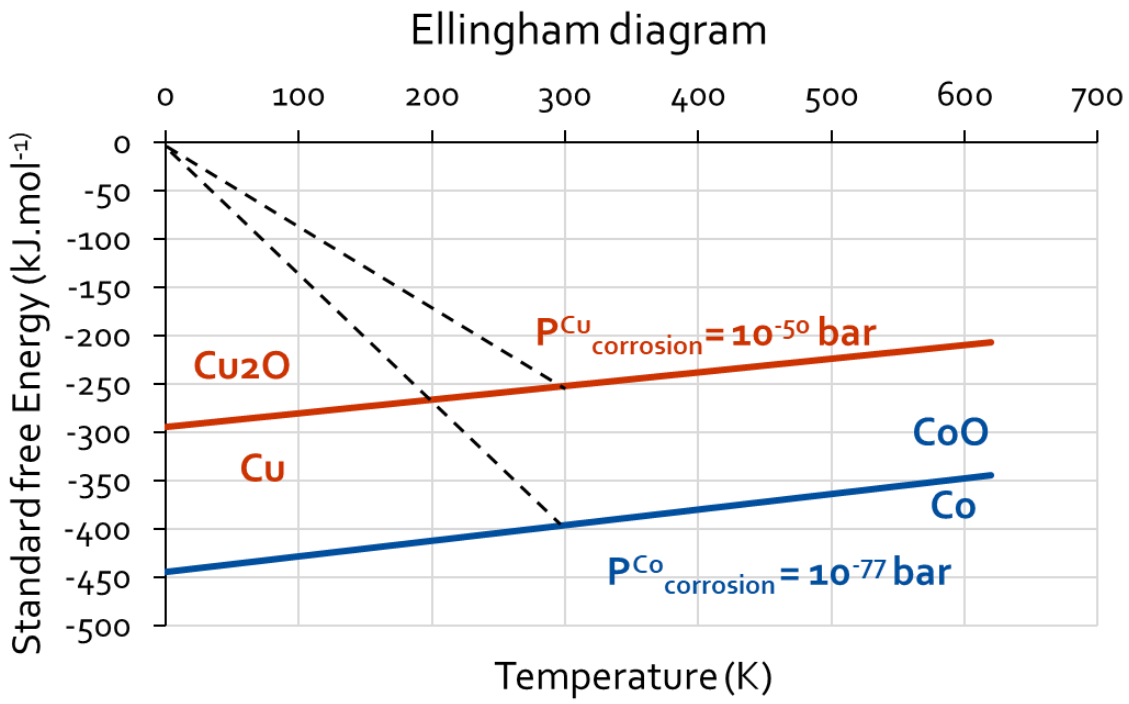

Figure I-12. *Co/CoO and Cu/Cu2O Ellingham diagram with corrosion pressure equilibrium.*

The cobalt seed is immersed in electrolytes in order to launch the electrodeposition process. These electrolytes can have a wide pH range. For example, acidic is the pH used generally for cobalt electrodeposition, basic is the used pH for Co electroless deposition. Thus, the understanding of the stability of Co thin seed layer in electrolytes is a key parameter. From Pourbaix diagram, it is clear that Cu is stable at all pHs. However, cobalt shows an instability in all acidic pHs due to the reaction with protons. This instability results in Co dissolution and H_2 release. The pourbaix diagram in Figure I-13 shows the existence of a small domain of Co stability under strong alkaline conditions pH>8 (blue area). At this range of pH, the cobalt electrodeposition becomes almost impossible due to the precipitation of Co ions.

The thermodynamics of cobalt in air and in chemistry confirms the instability of Co, however, questions are asked about the kinetic of these instabilities. In this thesis, the kinetics of the Co instability in air and in chemistries will be measured using XPS and EQCM.

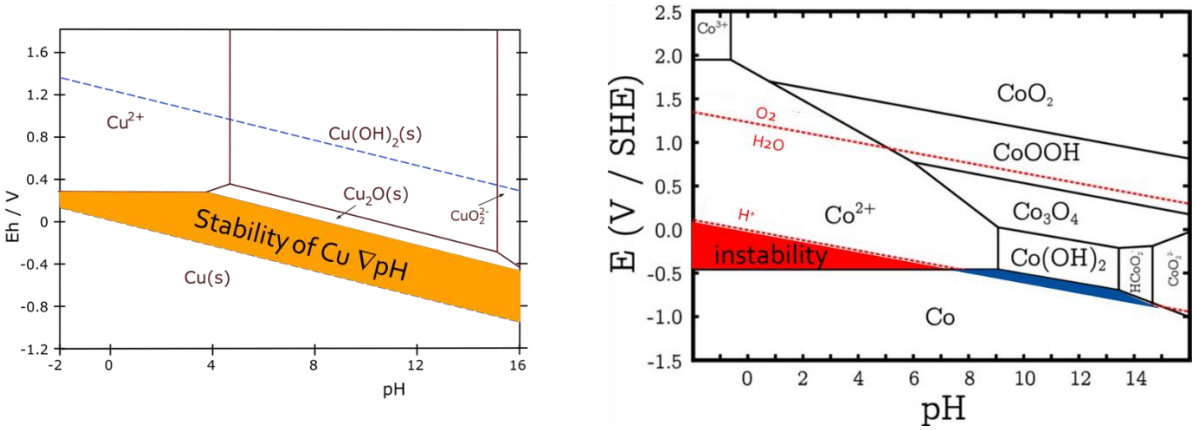

Figure I-13. *Pourbaix diagram of Cu (left) and Co (right) showing stability and instability domains in water.*

I.3 Metallization

I.3.1. Electrochemical cells

Electrochemistry is a branch of chemistry that studies the combination of the electrical and chemical effects. It describes chemical phenomena coupled with reciprocal exchanges of electrical energy. Electrochemistry includes several technologies and techniques, such as electrolysis, corrosion, batteries, fuel cells, accumulators, and electroplating [14].

An electrochemical cell is a device capable of generating electrical energy from chemical reactions or using electrical energy to cause chemical reactions. In Industry, it is composed of two electronic conductors called electrodes (anode and cathode) and an ionic conductor named electrolyte (see Figure I-14). The disadvantage of this type of cell is the non-control of potential, because of the changing of both electrodes' interfaces.

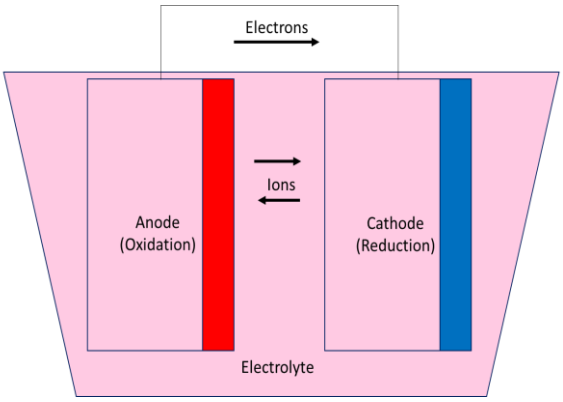

Figure I-14. *Two electrodes electrochemical cell used in industry.*

For that reason, in this thesis a three electrodes electrochemical cell is used. This cell is composed of a gold working electrode (WE), a platinum counter electrode (CE) and a silver chloride (Ag/AgCl) reference electrode (RE).

Various factors can affect the current collected between WE and CE. These factors are classified under 3 types (see Figure I-15):

- Resistance of charge transfer R_{CT} near the interface electrode/electrolyte, it is impacted by electroactive species and the nature of the surface.
- Resistance of mass transfer R_{MT} in the solution: passage of the electroactive species from the solution to the electrode; it is ensured by:
    - migration of the ions under the influence of the electric field.
    - diffusion of the ions due to the concentration gradient caused by the reaction at the electrode.
    - convection due to any form of agitation (stirring,).
- Resistance of parasitic reactions R_{PR} for example hydrogen evolution reaction in acidic media.

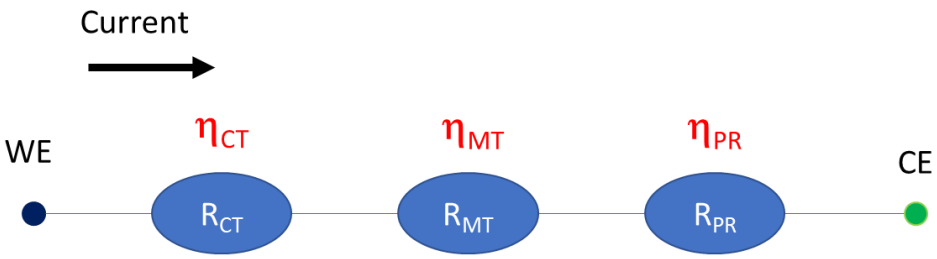

Figure I-15. *Factors affecting current.*

I.3.2. Electroplating and film growth

Electroplating is an electrochemical discipline that consists of thin film synthesis onto a surface. It allows, by the application of an electric current circulating in an electrolyte to ensure a chemical reaction. This depends directly on the nature of the metal salts dissolved in the electrolytic bath. The metal to be deposited is then present in ionic form and is reduced to form a solid metal deposit at the cathode. The electrons for the reduction reaction come from the cathode this phenomenon is governed by Eq. I-1:

$$M^{n+} + ne^{-} \rightarrow = M \qquad \textit{Eq. I-1}$$

Where M is the deposited metal.

For this reduction reaction to be active, the potential of the working electrode is lowered from its equilibrium potential value. This potential can be calculated using the Nernst equation (Eq. I-2) as below:

$$E_{eq_{M^{n+}/M}} = E^{0}_{M^{n+}/M} + \frac{RT}{nF} ln \frac{[M^{n+}]}{[M]} \quad \textit{Eq. I-2}$$

Where E_{eq}= cell equilibrium potential, n=number of electrons, F= Faraday constant, R= ideal gas constant, T=temperature, E° is the standard potential.

In the case of electroplating cobalt on the cobalt seed, the system is totally in Nernstian conditions and the potential at open circuit is equal to the equilibrium potential E_{eq}.

The overvoltage (η) corresponds to the difference between the applied potential E at the electrode and its equilibrium potential E_{eq}. The rate of deposit formation depends directly on the faradic current and parasitic reactions [16], which is a function of the overvoltage. The time required to form a coating is calculated using Faraday's Law, assuming a 100% faradic efficiency, parasitic reactions are then neglected. The relation used (see Eq. I-3) is then:

$$Q = n_{e^-} \times F = \int I \times dt \ \ldots\ldots \text{ with I=const} \Rightarrow Q = I \times t \quad \textit{Eq. I-3}$$

The number of moles of the deposited metal is calculated through Eq. I-4:

$$n_{deposited\ metal} = \frac{n_{e^-}}{z} = \frac{Q}{z \times F} = \frac{I \times t}{z \times F} \quad \textit{Eq. I-4}$$

Where:

Q: Electric charge — I: Applied current

F: Faraday constant (96485 $C.mol^{-1}$) — t: Electroplating time

n_{e^-}: Number of moles of exchanged electrons — z: number of exchanged electrons

To obtain the thickness of the deposited film Faraday's law (see Eq. I-5) is used as follow:

$$Q = n_{e^-} \times F = \frac{m}{M} \times z \times F \quad \textit{Eq. I-5}$$

And

$$\rho = \frac{m}{V} = \frac{m}{th \times A} \Rightarrow m = \rho \times th \times A \quad \textit{Eq. I-6}$$

Combining Eq. I-5 and Eq. I-6, the thickness is calculated by Eq. I-7

$$th = \frac{M \times Q}{\rho \times A \times F} \qquad \textit{Eq. I-7}$$

Where:

th = the thickness, m= deposited mass, ρ = metal density, A= electrode area, M= molar weight

In the presence of parasitic reactions, and to be sure of the obtained mass and thickness, those values are calculated from Q_a which is the anodic charge. This charge is related only to the dissolution of the metal.

Electroplating in acidic media is often accompanied by the proton reduction (Hydrogen Evolution Reaction HER), depending on the reaction Eq. I-8:

$$2H^{+}_{(aq)} + 2e^{-} \rightarrow H_{2(g)} \qquad \textit{Eq. I-8}$$

This phenomenon implies that a part of the applied current during electroplating is consumed by this reaction. It is the case for example of zinc, nickel and cobalt. The consequence of HER in acidic media can be the formation of pitting in the coating, a reduction in cathodic efficiency and an increase in local pH near the surface due to the formation of OH^- resulting from H_2O reduction in acidic media according to Eq. I-9.

$$2H_2O_{(l)} + 2e^{-} \rightarrow H_{2\,(g)} + 2OH^{-}{}_{(aq)} \qquad \textit{Eq. I-9}$$

This can lead to the precipitation of metal hydroxides and induce the embrittlement of the coating, a change in mechanical properties [16]. To quantify this phenomenon, the current efficiency (CE) it is calculated by the following equation (see Eq. I-10)

$$CE(\%) = \frac{Q_a}{Q_c} \times 100 \qquad \textit{Eq. I-10}$$

where Q_a is the anodic charge obtained by redissolution of metal and Q_c is the cathodic charge obtained during deposition.

I.3.2.1 Deposition techniques

In electroplating, a negatively charged layer is formed around the cathode as the process continues. When using direct current (DC) (see Figure I-16.A), this layer charges to a defined thickness and obstructs the ions from reaching the part. In pulse electrodeposition (PED), the output is periodically turned off (t_{off}) (Figure I-16.B and Figure I-16.C) to cause this layer to discharge somewhat. This allows easier passage of the ions through the layer and onto the part.

Compared with the low current density area, the high current density area in the plating solution consumes more ions. During t_{off}, the ions migrate to the depleted area in the bath. When a pulsed t_{on} occurs, a more uniform distribution of ions can be used to deposit on the part. The literature summarizes the influence of pulse current and pulse reverse current variables on electrodeposition [17].

Pulse deposition is mostly used in interconnect fabrication to improve current distribution. While the pulse deposition increases the limiting current density by replenishing metal ions in the diffusion layer during t_{off} period [17]. Desired film composition, structure, porosity and hydrogen percentage could be obtained by changing the pulse parameters [18]. Also pulse current plating decreases additive necessity by 50-60% and it improves bath stability [19]. Pulse reverse current improves step coverage for high aspect ratio structures in TSV's. [3][4][5].

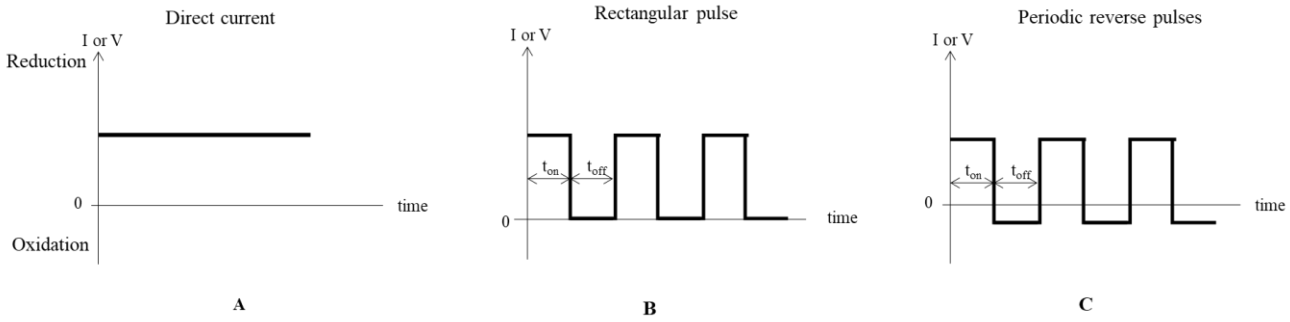

Figure I-16. *Major current waveforms used in electrodeposition, (A) direct current (B) rectangular pulse current and (C) periodic reversed pulse current.*

One important effect in pulse deposition techniques is a modification of the diffusion layer. Under pulse deposition conditions, the Nernst diffusion layer is divided into two diffusion layers, as shown in Figure I-17. In the pulsating diffusion layer next to the cathode, the metal ion concentration pulsates at the frequency of the pulsating current. Pulse deposition technology is mainly used to improve the distribution of the deposit (current distribution), leveling and brightness of deposits [20].

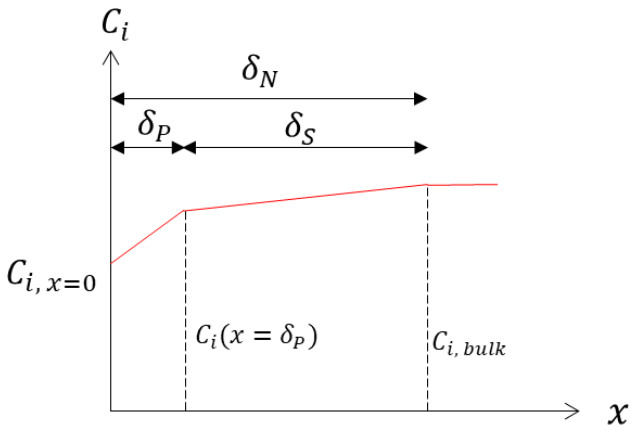

Figure I-17. *Concentration profile at the cathode for pulse plating conditions: \delta_P, pulsating diffusion layer thickness; \delta_S, stationary diffusion layer thickness; \delta_N, Nernst diffusion layer thickness [20].*

I.3.2.2 Film growth

As one of the condensate deposition methods, the nucleation and growth of electrodeposited materials include several stages. We can divide the nucleation and growth of electrodeposition into two main processes, including: (I) deposition and (II) electrocrystallization. The various stages of the electrodeposition process are shown in Figure I-18.

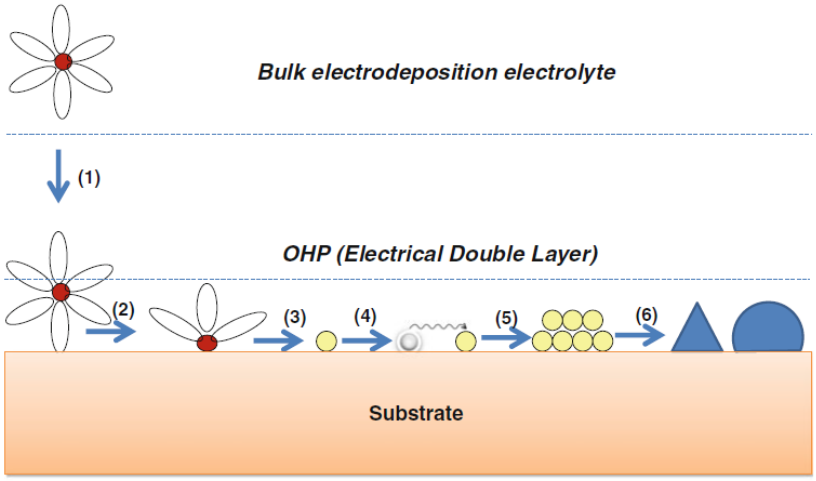

Figure I-18. *Nucleation and growth diagram during electrodeposition*

In step (1), ion transport from the bulk electrolyte to the outer Helmholtz plane (OHP). When ions approach the cathode and they cross the charged interface (step 2), they become condensed on the substrate thus, they must release the solvated water (step 3). In step 4, ad-atoms are formed and diffused on the substrate surface. Further progress will replace all hydration water molecules by coordinating metal atoms until their full accommodation number. This results in the nucleation of stable atomic clusters (step 5). In step 6, irreversible

incorporation of ad-atoms in the atomic lattice and establishing a peculiar crystallographic texture and morphology or electrocrystallisation.

I.3.2.3 Effect of additives

Additives have a huge impact on the electrodeposited film because of the adsorption phenomenon at the cathode surface. The first type of adsorption is chemisorption, in this case the additive forms a covalent bond, thus chemical combination between the electrode surface and the adsorbates where electrons are shared and a new electronic configuration may be formed due to this sharing. The second type of adsorption is physisorption which consist of Van der Walls bonds formation between the substrate and the adsorbates, and in this case, there is no electron sharing [21].

In microelectronics, usually the following additives are used during copper electroplating (Figure I-20):

- **Accelerator**: Common accelerators are Bis(3-sulfopropyl) disulfide (SPS), 3-mercapto-1-propanesulfonate (MPS), and 3-(2-benzthiazolylthio)-1-propanesulfonic acid (ZPS). As shown in Figure I-19, the standard molecular structure of the accelerator includes the terminal anion group (sulfonic acid) to attract the Cu ions in the electrolyte and the head sulfur-containing group capable of adsorbing on the Cu deposit. The adsorptive head group to the metal surface is HS, –S–S–, and –C–S–C– for MPS, SPS, and ZPS, respectively. Dow et al [22] examined the effect of SPS through post-addition of SPS in a bath originally containing PEG and Cl− ions. They found that the over-potential decreased with the addition of SPS, suggesting that SPS has a highly competitive adsorption ability capable of replacing the PEG adsorption sites.

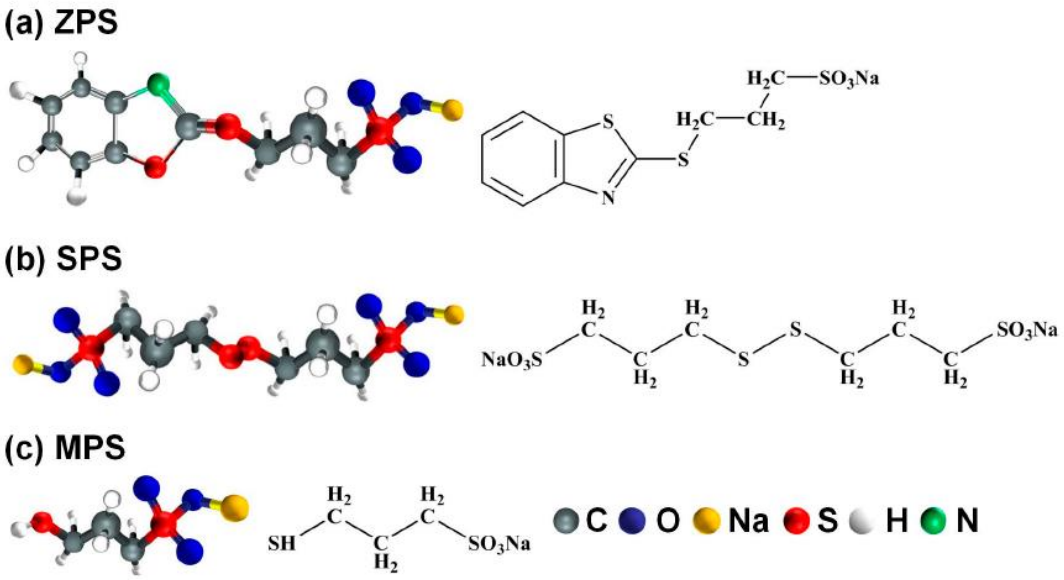

Figure I-19. *Molecular structures of three accelerators: (a) ZPS, (b) SPS, and (c) MPS.*

- **Suppressor**: Suppressor is typically a high-molecular polymer with a molecular structure of ethylene or propylene glycol, such as polyethylene glycol (PEG) or polypropylene glycol (PPG). In the electroplating process, the suppressor must operate synergistically with the Cl− ions in order to have a chelation reaction with the cuprous ions (Cu+) in order to suppress the Cu deposition [23]. Studies have shown that PEG molecules have a column-shaped morphology, because the plating solution is free of Cl− ions. However, in the presence of Cl− ions, a spherical form of PEG was observed by Kelly et al [24]. The Cu ions were encapsulated in the spheres by creating a PEG-Cu^{+}-Cl^{-} complex, and thus the Cu deposition rate was suppressed. In other words, a higher overpotential was required to minimize the reaction of Cu atoms to the deposit surface. Moffat et al. proposed that the complex acted as a passive film on the deposit surface, which controlled Cu rate deposition [25]. The suppression of the deposition rate is also possibly due to competition of adsorptive PEG molecules for active sites on the deposition surface [26]. In 2005, Dow et al [22] investigated the impact of the molecular weight of PEG and found that the higher the molecular weight of PEG, the greater are the suppressive effect (Figure I-20).

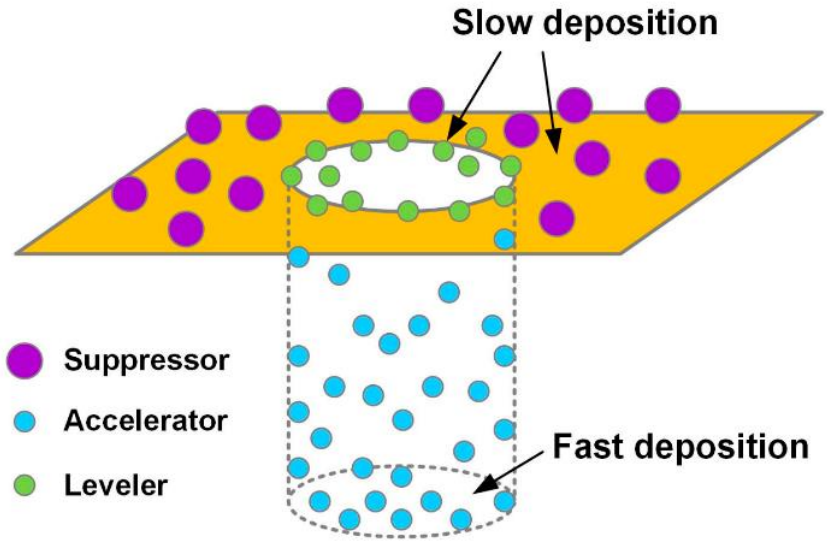

Figure I-20. *Diagram of the adsorption behavior of additives [9].*

- **Leveler:** Leveler is an azole compound that comprises nitrogen atoms (Figure I-21) as demonstrates the molecular structure of the commercial grader JGB (Janus Green B) [22]. Due to the positively charged amine (or nitro) group, the leveler tends to "automatically" adsorb to the region where the current is concentrated. On the other hand, the suppressor, i.e. PEG, needs to co-operate with Cl− ions in a forced convection environment to allow its adsorption on the deposition surface. During via electroplating process, the leveler primarily adsorbs at via opening and acts as a suppressor to inhibit the Cu deposition rate around the via opening. Local suppression of Cu deposition can prevent the formation of void or seam inside the through [23].

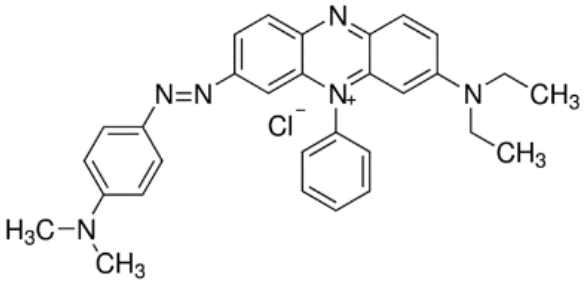

Figure I-21. *Structure of a commercial leveler (Janus Green B).*

To manage the vias filling and prevent the apparition of voids and seams, concentration of additives should be carefully studied (see Figure I-22) [27],[28].

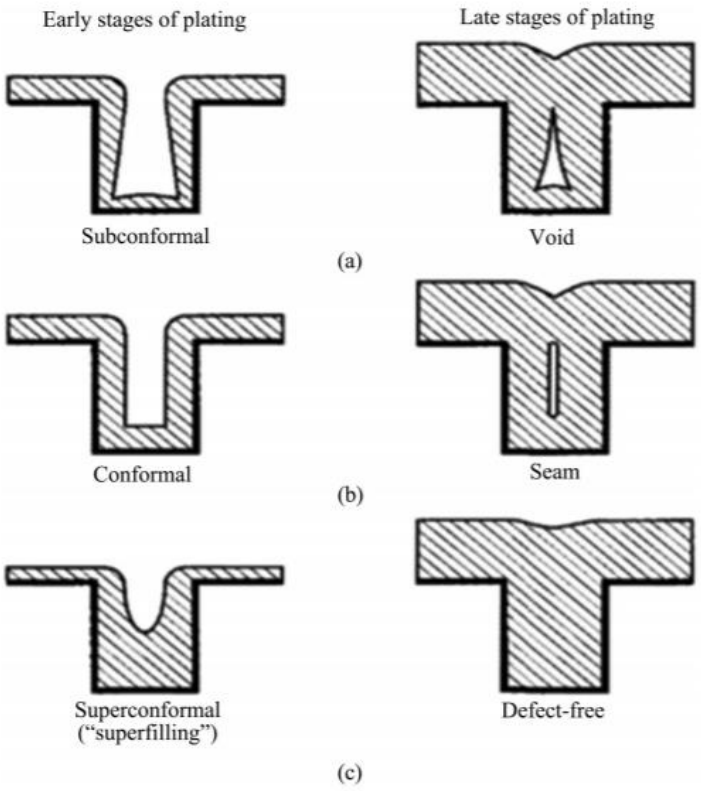

Figure I-22. *Different scenarios in electroplating. (a) faster deposition, (b) conformal deposition rate and (c) faster deposition rate at the bottom.*

I.3.2.4 Factor effecting electroplating

In electroplating, the conformal film depends on several parameters:

- **Current density distribution impact**

In electroplating current density will vary from point to point on the cathode surface since metal ions adsorption at certain favored sites. Current is concentrated at edges of the object (Spherical diffusion of species) and it tends to be low in recesses (vias and cavities) due to the planar diffusion (see Figure I-23). Thus, current distribution plays an important role in determining uniform deposits. Low current will lead to poor coating while high current density favors higher impurity presence in the film. The reason for this is once above the limiting current density value, hydrogen evolution reaction increases and raises pH at the cathode causing metal hydroxides precipitation at the deposits. The optimum current density range is depending on the bath composition and on the operating process condition.[29]

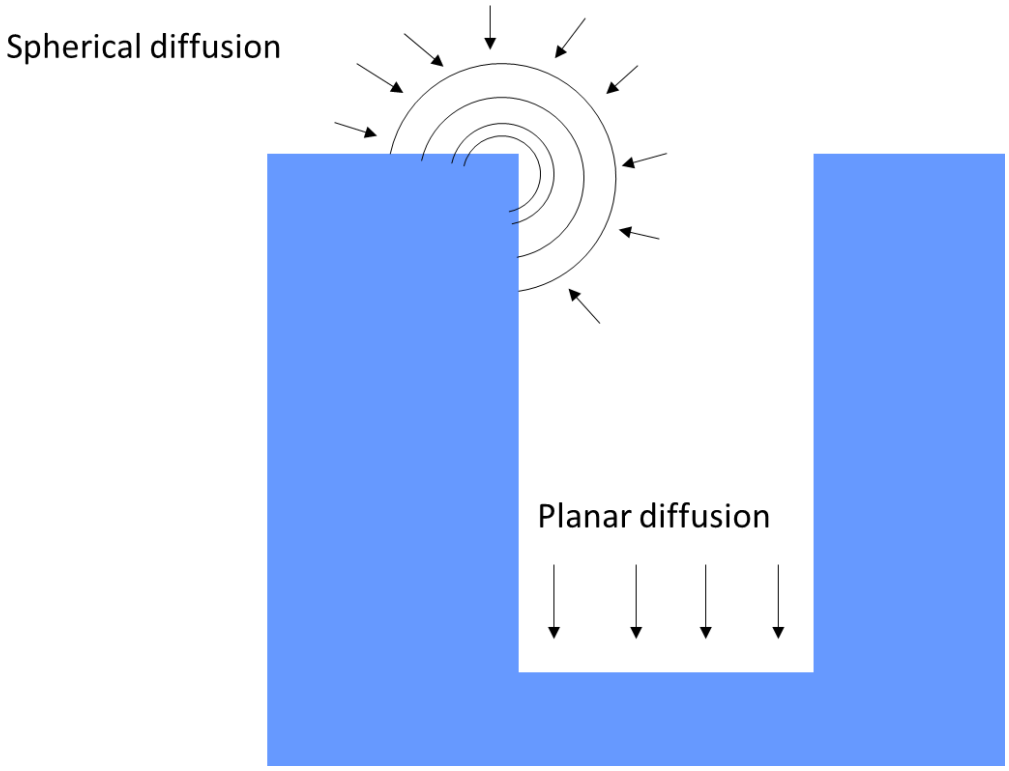

Figure I-23. *Diffusion type in the bottom and the edges.*

- **Impact of pH**

pH variation during electroplating influences the HER voltage, the precipitation of basic inclusions and the decomposition of the metal complex or hydrates from which the metal is electroplated. When pH increases due to HER, metal hydroxides precipitation may occur at the interface cathode/electrolyte, which leads to the co-deposition of metal hydroxides with the plated metal. Therefore, buffers are mandatory to decrease these pH changes. Other than the impact of hydrogen on the plating rate, it often also affects the deposited structure by causing spongy or powdery deposits. Depending on the bath composition, the pH difference between the electrolyte and the cathode becomes stabilized or continues to increase with increasing current density [29], [30].

- **Effect of agitation**

As known in electrochemistry agitation replenishes metal ions at the cathode and reduce the thickness of the diffusion layer. In the case of a cathode with vias, Chia-Fu Hsu studied the velocity variation between the bottom and the top of via. It was found that the velocity is at maximum at the top and decreases as we move towards the bottom [31] (see Figure I-24).

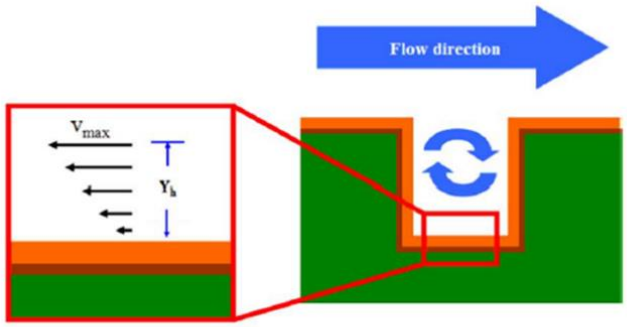

Figure I-24. *Velocity variation between the top and the bottom of the via.*

The lower the velocity is, the fewer metal ions are at the bottom of the via compared to the top. So, the concentration of metallic ions is lower at the bottom, and according to electrochemistry principles when the concentration of the electrolyte is decreased, the amount of deposited metal increases. In dual-damascene process the deposition rate is higher at the bottom than the top of the via, which leads to bottom-up filling.

I.4 References

[1] J. Bardeen and W. H. Brattain, “The Transistor, A Semi-Conductor Triode,” *Phys. Rev.*, vol. 74, no. 2, pp. 230–231, Jul. 1948, doi: 10.1103/PhysRev.74.230.

[2] W Shockley, M. Sparks, and G. K. Teal, “p-n Junction Transistors,” *Physical Review*, pp. 151-164, 1951.

[3] J. Bardeen and W. Brattain, “Physical Principles Involved in Transistor Action,” *Physical Review*, pp. 1208-1226, 1949.

[4] G. E. Moore, “Cramming more components onto integrated circuits,” p. 3, 2006.

[5] M. Aimadeddine *et al.*, “Robust integration of an ULK SiOCH dielectric (k=2.3) for high performance 32nm node BEOL” in *2007 IEEE International Interconnect Technology Conferencee*, Jun. 2007, pp. 175–177, doi: 10.1109/IITC.2007.382382.

[6] J. D. Meindl, “Georgia Institute of Technology,” *IEEE MICRO*, p. 8, 2003.

[7] J. D. Meindl, “Low power microelectronics: retrospect and prospect,” *Proc. IEEE*, vol. 83, no. 4, pp. 619–635, Apr. 1995, doi: 10.1109/5.371970.

[8] K. Banerjee, S. J. Souri, P. Kapur, and K. C. Saraswat, “3-D ICs: a novel chip design for improving deep-submicrometer interconnect performance and systems-on-chip integration,” *Proc. IEEE*, vol. 89, no. 5, pp. 602–633, May 2001, doi: 10.1109/5.929647.

[9] T. Gupta, “The Copper Damascene Process and Chemical Mechanical Polishing,” in *Copper Interconnect Technology*, New York, NY: Springer New York, 2009, pp. 267–300.

[10] R. H. Dennard, J. Cai, and A. Kumar, “A Perspective on Today’s Scaling Challenges and Possible Future Directions,” in *Handbook of Thin Film Deposition*, Elsevier, 2012, pp. 3–18.

[11] J. A. Davis *et al.*, “Interconnect limits on gigascale integration (GSI) in the 21st century,” *Proc. IEEE*, vol. 89, no. 3, pp. 305–324, Mar. 2001, doi: 10.1109/5.915376.

[12] H. Ceric and S. Selberherr, “Electromigration in submicron interconnect features of integrated circuits,” *Mater. Sci. Eng. R Rep.*, vol. 71, no. 5–6, pp. 53–86, Feb. 2011, doi: 10.1016/j.mser.2010.09.001.

[13] C. Christiansen, B. Li, and J. Gill, “Blech Effect and Lifetime Projection for Cu/Low-K Interconnects,” in *2008 International Interconnect Technology Conference*, Burlingame, CA, USA, Jun. 2008, pp. 114–116, doi: 10.1109/ IITC.2008.4546941.

[14] “Reliability and Failure of Electronic Materials and Devices - 2nd Edition.” https://www.elsevier.com/books/reliability-and-failure-of-electronic-materials-and-devices/ohring/978-0-12-088574-9 (accessed Aug. 27, 2020).

[15] B. M. says, “The Cobalt Wave Continues,” *EEJournal*, Jul. 16, 2018. https://www.eejournal.com/article/the-cobalt-wave-continues/ (accessed Aug. 21, 2020).

[16] “Godon - Relations StructureCompositionPropriétés de revê.pdf.” .

[17] M. S. Chandrasekar and M. Pushpavanam, “Pulse and pulse reverse plating—Conceptual, advantages and applications,” *Electrochimica Acta*, vol. 53, no. 8, pp. 3313–3322, Mar. 2008, doi: 10.1016/j.electacta.2007.11.054.

[18] A. M. Alfantazi, G. Brehaut, and U. Erb, “The effects of substrate material on the microstructure of pulse-plated Zn–Ni alloys,” *Surf. Coat. Technol.*, vol. 89, no. 3, pp. 239–244, Mar. 1997, doi: 10.1016/S0257-8972(96)02894-0.

[19] P. T. Tang, M. Jaskula, M. Kubiczek, I. Mizushima, K. Pantleon, and M. Arentoft, “Pulse reversal plating of nickel–cobalt alloys,” *Trans. IMF*, vol. 87, no. 2, pp. 72–77, Mar. 2009, doi: 10.1179/174591909X424834.

[20] J. O. Bockris, B. E. Conway, and R. E. White, Eds., *Modern Aspects of Electrochemistry*. Springer US, 1995.

[21] Schlesinger M, Paunovic M. Modern electroplating. John Wiley & Sons; 2011.

[22] W.-P. Dow, M.-Y. Yen, W.-B. Lin, and S.-W. Ho, “Influence of Molecular Weight of Polyethylene Glycol on Microvia Filling by Copper Electroplating,” *J. Electrochem. Soc.*, vol. 152, no. 11, p. C769, 2005, doi: 10.1149/1.2052019.
[23] H. Lee and C.-M. Chen, “Impurity Effects in Electroplated-Copper Solder Joints,” *Metals*, vol. 8, no. 6, p. 388, May 2018, doi: 10.3390/met8060388.
[24] J. J. Kelly and A. C. West, “Copper Deposition in the Presence of Polyethylene Glycol,” *J Electrochem Soc*, vol. 145, no. 10, p. 5, 1998.
[25] T. P. Moffat, D. Wheeler, and D. Josell, “Electrodeposition of Copper in the SPS-PEG-Cl Additive System,” *J. Electrochem. Soc.*, vol. 151, no. 4, p. C262, 2004, doi: 10.1149/1.1651530.
[26] J. W. Gallaway and A. C. West, “PEG, PPG, and Their Triblock Copolymers as Suppressors in Copper Electroplating,” *J. Electrochem. Soc.*, p. 8.
[27] J. K. Jhothiraman and R. Balachandran, “Electroplating: Applications in the Semiconductor Industry,” *Adv. Chem. Eng. Sci.*, vol. 09, no. 02, pp. 239–261, 2019, doi: 10.4236/aces.2019.92018.
[28] E. Delbos, L. Omnès, and A. Etcheberry, “Copper Electrodeposition Parameters Optimization for Through-Silicon Vias Filling,” *ECS Meet. Abstr.*, vol. MA2009-02, no. 26, p. 2177, Jul. 2009, doi: 10.1149/MA2009-02/26/2177.
[29] S. Kumar, S. Pande, and P. Verma, “Factor Effecting Electro-Deposition Process,” p. 4.
[30] W. Street, “National Eibrary of Canada Acquisitions and Bibliographie Services,” p. 117.
[31] C.-F. Hsu, W.-P. Dow, H.-C. Chang, and W.-Y. Chiu, “Optimization of the Copper Plating Process Using the Taguchi Experimental Design Method: I. Microvia Filling by Copper Plating Using Dual Levelers,” *J. Electrochem. Soc.*, vol. 162, no. 10, pp. D525–D530, 2015, doi: 10.1149/2.0531510jes.

CHAPTER II Cobalt electrochemical investigation and mechanism comprehension

CHAPTER II COBALT ELECTROCHEMICAL INVESTIGATION AND MECHANISM COMPREHENSION 48

II.1 INTRODUCTION 49

II.2 COBALT ELECTROCHEMICAL INVESTIGATION 52

II.2.1. Cyclic voltammetry 52

II.2.2. Cobalt concentration impact 60

II.3 COBALT ELECTRODEPOSITION MECHANISM 70

II.3.1. Current efficiency 70

II.3.2. Nucleation and growth 74

II.3.3. Bath temperature impact 77

II.4 CONCLUSION 79

II.5 REFERENCES 81

II.1 Introduction

The processes of electrolytic deposition are at the heart of Electrochemical Science. Electrochemical deposition can be now considered as a very practical method in surface coating present in a lot of technological domains. Compared to other coating methods it is often a cheaper choice, which is however able to produce dense deposits with good mechanical properties. Understanding them, then controlling them requires looking in detail at multiple interdependent parameters, which will decide the nature and the quality of the final electroplated film. Thus the concepts of interfacial electrochemistry, the kinetic considerations, the polarization modes, the morphological evolutions during growth, the progressive modifications of electrostatic or chemical conditions at the moving interface and numbers of other parameters (solution side or electrode side) are to be considered in an equivalent way in order to understand the deposition process quantitatively. Electroplating is therefore a very complex discipline that may be an "art", both in terms of the diversity of plating-bath formulations and the diversity of the electrochemical engineering choices involved.

Electrolytic deposition can generate films of metals, semiconductors, polymers which can be used either directly or after treatment. Lot of metals: gold, silver, Copper, Nickel etc., can be electrodeposited with excellent final film qualities [1]. Cobalt is also to be included in this top list of "electrodeposited metals". Indeed, electrochemically deposited cobalt and its alloys are about the most used decorative coatings, and micromachining materials. Cobalt is used in the fabrication of materials required for diverse applications, ranging from the production of magnets, hard metals, superalloys, and gas turbine components to the manufacturing of lithium-ion batteries and industrial catalysts [1], [2].

The electrodeposition of cobalt is mostly performed in acidic electrolytes containing Co salts (sulfates, chloride, sulfamates) with boric acid [3]. Many researchers study the impact of the applied current and the pH on cobalt electrodeposition. It was found that a high electrolyte pH increases the amount of side hydroxide formation. *Vicenzo et al.* [4] have studied the effect and evolution of hydrogen reaction and the growth model deeply. It was found that the adsorbed hydrogen impacts the structure of the formed cobalt and affects its crystalline structure. This point is not specific to the Co electrodeposition, but it is an important parameter to consider for this metal.

As already presented in chapter I, in the microelectronics industry, the electroplating approach has particularities, even specificities compared to electroplating in other fields. These

particularities are like those of copper electroplating in interconnections. Among these specificities, the ability to deposit the metal while considering the shape factors. As for copper, it is an enormous challenge, which is the key to a mature technology. The second important particularity is to ensure the continuity of the deposited metal layers. These aspects require us to dominate electroplating with a nanometric scale precision. Concerning the copper technology, it is almost entirely controlled. Concerning the cobalt as it is a recent challenge, many fundamental and application aspects are still open to understanding, etc. Indeed, the R&D engineers in 'Co' microelectronics are limited by time because of several constraints. Among these constraints, the novelty of cobalt electroplating results in a lack of knowledge in this field. In addition to the microelectronic industry's critical advancement imposes a certain rhythm on research and development. So fundamental and industrial application are totally mixed at this time compared to the copper story it is a very different context.

aveni® already has the expertise in copper electroplating, and by considering the evolution of the context, it has also developed bath formulations for cobalt electroplating [5]–[7]. These formulations have some specificities and consequently are PI protected. The first one concerns a global formulation of acidic chemistry of cobalt called *Cowave* and the second one involves the development of a particular additive dedicated to the Cowave cobalt chemistry. The cobalt films obtained by Cowave is qualified by X-ray diffraction (XRD) and by electrical measurements. However, there is an insufficiency of fundamental knowledge in the physicochemistry of nanometric cobalt films in microelectronics. For the Cowave chemistry, there is a need to specify some points of the solution properties and thus of the deposited films. This need is due to the ultimate miniaturization of feature sizes, which requires us to well understand and control the nanometric cobalt deposit and its following behaviors [8].

One of the important statements made by aveni® engineers on cobalt electrodeposition is the dependence of the current efficiency on the applied current. However, this statement needs additional data to deepen its understanding. Contrary to thick cobalt films (200-400 nm) studied previously by aveni® as by many electrochemist groups, several questions arise for thinner films of a few nanometers thick, namely, their reactivity toward air and/or final plating chemistries. The second piece of evidence is to understand best the role of the additive added to *Cowave*.

For aveni®, several challenges must be overcome to study thin cobalt films, like the necessity to use external purchased wafers with specific thicknesses we wanted to explore.

However, this operation is costly and time-consuming (shipping), resulting in investigation delays. To optimize time, the following question is asked: **is it possible to make controlled thin cobalt films with our own resources and in total independence?**. To answer this question, it is mandatory to do high precision electrochemistry which is able to provide thick, thin, ultra-thin films as wanted.

An engineered approach was developed to face all these challenges. Firstly, this consists of working on cyclic voltammetry (CV) techniques to take advantage of depositing and dissolving cobalt films. This step will help us to manage current efficiencies. Secondly, we will attempt to electrodeposit and control homogeneous cobalt films with different nanometric thicknesses. We will then study the physicochemistry of the obtained thin films and investigate their behavior when immersed in different chemistries. Our methodology choice consists of using a gold working electrode to understand the electrochemistry of the cobalt electroplating and develop different film thicknesses for the following studies. However, to deposit and control very thin nanometric thicknesses and study their eventual dissolution phenomenon, a more powerful tool than CV is needed.

For this reason, we decided to use electrochemical quartz crystal microbalance (EQCM). This tool will provide us direct access to the needed mass information while doing electrochemistry. EQCM has been widely used for the characterization of copper electrodeposition [9]. However and surprisingly, it is not easy to find this technique in cobalt electroplating investigations. Using a quartz microbalance technique for cobalt electroplating study makes this technique more original due to the possibility of studying the nanometric obtained films by different techniques of characterization like XRD, XPS, nano-Auger…

In this chapter, three critical parameters for the cobalt electroplating control are presented. The current efficiency evolution as a function of applied potential, the nucleation and growth mechanism, and parasitic reactions are studied. As it is crucial to assess the impact of electroplating bath on Co deposition, the temperature and the Co^{2+} concentration are also slightly investigated.

After having reasonable control of the cobalt electroplating process and understanding the impact of the different parameters on it, the behavior of nanometric Co films in different acidic and alkaline solutions are explored using both EQCM and x-ray photoelectron spectroscopy. The main goal of this study is to assess a thin cobalt seed layer immersion in well-known

chemistry. It is a very important point for the aveni technology and the approach developed in this thesis combining electrochemical and surface science information is a main point.

II.2 Cobalt electrochemical investigation

II.2.1. Cyclic voltammetry

To study the electrochemical behaviors of the aveni*@Cowave* bath we started by using a potentiostatic mode which allows to perform Cyclic Voltammetry (CV). This electrochemical method provides a well adapted experimental configuration for an initial easier and efficient investigation of the plating performances of the aveni*@Cowave* formulation. Then all CV electrochemical tests used a standard three-electrode configuration cell with a silver chloride electrode (AgCl KCl saturated) from Metrohm as a reference electrode. A 3 cm^2 platinum sheet was used as a counter electrode. During the first experiments, we started with a rotating gold disc as a working electrode with a surface of 0.196 cm^2. It allowed initial exploration of the electrochemical behaviors but with the limitation of very small size for a fine plating process understanding. As the responses under rotation were not our priority, we decided to switch to a gold-coated crystal working electrode for better cell design, for larger interacting surface and for a better electrical conductivity system. The gold-coated electrodes we used were always circular; they had an area of 1.37cm^2. Consequently, the planar diffusion was emphasized so edge effects were minimized, and following mappings of the film quality were more easily performed. Moreover, our gold-coated electrodes were also oscillating quartz working electrodes, which allowed the very performing EQCM method, which combines mass and electrochemical information. This choice also allows a vertical positioning, and it allowed us to have a visual *in situ* tracking of the electrodeposition process. It was very practical and helpful, as seen below. Moreover, batch of quasi-identical electrodes were available for direct result comparison. As expected, it should be noted that the obtained CV results with the rotating gold disc electrode are precisely equivalent to those performed on the gold quartz microbalance electrode.

Before each experiment, the working electrode is electrochemically cleaned in 1M HCl by 100 cycle scanning between -0.8 and 1 $V_{/Ag/AgCl}$ at a scanning rate of 100 mV/s. To ensure the stability of the reference electrode, it was checked before and after each experiment. The volume of the electrolyte was 100 ml.

Only *Cowave* bath of aveni®, was used to electro-deposit cobalt. It contains 9.5 g/L of ($CoCl_2$, $6H_2O$)/(0.04 mol/L) for the Virgin Makeup Solution (VMS). To *Cowave* VMS an

additive is added to fill the interconnect structures. note that in this work we will focus only on the *Cowave* VMS solution (without additive). The pH of *Cowave* /VMS is 2.2. By bubbling nitrogen, dissolved oxygen amount decreased in the electrolyte (it is never totally removed with our experimental set up) from the cobalt electrolyte. This de-oxygenation step is applied once before electrodeposition. Before each experiment, conductivity and pH measurements are checked using MasterLAb CDM210 conductivity meter and "pH 150" Eutech pH meter respectively. The *Cowave* solution's pH is equal to 2.2±0.1, and the conductivity value is 8 mS/cm.

An analysis of the cobalt deposition process was performed at room temperature in the *Cowave* VMS bath. Linear potential sweeps are generally conducted at 20 mV/s. All the potential ramps associated with the voltammograms started from the open circuit potential (OCP) E_{OCP} = -0.4 V±0.01/$_{Ag/AgCl}$. Figure II-1 is specific of a CV curve over a large potential range which includes cathodic and anodic features in the same voltammogram, which details are totally related to Co containing solution. In Figure II-1 The electrode potential moved from OCP towards −1.8 V/$_{Ag/AgCl}$. Next, the direction of scanning was inversed and it continued positively until the potential of 0.8 V/$_{Ag/AgCl}$. Generally, voltammograms were performed for 10 cycles over the same potential range, and the calculated error for the current density is less than 2%. The current density error is estimated by Eq. II-1:

$$error(\%) = \frac{j_{max} - j_{min}}{j_{max} + j_{min}} \qquad \textit{Eq. II-1}$$

Where j_{max} and j_{min} are the maximum and the minimum current densities obtained during 10 cycles voltammograms.

We must point out that the OCP value is very reproducible, and this value is characteristic of the Co^{2+}/Co couple on gold working electrodes in Cowave VMS solution. As shown in Figure II-1, there are two parts in our voltammogram, one with negative overvoltages and the other with positive overvoltage toward the OCP. The negative one's presents a well-defined cathodic current contribution, and the positive one's has a characteristic anodic current.

The specific shape of the cathodic contribution is related to the presence of Co^{2+} cations in solution. The anodic contribution is totally related to a previous cathodic sequence. Indeed, the anodic response is only observed if a previous complete cathodic sequence has been performed.

In negative overvoltages, two cathodic regions are noticed, the first one with low current densities then the second region with higher current densities with a specific final wave. In this

first region, the current density begins to rise at approximately -0.5 $V_{/Ag/AgCl}$ position. The cathodic current presents a well-defined hysteresis discussed below. Later in the text, we will prove that in this region, there is no cobalt deposition. This study allowed us to say that the low current densities in this range of potentials are related to parasitic reactions that we will discuss below.

In this intermediate acidic medium, this low current contribution can be associated with H^+ reduction and maybe to the reduction of the residual dissolved oxygen. As the negative sweep continues, the current increases moderately until the shoulder's formation at approximately -0.8 V. As it is specific of the Co^{2+} containing bath, it is suggested that it is due to the adsorption of Co^{2+} ions on the gold working electrode, the shoulder may be associated with the hindrance of the cobalt nucleation process [10]. Negatively to this first cathodic potential zone, the current presents a well-defined threshold which continues to increase until the apparition of a characteristic peak A at -1.65 $V_{/Ag/AgCl}$. Below, we will confirm that the intensity of the peak A totally depends on the Co^{2+} concentration in the electrolyte. Thus, we can assume that this peak is associated with Co^{2+} limiting reduction current associated to the Co film deposition.

In the positive overvoltage zone, we observe a principal asymmetrical peak B with a typical triangular shape at around 0.60 V. The observed peak increases linearly with the potential sweeping, which is associated with the system's resistivity. After the anodic current increase, a brutal current drop is observed at a specific potential. It was established that this potential is dependent on the cobalt deposited quantity. This peak is typical of the metallic dissolution of cobalt. It is with a total relation of the system's cathodic behavior.

The voltammogram of the Figure II-1 led us to investigate the deposition and the dissolution of cobalt in *Cowave* VMS chemistry. To see the correlation between proton reduction and cobalt deposition, voltammetry was done in cobalt-free electrolyte and compared to that of the *Cowave* VMS plating electrolyte. Figure II-2 presents cyclic voltammograms at pH 2.2 in both solutions. The cobalt-free electrolyte contained HCl. The results show the current densities evolution as a function of the applied potential vs. AgCl on a gold working electrode. This study is focused only on the negative overpotential region. The black curve represents the current density evolution in *Cowave* VMS chemistry at 20 $mV.s^{-1}$. However, the red curve is the current density evolution in cobalt-free solution HCl at the same pH 2.2.

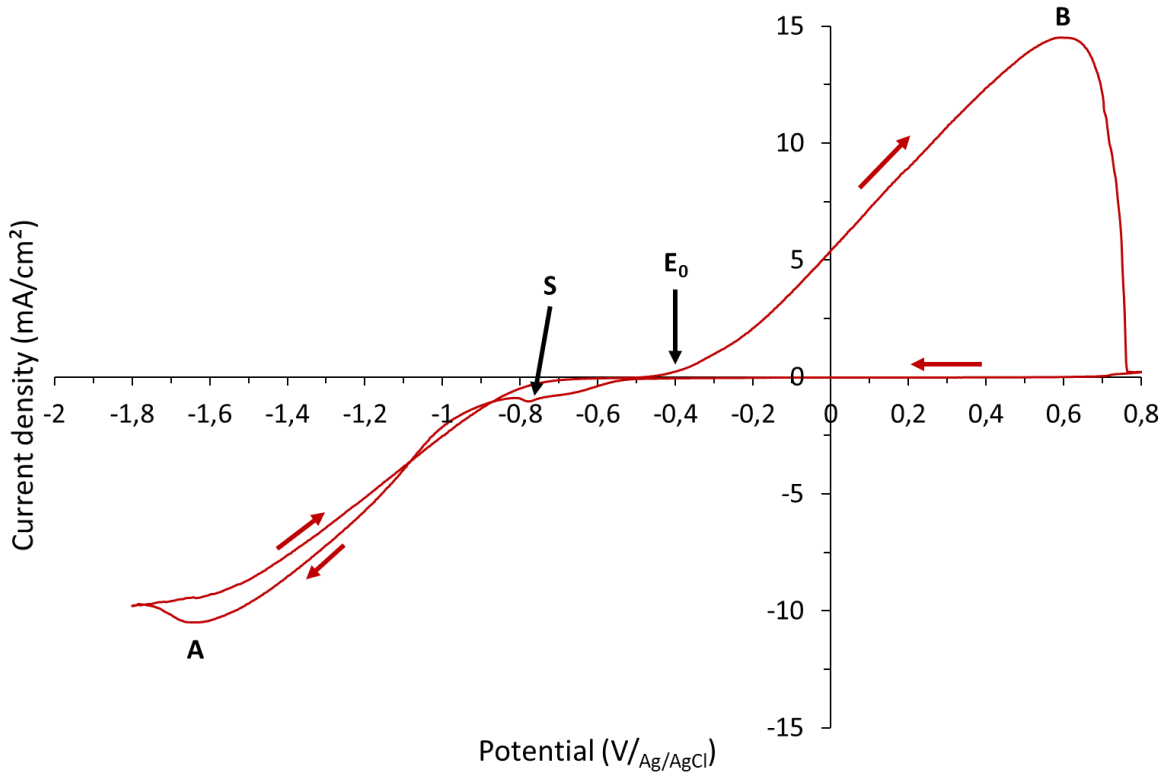

Figure II-1. *Cyclic voltammogram for Au substrate at 20 mV/s in VMS Cowave bath*

Note that the voltammograms presented in Figure II-2 are only for the first scan. However, from the second scan onwards, the current response is more regular in HCl while less regular in Cowave VMS. This phenomenon is noticed only in the low cathodic domain, and we assume that it is related to the working electrode nature. Which remains unchanged in HCl (gold), and it changes from gold to cobalt after the first scan. In Cowave VMS solution, the current increases after reaching -0.5 $V_{Ag/AgCl}$, whereas, in HCl voltammogram, the current increases after -0.4 V. The 100 mV difference is probably related to the absorption of Co^{2+} ions that delayed the H^+ reduction reaction. The second difference is noticed at -0.8 V, where a shoulder (S) is formed in Cowave VMS solution; however, the current continues to rise in HCl solution. Further studies will prove that this potential (-0.8 V) corresponds to the beginning of cobalt deposition. It is also clear that for potentials more negative than -1.1 V, the current density values in the presence of Co^{2+} are more intense with a well defined threshold. This difference in current densities evolution is related to the cobalt ion's reduction.

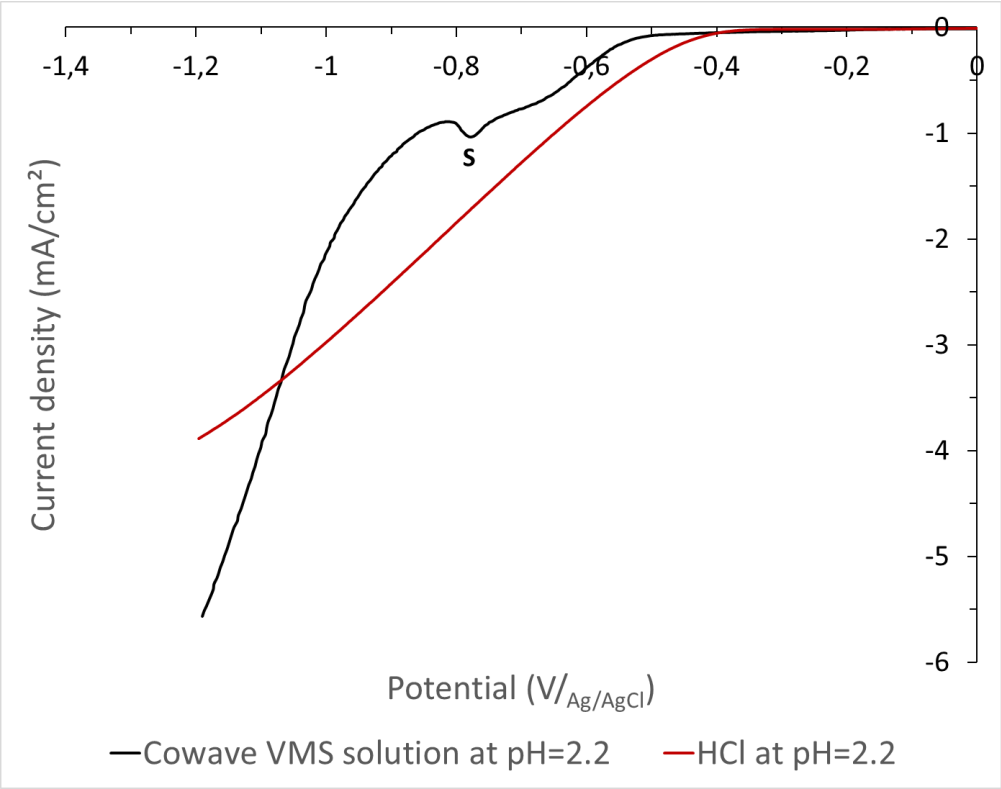

Figure II-2. *Voltammograms on Au: in Cowave VMS (black) and HCl (red) at pH2.2, scan rate 20 mV.s^{-1}*

To confirm previous results, an Electrochemical Quartz Crystal Microbalance (EQCM) is coupled with the three-electrodes electrochemical cell used before. EQCM experiments were done using a Maxtek® research QCM with 5 MHz gold sensing electrodes (1.37 cm²). All experiments were done at room temperature, without compensation for cell resistance, and without solution stirring. EQCM will allow us to monitor small mass changes on the surface of a coated quartz crystal. Including a high-sensitivity mass sensor (0.04 ng of cobalt) while giving us the option to simultaneously run electrochemical experiments to gain insight into what drives mass changes within films.

According to the Sauerbrey equation (Eq. II-2), from the change in the frequency response as a function of time, the Maxtek RQCM software calculates the frequency variation, thus the mass evolution of the deposited species.

$$\Delta f = \frac{-2f_0^2 \Delta m}{A\sqrt{\mu_i \rho_i}} = -K\Delta m \qquad \textit{Eq. II-2}$$

Where f_0 is the resonant frequency of the quartz crystal, A the piezoelectric active area, μ_i the shear modulus of the quartz, K the experimental mass coefficient, and ρ_i is the density of quartz, Δm and Δf are the mass and the frequency change, simultaneously.

The µ-balance or EQCM is a piezoelectric material that can be made to oscillate at a defined frequency by applying an appropriate voltage, usually via metal electrodes. The oscillation frequency can be affected by the addition or removal of small amounts of mass onto the electrode surface. A voltammogram, coupled with delta frequency variation, is illustrated in Figure II-3. The frequency variation remains unchanged during the first increase of current density in the interval [-0.8 V, -0.5 V]. This is associated with no mass change at this interval and the no deposition of cobalt. Thus the first region is specific of parasitic reactions.

The suggested parasitic reactions are: the first reaction (Eq. II-3) of proton reduction in acidic media and the second reaction (Eq. II-4) related to the dissolved oxygen reduction that we estimate negligible after bubbling with N_2.

$$2H^+_{(aq)} + 2e^- \rightarrow H_{2\,(g)} \qquad \textit{Eq. II-3}$$

$$O_{2\,(g)} + 4H^+ + 4e^- \rightarrow 2H_2O_{(l)} \qquad \textit{Eq. II-4}$$

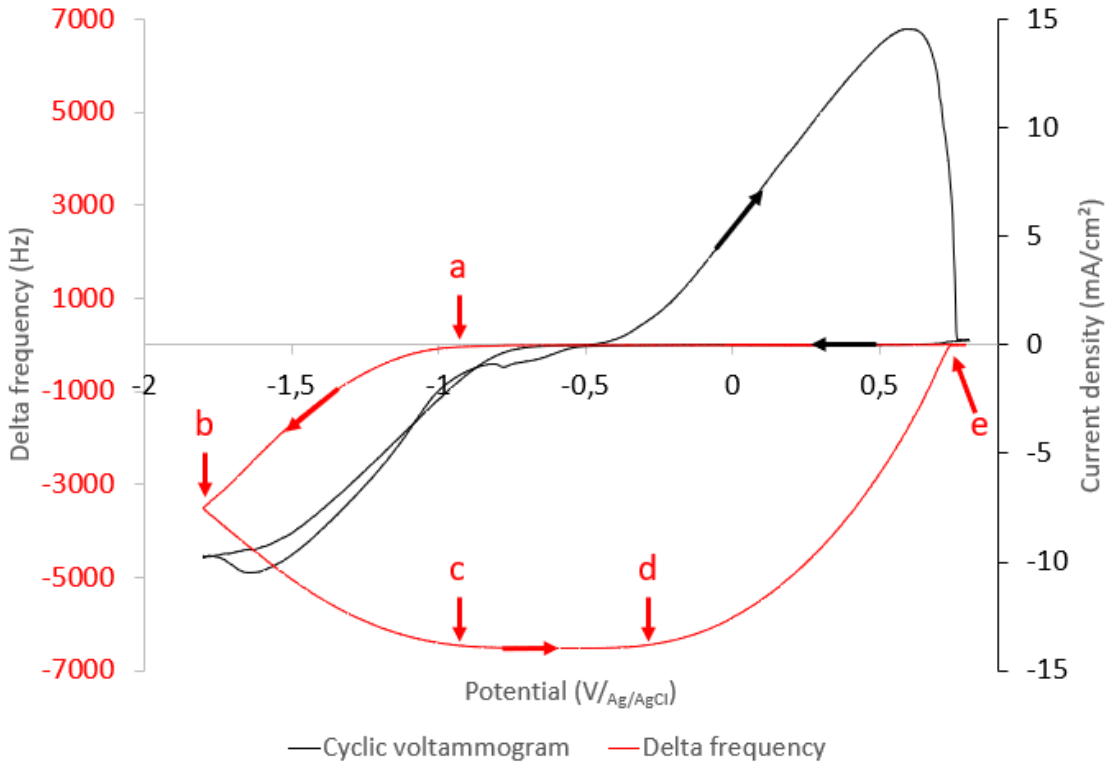

Figure II-3. *Voltammogram of Au electrode: in Cowave VMS chemistry (black) and associated delta frequency variation (red), scan rate 20 mV.s^{-1}.*

Delta frequency starts to decrease at approximately -1.0 V/Ag/AgCl (point a). According to Sauerbrey law, this decrease is significant for the mass increase. The delta frequency continues to decrease until -1.8 V (point b), which is the reverse scan's potential. Since the potential

applied is more negative than -1.0 V, the frequency change decreases until point c, the equivalent mass increases. From point c to point d, the delta frequency is stable during the reverse scan, which is significant for no cobalt mass change and no cobalt deposition. The mass remains unchanged because this region of overpotentials is associated only with hydrogen evolution reaction. When -0.4 $V/_{Ag/AgCl}$ is reached, delta frequency starts to increase, significantly of mass diminution. This diminution is related to cobalt film dissolution. When reaching 0.7 V (point e), delta frequency variation returns to the same value as the starting potential, and the mass change is reversible. According to this result, it can be concluded that there is no oxides formation within the detection limit of the microbalance. At this point (e) the current density drop to 0, which also confirms the dissolution of all deposited cobalt.

One of the critical parameters is the starting deposition potential of cobalt. This value will serve us to study the nucleation mechanism of cobalt electroplating. To explore this value, EQCM is coupled with the chronoamperometry (CA) technique. This technique is applied in the region where the delta frequency starts to decrease. -0.7, -0.75 and, -0.8 $V/_{Ag/AgCl}$ are applied for 10 minutes on Au working electrode in Cowave VMS solution. Figure II-4 shows the mass change and the thickness of the obtained film during the CA process.

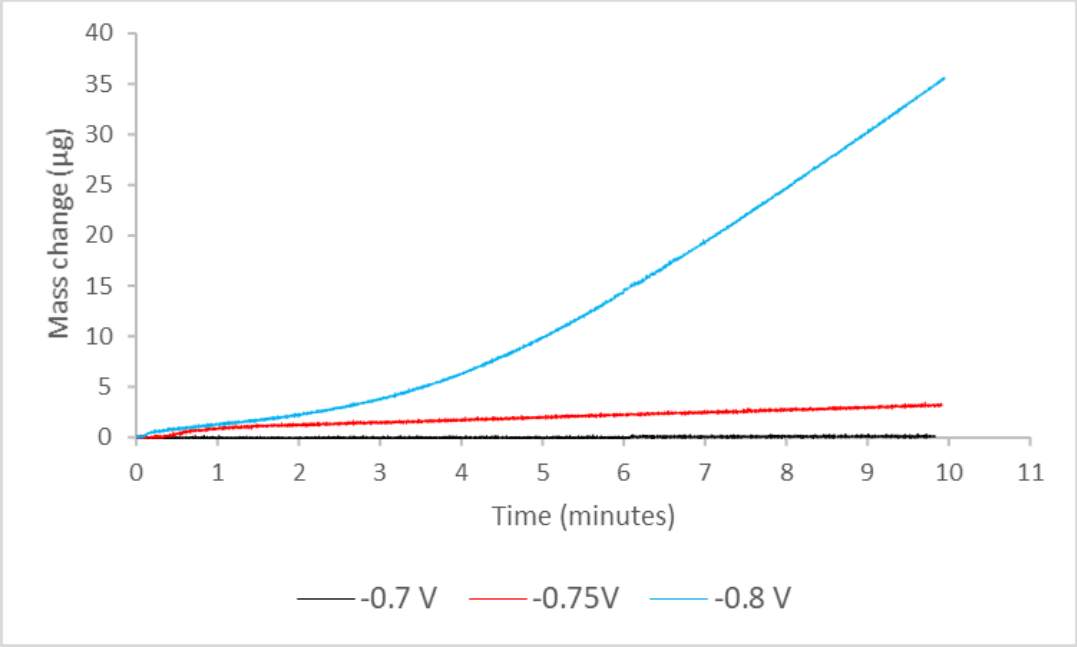

Figure II-4. *Mass change of applied potentials vs. AgCl on Au working electrode in Cowave VMS solution.*

As we can see from Figure II-4, the deposited cobalt's mass change is equal to 0 at -0.7 V, and it starts slightly to increase at -0.75 V but remains quasi-stable at this potential. This implies

that the deposition potential of cobalt on the gold working electrode at -0.8 V is obvious. Moreover, it is following the reaction (Eq. II-5) below:

$$Co^{2+}{}_{(aq)} + 2e^{-} \rightarrow Co_{(s)} \qquad \textit{Eq. II-5}$$

This result also confirms that the shoulder discussed before in Figure II-1 could be attributed to the Co nucleation on the Au working electrode. We suppose that only metallic cobalt is deposited. Then the density of the deposited film is equal to the cobalt density 8.9 g.cm^{-3}, and the deposited cobalt is homogeneous, the thickness is calculated using the Eq. II-6.

$$t = \frac{m}{\rho \times A} \qquad \textit{Eq. II-6}$$

where m is the mass, ρ is the density of cobalt, and A is the area of the gold working electrode.The equivalent thicknesses are represented in Figure II-5.

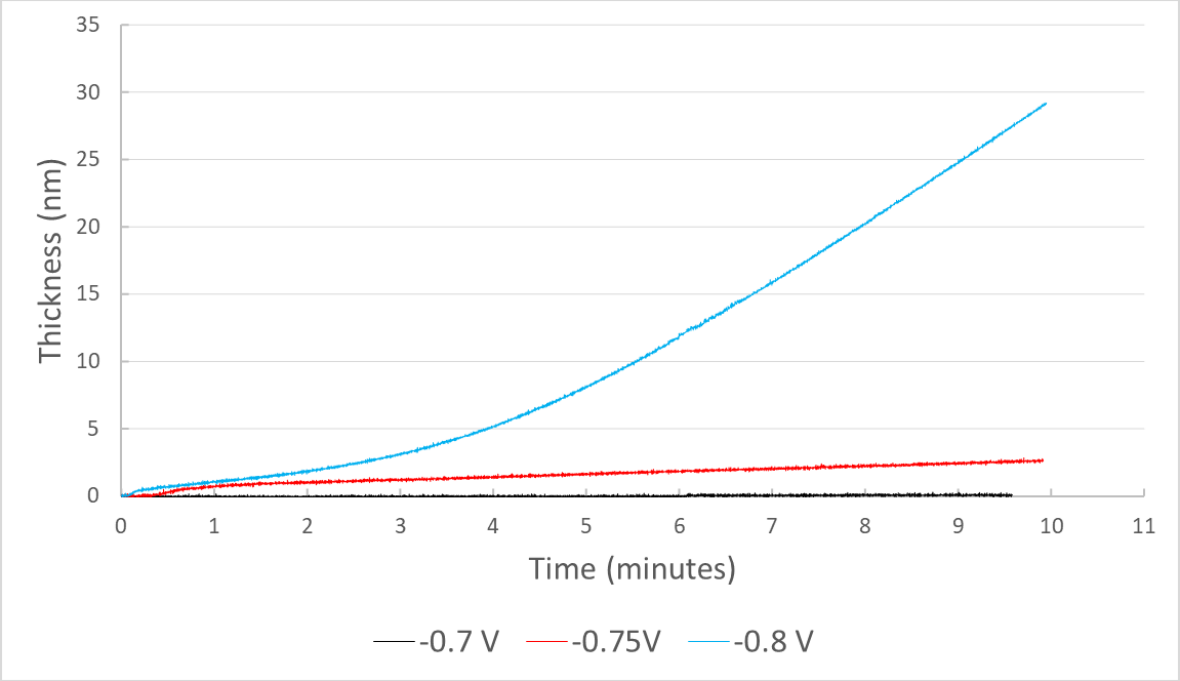

Figure II-5. *Thickness evolution at applied potentials vs AgCl on Au working electrode in Cowave VMS.*

From Figure II-5, considering that the deposited film is uniform, it is clear that EQCM allowed us to make very thin cobalt films (5, 10, 20 nm,…) that can be used as reference objects for reactivity studies in chapter III. The second important result is the high reproducibility of the deposited thicknesses. For the studies performed in this thesis, we hypothesize that the cobalt film thickness is homogeneous. This hypothesis must be confirmed using , energy-dispersive X-ray (EDX) on thin films by studying the ratio Co/Au at different points of the deposit (edge and center).

II.2.2. Cobalt concentration impact

Narayanan *et al.* [11] worked on the hydrogen evolution reaction in the transition of lithium metal. It was showed that transition metal ions concentration impacts the HER. Thus, it is crucial to assess the effect of Co^{2+} concentration on HER.

To analyze the influence of metal ions concentration, two diluted solutions of *Cowave* VMS are prepared. The first solution is a 50% diluted *Cowave* VMS solution. The second, consisting of the dilution of *Cowave* VMS by 75%. The pH was adjusted to 2.2 using HCl. The obtained solutions are shown in Table II-1.

Table II-1. Diluted solutions

Solution	Concentration of $CoCl_2$ (mol/l)
Cowave VMS	0.04
50% dilution	0.02
75% dilution	0.01

The impact of concentration was examined with the method of cyclic voltammetry coupled to EQCM. The tests were conducted in acidic solutions of pH = 2.2, applying different concentrations of electrolyte. Voltammetric tests employed a polycrystalline gold electrode of 1.37 cm² area. In the voltammetric tests, the reference electrode was AgCl. And the counter electrode was a platinum sheet of 3 cm². Voltammetric curves with a scan rate of 20 $mV.s^{-1}$ are illustrated in Figure II-6. it was observed that with reducing cobalt ions concentration (red and blue curve), the limiting current density intensity decreased. This phenomenon is governed by mass-transfer law according to Eq. II-7 [12]:

$$I = nFAk_DC \qquad \textit{Eq. II-7}$$

Where n is the number of electrons involved in the transfer. C represents the bulk concentration of the electrochemically active species. A is the area of the electrode, and k_D is a diffusion constant.

In the negative overvoltage of Figure II-6, two statements are set. The first domain is in the proton reduction region, where it is noticed that in 0.02 and 0.01 M Co^{2+} solutions, only a low overvoltage is necessary to start the proton reduction reaction (see inset graph). While the 0.04 M Co^{2+} solution, the proton reduction starts at a more negative overvoltage (-0.55 V). It can be assumed that increasing cobalt concentration influences proton reduction. The second observation concerns the limiting current of proton reduction. As noticed, the current intensity of proton reduction increases when the electrolyte concentration decrease. This phenomenon

can be related to the fact that Co^{2+} and H^{+} reductions overvoltages are close; thus, there is a possible competition between the two reductions.

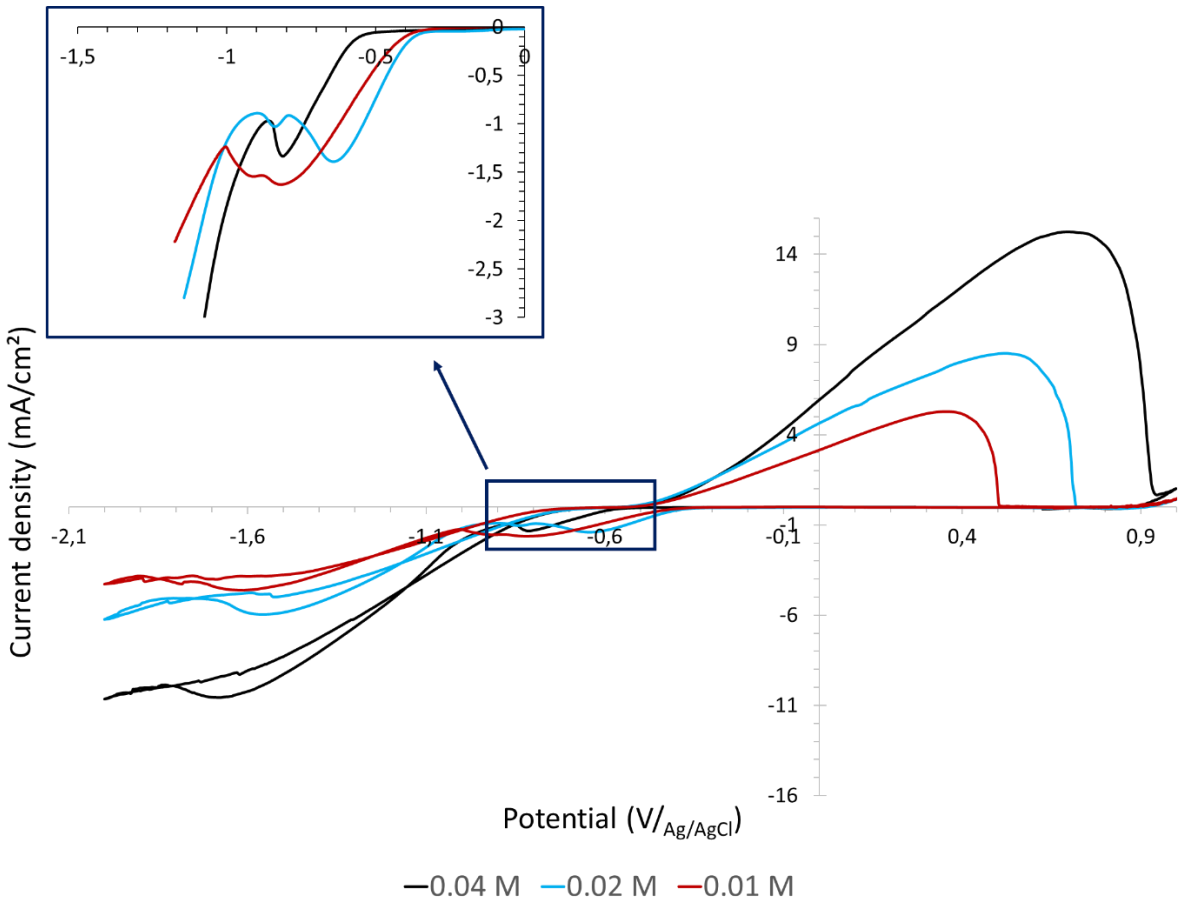

Figure II-6. *Cyclic voltammogram of Au electrode in Cowave VMS 0.04 M (black), 0.02 M (blue), 0.01 M (red), at a scan rate of 20 mV.s^{-1}*

In the more negative potentials (see Figure II-6), the cobalt limiting current density in *Cowave* VMS solution (0.04 M – black curve) is -10.5 mA.cm$^{-2,}$ which decreases with decreasing Co^{2+} to become -5.9 mA/cm² (blue) and -4.6 mA.cm^{-2} (red) in diluted solutions 0.02 M and 0.01 M, respectively. After calculating the ratios of anodic charges and limiting current densities compared to *Cowave* VMS (see Table II-2. Anodic charges and current densities ratios of diluted solutions vs. Cowave VMS solution. It is noticed that the ratios of anodic charges/ *Cowave* VMS fit perfectly with the respect of the ratio Co^{2+} concentrations/ *Cowave* VMS ratios. By making the hypothesis that anodic charge is related only to cobalt dissolution, these results indicate that the amount of deposited cobalt is linearly dependent on the concentration of Co^{2+} concentration. We should note that this experiment is performed at 0 RPM which means that we are under natural convection only.

Table II-2. *Anodic charges and current densities ratios of diluted solutions vs. Cowave VMS solution*

Co^{2+} concentration	Ratio Co^{2+} / Cowave VMS	Anodic charge (mA.s)	Co^{2+} limiting current densities ($mA.cm^{-2}$)	Ratio anodic charges / Cowave VMS
0.04 M	**1**	824.4	10.5	**1**
0.02 M	**0.5**	412.1	5.9	**0.50**
0.01 M	**0.25**	213.5	4.6	**0.26**

A linear trendline of the limiting current density as a function of the concentrationn of cobalt species (see Figure II-7). As shown, the curve's linearity is apparent. Thus, the current limiting peaks depend on the cobalt concentration. The second important point is that this curve does not pass through zero, which means that during cobalt deposition, there are parasitic reactions, and the faradic yield will never be equal to 100%. From the curve of Figure II-7, the extrapolation at 0 is equal to 2.3 mA/cm² and this current is related to the parasitic reaction. To investigate precisely the concentration impact, it would be recommendable to work with a rotating electrode, in order to work under forced convection conditions. In the second place, it would be advisable to work on several lower concentrations to conclude about this phenomenon.

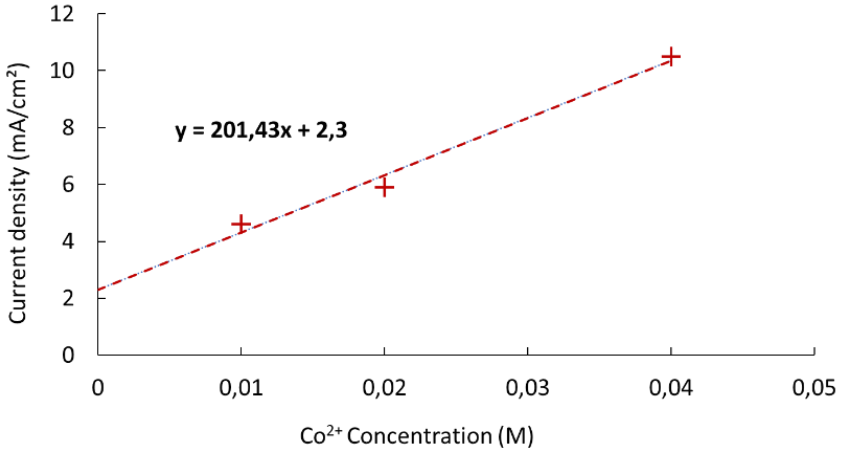

Figure II-7. *Current limiting of Co2+ vs cobalt concentration for Cyclic voltammogram of Au electrode in Cowave VMS 0.04 M (black), 0.02 M (blue), 0.01 M (red), at a scan rate of 20 mV.s-1*

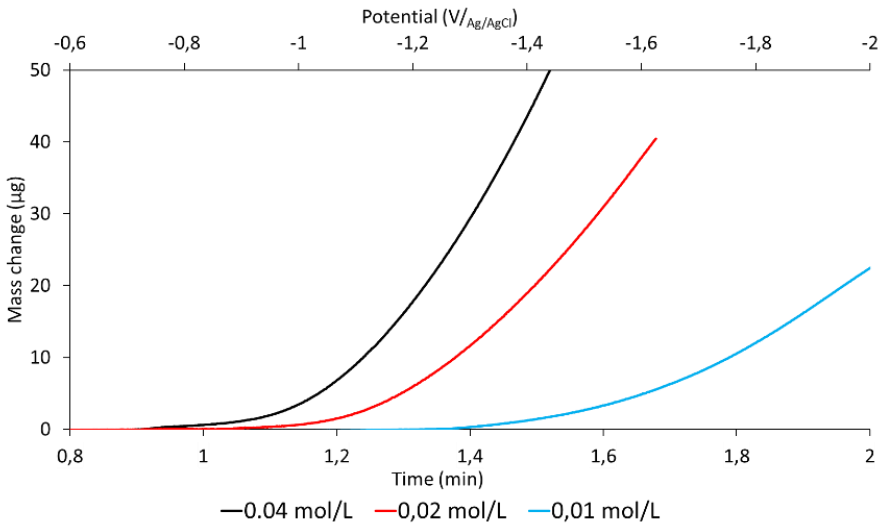

Figure II-8. *Cobalt mass evolution vs time and associated potential on gold electrode in Cowave VMS 0.04 M (black), 0.02 M (blue), 0.01 M (red), scan rate = 20 mV.s^{-1}*

In the anodic region of the Figure II-86, the dissolution peak intensity is decreasing when solutions are diluted. To get more details, EQCM was used during the above experiments. Figure II-8 shows the cobalt mass evolution as a function of time. It was clear that cobalt deposition in 0.04 M solution starts before the 0.02 and 0.01 M solutions. The deposition rate also is affected by dilution. The deposition rate slope decreases by reducing metal ions in the electrolyte (see Figure II-8).

Voltammetric studies, coupled with EQCM on diluted cobalt solutions, showed several new findings. First, increasing Co ions concentration influences the HER reaction by increasing its overvoltage. Second, the cobalt deposition is delayed in diluted solutions. Third, the mass deposition rate is faster in more concentrated cobalt electrolytes.

The observed phenomenon might be due to the competition of H^+ reduction and Co^{2+} reduction [13]. Thus, the concentration of cobalt is a key parameter in acidic media [11].

To clarify this observation, an analysis of the cobalt deposition process was performed in Cowave VMS solution at pH=2.2. Voltammetric tests were conducted at different vertex potentials at a scan rate of 20 mV.s^{-1}. The tests aimed to confirm the different reactions of cobalt deposition and go beyond the cobalt current limiting reaction. The scanning started from the open circuit potential E_{OCP} = -0.4 V/$_{Ag/AgCl}$. Then it moved towards potentials of -0.8 to -2.2 V/$_{Ag/AgCl}$. Next, the direction of scanning was changed, and it continued till the potential of 0.8 V/$_{Ag/AgCl}$ to dissolve the deposited film.

A collective diagram presenting a group of voltammograms obtained following the described outline is illustrated in Figure II-9. During the change of potential towards more electronegative, a slight increase of cathodic current density could be noticed from potential -0.5 V. This increase is may be assigned to the parasitic reactions discussed before.

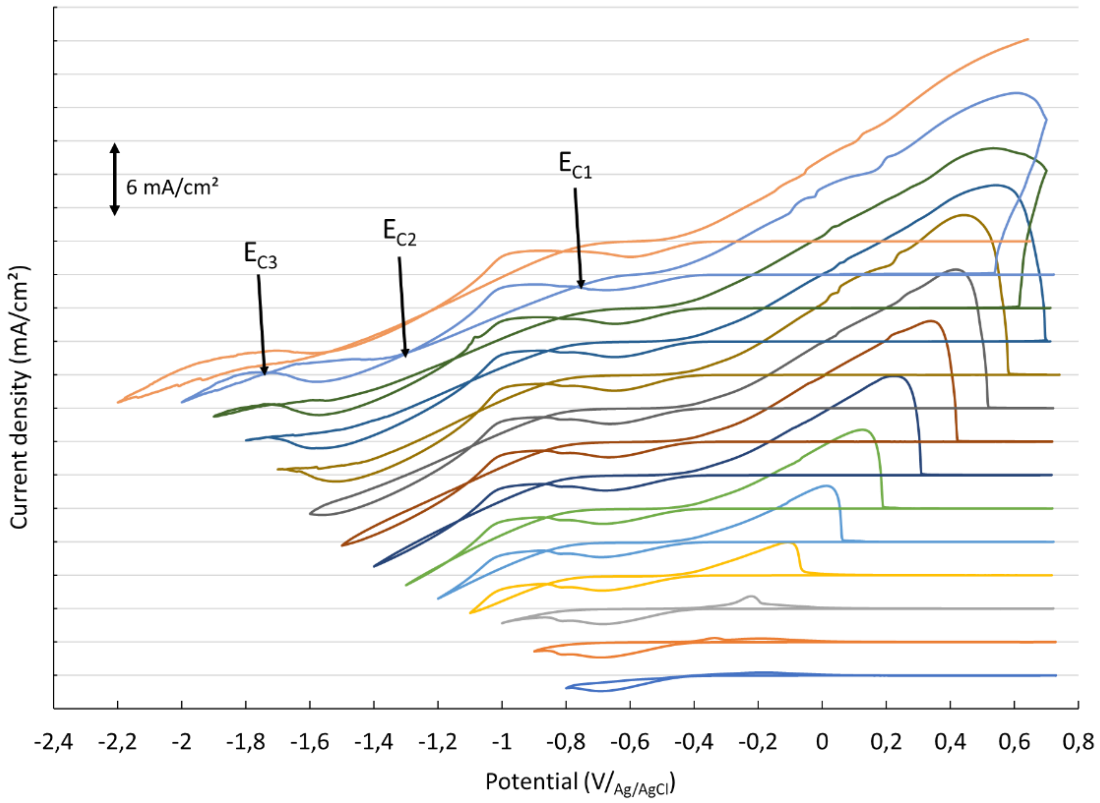

Figure II-9. *Cyclic voltammograms on Au electrode at different vertex potentials at a sweep rate of 20 mV.s^{-1} in Cowave VMS electrolyte solution.*

After reaching -0.8 V (after the apparition of the shoulder), an anodic peak is obtained when the potential is reversed. This peak is assigned to the dissolution of cobalt. The intensity of this peak continues to increase as the vertex potential goes more negative. At -1.65 V, a peak is observed. In the previous study, we showed that this peak is associated with the electrolyte Co^{2+} concentration. Meaning that this peak is the current density diffusion limit of the system. For the potential's vertex more negative than -1.7 V, the cathodic current continues to increase. This increase could be associated with H_2O reduction reaction [14]. Three crossovers E_{C1}, E_{C2}, and E_{C3} were observed at around -0.85 V, -1.1 V, and -1.8 V, respectively. E_{C1} is related to interface changing from Au to H_2/Au. The second crossover E_{C2} is typical of the formation of a new phase involving a nucleation process [14], [15]. The interface at -1.1 V is a mix of H_2 and Co on Au substrate. At the third crossover E_{C3}, it is assumed that H_2O reduction implies the formation of H_2 and HO^- following the reaction (Eq. II-8) below:

$$H_2O_{(l)} + 2e^- \rightarrow H_{2\,(g)} + OH^-_{(aq)} \qquad \textit{Eq. II-8}$$

We suppose that E_{C3} can be associated with the interface changing from H_2/Co to H_2 + OH^-/Co.

For more negative potentials than E_{C3}, OH^- ions are formed at the interface. However, it can imply a local pH increase at the interface.

As we can see in Figure II-9., the drop of the anodic peak depends on vertex potential. This proves that the dissolution region is dependent on the deposition region. When the vertex potential is -2.4 V, there is no anodic peak drop. This is explained by the fact that the cobalt deposited amount is high and the scan rate is higher to dissolve all deposited cobalt. The same experiment is performed with 10 mV/s dissolution scan rate, and effectively the anodic peak drop is noticed.

To confirm the anodic and cathodic regions' dependence, Table II-3 represents each region's charge for different applied potentials -: 0.9, -1.0, -1.1, -1.5, -1.8, -1.9 and -2.0 V.

Table II-3. *Cathodic and anodic charges as a function of vertex potential*

Applied potential vs AgCl	Cathodic charge (mA.s)	Anodic charge (mA.s)
-0.9	36.9	6.3
-1.0	49.7	10.0
-1.1	93.7	41.2
-1.5	455.0	322.8
-1.8	810.6	584.0
-1.9	953.9	691.1

-2.0	1142.6	809.5

The table confirms both regions' dependency, which leads us to hypothesize that the anodic peak is related only to the cobalt dissolution, which means no chemical reactions in the anodic region and only electrochemical dissolution of cobalt.

As the working electrode's nature has an essential role in electroplating, voltammetric studies are performed on cobalt working electrode to compare them to the gold working electrode results. The technique consists of:

- Starting from a gold working electrode, we deposit cobalt in Cowave VMS by chronoamperometry at -1.2 $V_{Ag/AgCl}$ for 2 minutes. The obtained film is considered as a cobalt working electrode, and it will serve as a reference.
- Apply voltammetry cycling on the deposited cobalt starting from -0.3 V to -0.9 V in Cowave VMS for 18 cycles to investigate parasitic reaction behavior on a Co working electrode.
- Finally, dissolve the deposited cobalt.

The applied technique is illustrated in Figure II-10, and the results are presented in Figure II-11.

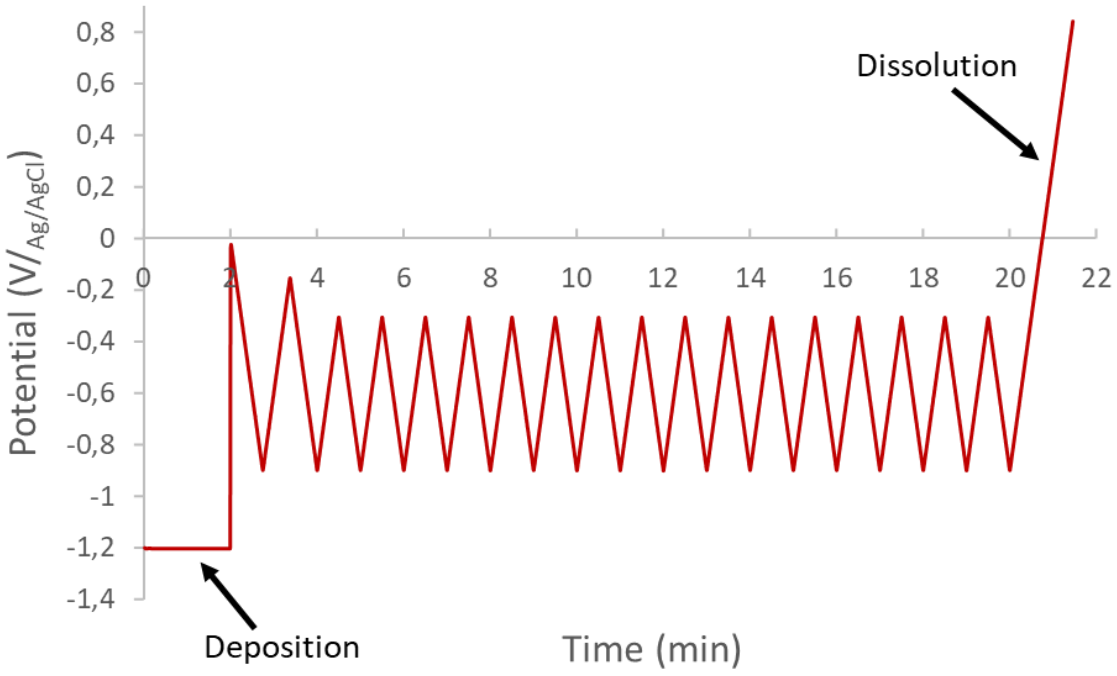

Figure II-10. *The applied process to study the reactions on Co working electrode.*

Figure II-11 shows that there are three regions, the first from 0-2 min, which is associated with the deposition of cobalt. The second region is situated between 2 and 20 minutes. This region is the result of cycling in the parasitic reactions. The third region is the dissolution of the cobalt to return to the initial state on a gold working electrode. The current density of parasitic reactions increases with the number of cycling. During the 1st cycle, the current density is -0.16 mA.cm^{-2}. This value continues to increase to reach -0.85 mA.cm^{-2} in the 18th cycle. These values are relatively low compared to the voltammogram performed directly on Au working electrode (-0.95 mA.cm^{-2}). To understand this phenomenon, mass change is tracked during the applied electrochemical process.

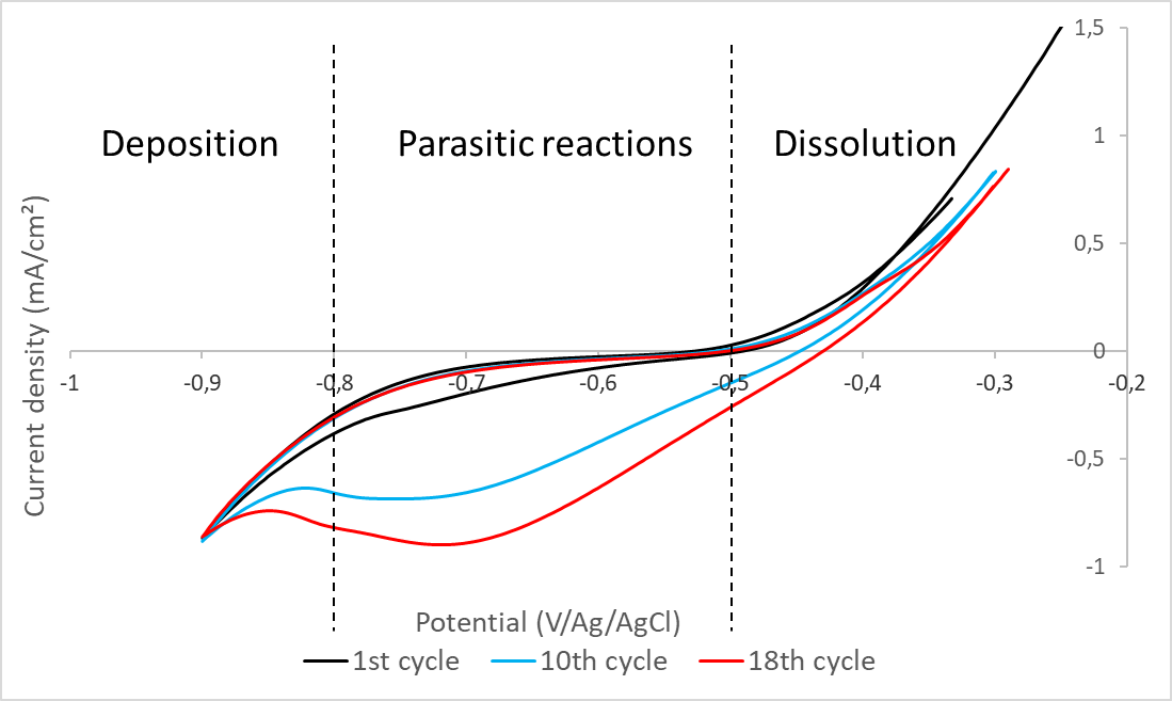

Figure II-11. *Cyclic voltammetry on deposited cobalt in Cowave VMS; scan rate 20 mV.s-1 : 1st cycle (black), 10th cycle (blue) and 18th cycle (red).*

Figure II-12 shows the mass evolution of the three regions discussed before. It can be observed that the mass increases during the first 2 minutes due to the deposition of cobalt to reach~90 µg, which is equivalent to ~75 nm. After 2 min, the voltammetric cycling process begins, and the mass start to decrease. This decrease is the result of cobalt dissolution as the potential is more positive than -0.5 V. As we can see in one cycle, the cobalt is deposited with a small amount compared to the dissolved mass of cobalt. Thus, the mass change is dropping due to the higher dissolution amount compared to the deposited cobalt during cycling. This leads to reducing the thickness of the deposited cobalt. Therefore, it is getting closer and closer to the gold electrode. Thus, the current increases with the number of cycles. It can be concluded

that the parasitic reactions currents depend hugely on the working electrode. The hypothesis that we can make is that the reactivity of the parasitic reactions on gold is higher than the reactivity on cobalt.

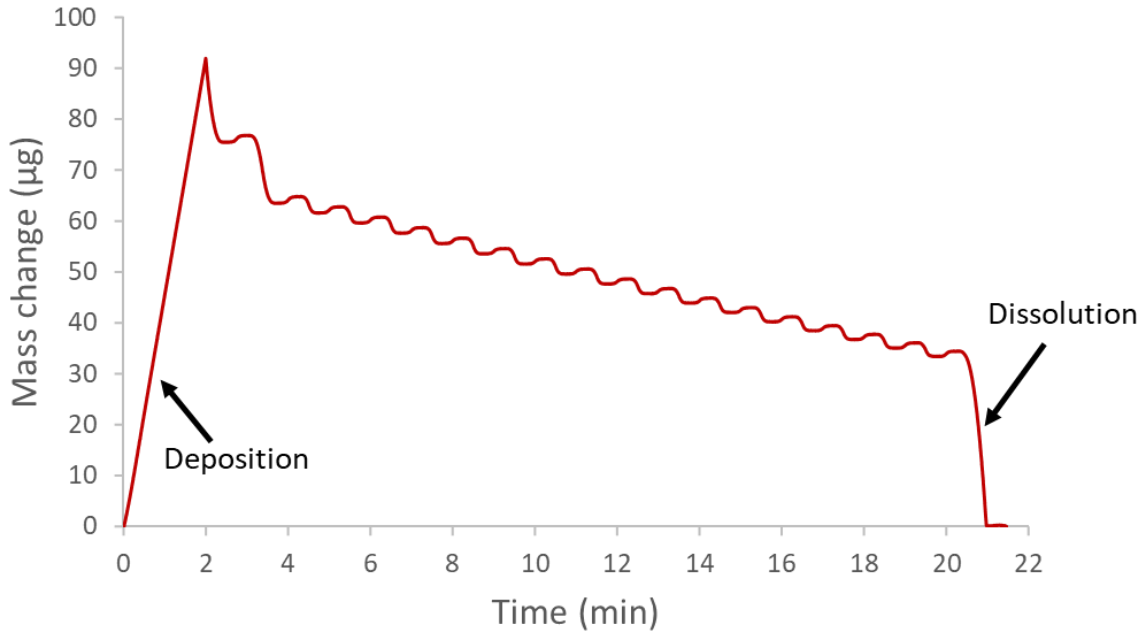

Figure II-12. *Corresponding mass change on cobalt working electrode in Cowave VMS, scan rate 20 mV.*

The second important area in our study concerns the deposition of cobalt. To investigate this part, a voltammogram is obtained in *Cowave* solution using a gold working electrode with a scan rate of 20 $mV.s^{-1}$. The experiment consists of applying 2-cycle linear sweep voltammetry. The first cycle ranges from 0.7 V to -1.7 $V_{/Ag/AgCl}$. At -1.7 V the potential is reversed to reach -0.5 V. From that point, the second cycle is started by applying a direct negative scan to reach -1.7 V. Finally, a potential stripping process is applied towards 0.8 V with a scan rate of 10 $mV.s^{-1}$ to dissolve the deposited cobalt. The technique described below is illustrated in Figure II-13.

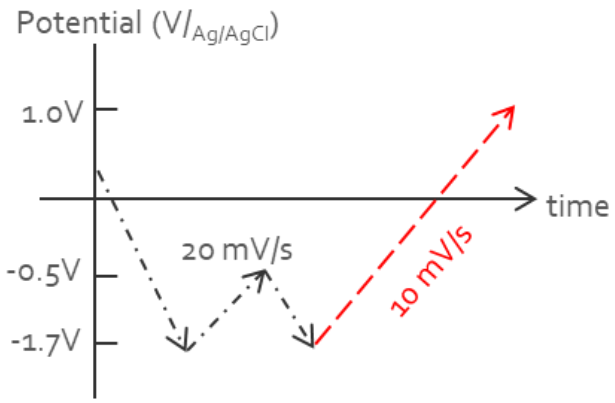

Figure II-13. *Applied process to investigate cobalt deposition on Au vs Co substrate.*

The technique described above was coupled with EQCM to track the mass change. From Figure II-14, it is assumed that except the part of parasitic reactions, all the negative overvoltage region is the same at 1st cycle (on Au) and 2nd cycle (on Co). This means that the cobalt mechanism on a cobalt substrate is the same as on a gold one. The mass change starts to increase (see Figure II-15) at approximately -0.92 V in the 1st cycle (on gold), whereas the mass increases at -0.84 V during the 2nd cycle (on cobalt). It can be assumed that the slight potential difference is related to the behavior of protons on the different electrode surfaces.

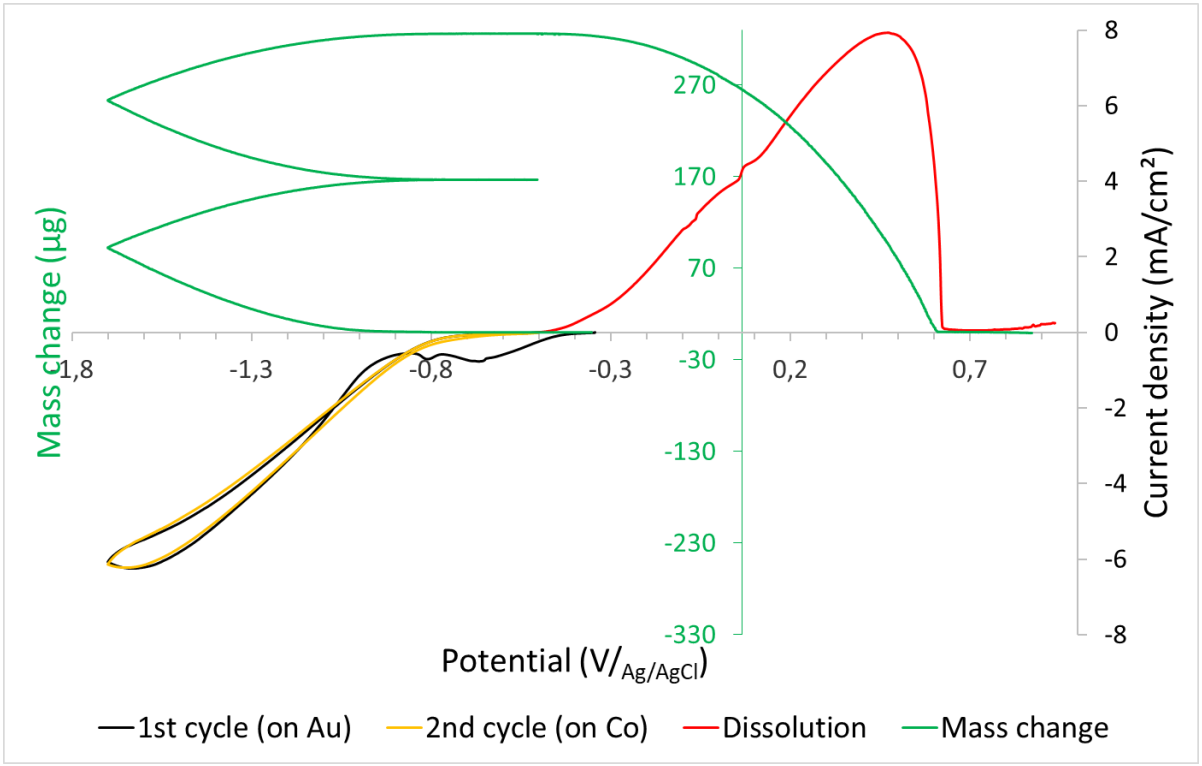

Figure II-14. *cyclic voltammogram in Cowave VMS on: gold in the 1st cycle (black), on cobalt in the 2nd cycle.*

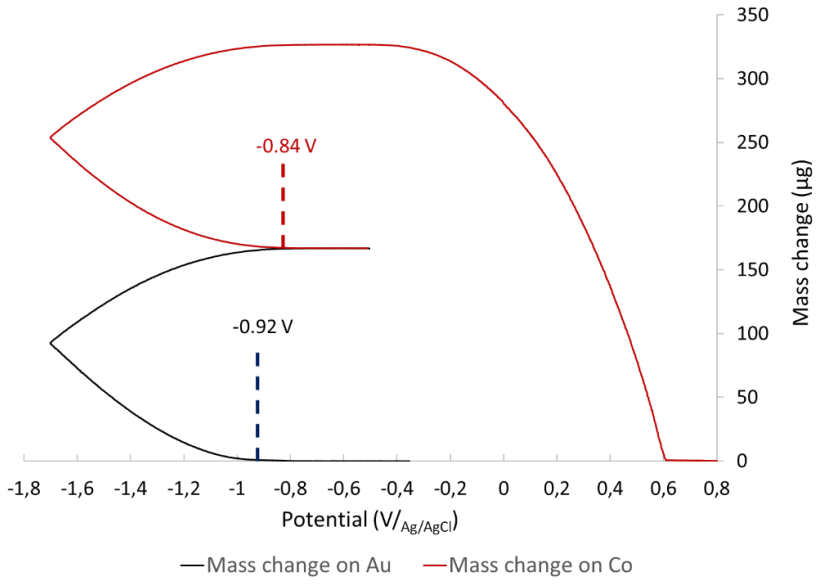

Figure II-15. *Zoomed area of mass change in Cowave VMS: on gold working electrode vs cobalt working electrode.*

II.3 Cobalt electrodeposition mechanism

II.3.1. Current efficiency

During cobalt electrodeposition, we noticed a release of hydrogen gas at the gold working electrode. The phenomenon is persisting before and after reaching cobalt deposition potential in the negative overvoltage region. These hydrogen bubbles become denser after reaching the Co^{2+} limiting current, according to the works presented by J. Wu [16] and J.T. Matsushima [17], this phenomenon is governed by proton reduction before reaching cobalt limiting current, and by H_2O reduction in acidic media after reaching Co^{2+} limiting current. Figure II-16 shows the H_2 bubbles formed during Co electrodeposition process.

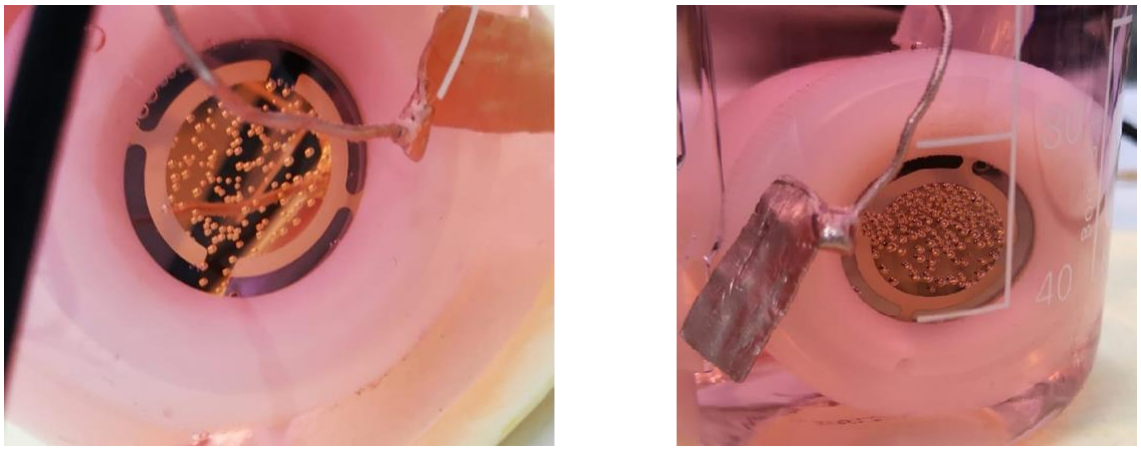

Figure II-16. *hydrogen evolution on gold substrate (left) and on deposited cobalt (right).*

To quantify the impact of hydrogen evolution reaction on cobalt electroplating, a current efficiency (CE%) study is performed. First, 100 ml of aqueous solution "*Cowave* VMS" containing 0.04 mol/L cobalt chloride was used as an electrolytic bath for electrodeposition. The cell was purged with argon for 15min. The temperature of the electrolytic bath is 20°C, and the pH is 2.2. Next, cobalt is electrodeposited on a gold working electrode (1.37 cm^2) by applying potentials (chronoamperometry) starting from -0.8 to -2.2 V vs AgCl with 100 mV steps. These potentials are applied for 30 seconds. Based on the obtained current-time curves, the amount of the total charge (Qc) associated with the reduction reactions (cobalt deposition and hydrogen evolution) is calculated. After deposition, a sweeping voltammetry process is applied to start from -0.5 V to 1.0$V_{Ag/AgCl}$ with a scan rate of 20 mV/s to dissolve all the deposited cobalt. In this way, we calculated the amount of the charge (Qa) due to the dissolution of cobalt. The charges are calculated using the integral as described in Figure II-17. After charges calculation, the current efficiency of the system is calculated by dividing Qa by Qc.

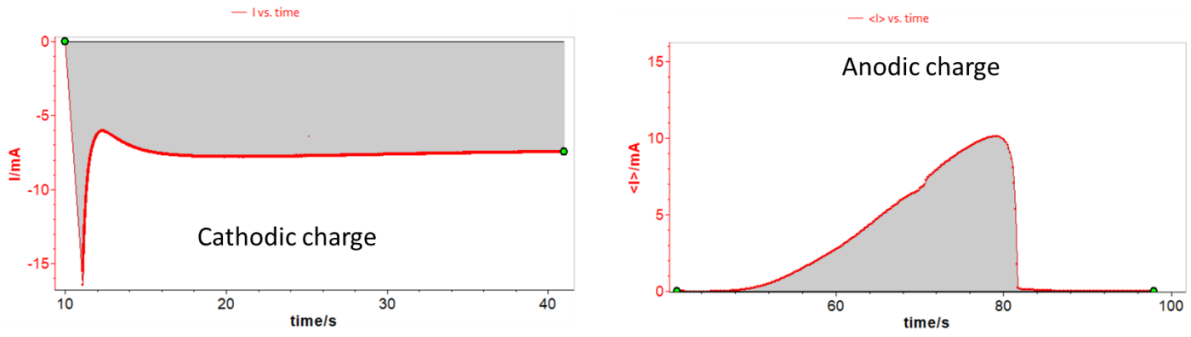

Figure II-17. *The calculation method of cathodic and anodic charge Q_c and Q_a, simultaneously.*

The obtained results are presented in Table II-4.

Table II-4. *cathodic and anodic charge values*

Applied potential ($V_{Ag/AgCl}$)	**|Cathodic charge| (mA.s)**	**|Anodic charge| (mA.s)**	**Current efficiency (%)**
-0.8	42.1	12.7	30.2
-0.9	45.2	15.8	35.0
-1.0	108.3	60.7	56.0
-1.1	163.2	110.1	67.5
-1.2	236.3	162.0	68.6
-1.3	282.7	205.8	72.8

-1.4	338.8	250.3	73.9
-1.5	387.8	288.5	74.4
-1.6	422.0	315.0	74.6
-1.7	441.7	331.0	74.9
-1.8	459.6	340.9	74.2
-1.9	484.0	351.5	72.6
-2.0	521.8	363.1	69.6
-2.1	560.0	380.22	67.9
-2.2	666.0	442.9	66.5

Figure II-18 shows the relationship between the current efficiency of the cobalt deposition reaction and the applied potential (red line). The current efficiency was less than 100% under all tested potentials. These values increased with applied potential until reaching their maximum value of ~75% at -1.7 $V_{/Ag/AgCl}$. Meaning at potentials less cathodic than -1.7 V more percentage of current was contributed to hydrogen reduction rather than cobalt reduction. This phenomenon could be explained by the fact that the reduction of protons H^+ starts before the cobalt ions Co^{2+} reduction (-0.4 $V_{/Ag/AgCl}$ vs -0.8 $V_{/Ag/AgCl}$). For potentials more cathodic than -1.7 $V_{/Ag/AgCl}$, CE% start decreasing to reach 65% at -2.4V. At these potentials, Co^{2+} limit diffusion current is attained, and the H_2O reduction reaction starts (see Eq. II-9):

$$2H_2O_{(l)} + 2e^- \rightarrow H_{2\,(g)} + 2OH^-_{(aq)} \qquad \textit{Eq. II-9}$$

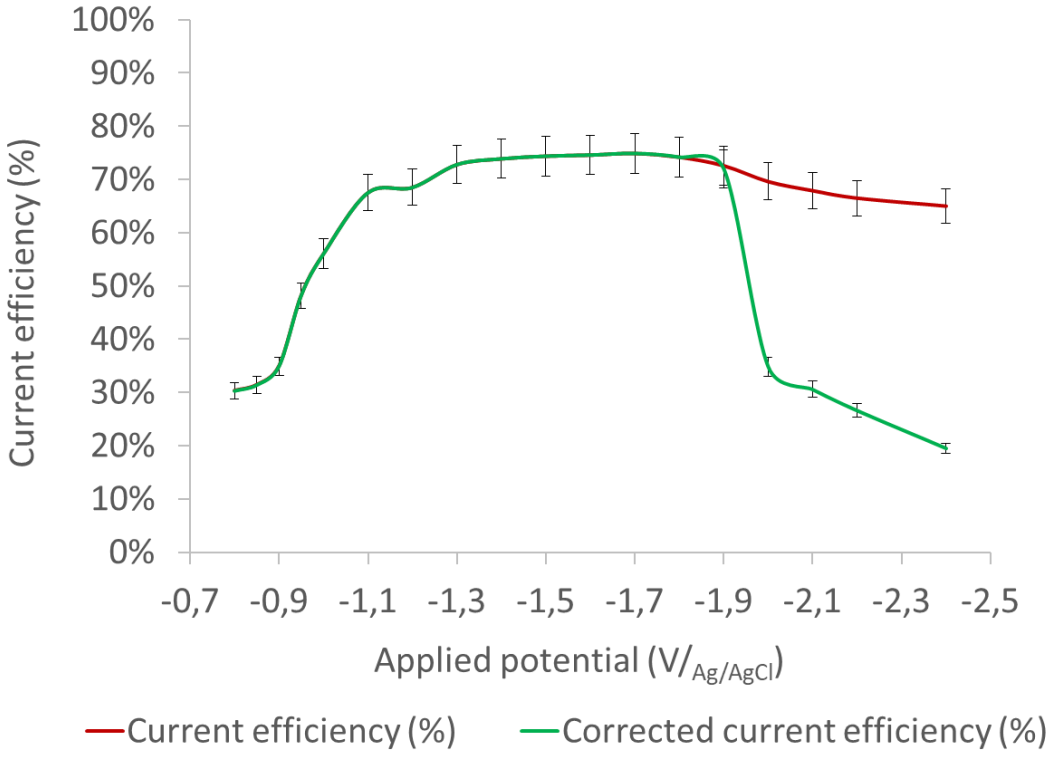

Figure II-18. *Impact of applied potentials on current efficiency of cobalt reduction*

The water reduction will increase H_2 release. Therefore, current efficiency is decreasing after Co^{2+} limits diffusion current. We have noticed that when more negative potentials than -2.0 $V_{Ag/AgCl}$ are applied, the working electrode area is reduced by H_2 bubbles (see Figure II-19). Consequently, the electrochemically active area of the working electrode is also reduced, and it will behave as an insulator. Thus, not all the current is collected at the working electrode. Hence, a corrected CE% is calculated by estimating the new active area Figure II-18 (green line).

Based on Figure II-19 the active area at -2.4 V is estimated at 30% of the working electrode surface. The CE% corrections applied for potentials -2.0, -2.1, -2.2, and -2.4 V are 50%, 45%, 40%, and 30%, respectively. It is very interesting to quantify the quantity of hydrogen and its impact on the cobalt film by investigating the contact angle of hydrogen on cobalt metal.

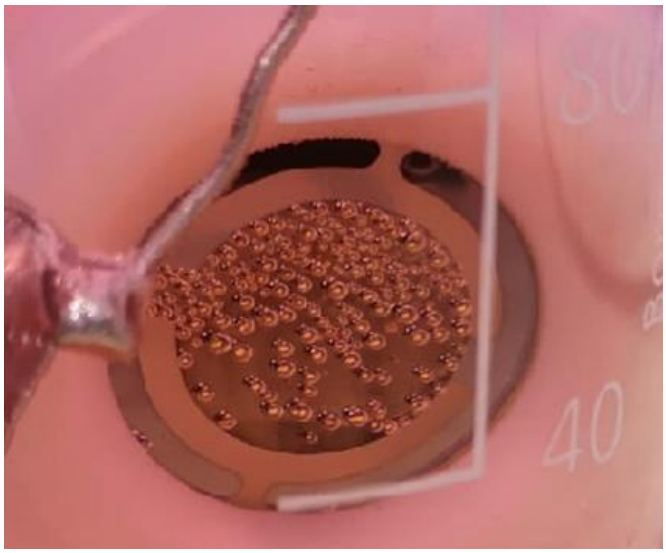

Figure II-19. *Hydrogen evolution reaction at -2.4 V/$_{Ag/AgCl}$ in Cowave VMS solution.*

II.3.2. Nucleation and growth

Chronoamperometry is an effective method to study the metal nucleation/growth model during the electrocrystallization process [18]. Nucleation control is the most powerful strategy for optimizing electroplating in advanced interconnect features [19]. Figure II-20.a shows the current density-time (j-t) transient curves for measuring the deposition of cobalt on a gold electrode in the Cowave VMS electrolyte. The applied potentials are -1.1 V, -1.2 V, and -1.3 V/$_{Ag/AgCl}$, the corresponding time is 30 s, the temperature is 20 °C, and the pH is 2.2. As discussed above, Co deposition dominates the current from crossover at -1.1 V. Therefore, a range of different potentials between -1.1 V and -1.3 V was selected for the following potentiometric studies on Co nucleation.

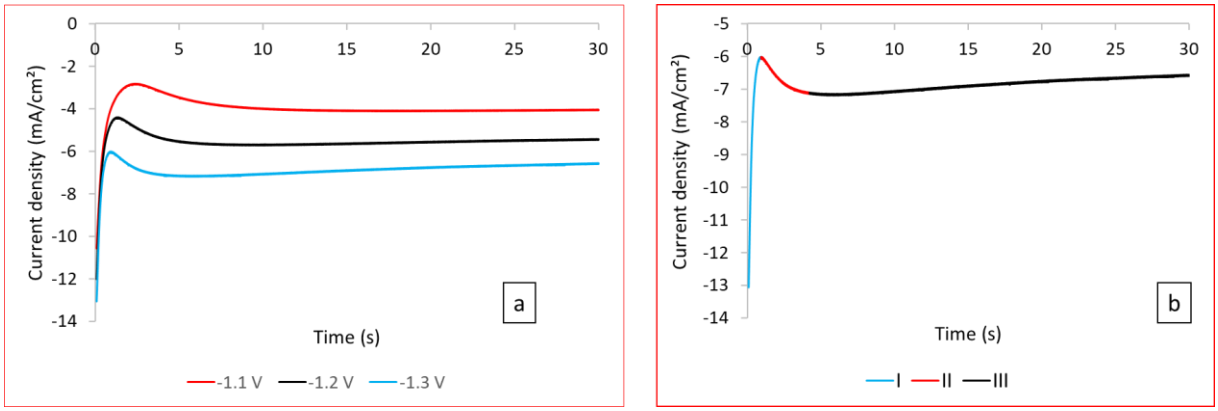

Figure II-20. *j-t curves of cobalt deposition at different step potentials on gold electrode.*

The obtained *j-t* curves can be divided into three parts (see Figure II-20.**b**). The first part (I) is near the vertical axis, and the current density decreases, which corresponds to the charging

of the electric double layer on the electrode surface. In the second part (II), the current density gradually increases and reaches the maximum current density j_m value, which is a typical crystal nucleation/growth process. As the Co^{2+} diffuses from the electrolyte to the electrode/solution interface in the third part (III), the working electrode current density gradually decreases. Since cobalt deposition occurs at a comparably negative potential, hydrogen evolution inevitably occurs. The surface agitation caused by hydrogen bubbling promotes mass transport. The observed steady-state current density includes Co deposition and hydrogen evolution [14]. In the *j-t* curve, it is worth noting that by making the potential more negative, the maximum current density (j_m) gradually increases, while the corresponding time (t_m) decreases, which indicates an increase in the nucleation rate (see Table II-5). This may be because the higher electric field force under more negative potential increases the active nucleation sites on the electrode surface, promoting the electro-crystallization process [18], [20].

Table II-5. *j_m and t_m of j-t curves for cobalt deposited at -1.1, -1.2, and -1.3 V/$_{Ag/AgCl}$.*

Potential (V vs AgCl)	J_m (mA/cm^2)	t_m (s)
-1.1 V	-4.12	18.79
-1.2 V	-5.73	9.96
-1.3 V	-7.19	5.42

The early stage of the electrochemical phase transition is usually related to the two-dimensional or three-dimensional nucleation process. The rate of the two-dimensional nucleation process and the number of nuclei formed thereby strongly depend on the overpotential. Therefore, it is essential to establish a precise relationship between overpotential and nucleation kinetics.

To characterize the nucleation process of cobalt, the data of the CA curve is normalized to *$(j/j_m)^2$ - (t/t_m)* curve and compared using the Scharifker–Hills model [20] based on equations below:

Progressive nucleation:

$$(j/j_m)^2 = \frac{1.2254}{(t/t_m)} \{1 - exp[-2.3367(t/t_m)^2]\}^2 \qquad \textit{Eq. II-10}$$

Instantaneous nucleation:

$$(j/j_m)^2 = \frac{1.9542}{(t/t_m)}\{1 - exp[-1.2564(t/t_m)]\}^2 \qquad \textit{Eq. II-11}$$

Instantaneous nucleation corresponds to the slow growth of nuclei on a small number of active sites; all activated at the same time. Progressive nucleation corresponds to the fast growth of nuclei on many active sites; all activated during electroreduction [21]. The obtained dimensionless $(j/j_m)^2$ - (t/t_m) curve for each applied potential is shown in Figure II-21.

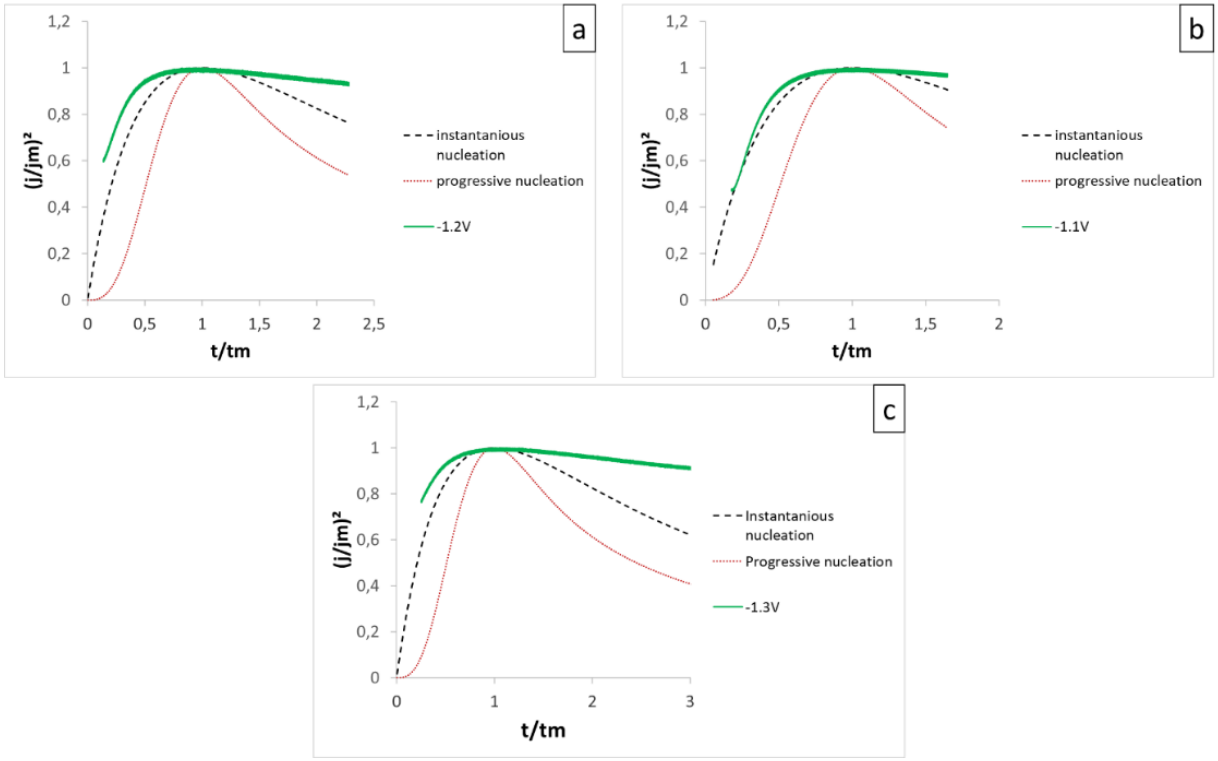

Figure II-21. *Dimensionless curves of the cobalt deposition process on a gold working electrode: (a) -1.1 V; (b) -1.2 V and (c) -1.3 V/$_{Ag/AgCl}$.*

From the dimensionless $(j/j_m)^2$ - (t/t_m) curves at all applied potentials, it can be seen that the nucleation model of Co follows the instantaneous nucleation model discussed before. However, when $t/t_m>1$, the experimental curves gradually deviate from the theoretical curve. This deviation becomes greater when the applied potential increases. On the other hand, as has been observed in the analysis of the current transients, the experimental curves separate from the theoretical ones at longer times, after the maximum t_m (see Figure II-21). This indicates that a change in the growth process occurs during electrodeposition. The transition to a 3D growth may occur, thereby providing an additional activity that adds additional active nucleation sites for the electro-crystallization of cobalt ions [22]–[24].

This study is applied at other potentials -1.4, -1.5, -1.6, -1.7, -1.8, -1.9 V/$_{Ag/AgCl}$. It is noticed that the results do not follow the theoretical curves of nucleation. It is supposed that at

these potentials, the domination of HER on Co is higher. P. Allongue studied the cobalt electrodeposition on gold electrode. It was concluded that at potentials < −1.2 VMSE, Co grows 2D with the initial formation of biatomic islands which rapidly cover the entire Au surface, followed by layer-by-layer growth; at potentials > −1.20 VMSE, Co grows 3D with the formation of large multilayer islands with flat top [25].

II.3.3. Bath temperature impact

We have studied the deposition mechanism of cobalt at room temperature (at 20°C). These studies allowed us to conclude that the current efficiency of cobalt deposition depends on the reduction of protons or HER. During my experiments, I noticed that the current efficiency I was calculating changes from one experience to another. This variation is observed between 2 experiments carried out between morning and afternoon during winter. Knowing that the pH was constant but after checking the bath temperature, the value was 15.7 °C in the morning and 20°C in the afternoon.

To evaluate the bath temperature impact, a voltametric study on Au electrode in HCl at different temperatures was performed. The pH of the solution is kept at 2.2. To vary the bath temperature, a refrigerator and a hairdryer are used to decrease and increase its value simultaneously. The temperature is checked using Eutech pH 150 temperature electrode.

For this study, two bath temperatures are chosen as T_1=12°C and T_2=16°C. At each bath temperature, a cyclic voltammogram is performed on a disc gold working electrode of 0.196 cm². A saturated calomel electrode and a platinum sheet (3 cm²) are used as reference and counter electrode, respectively. The scan rate for this experiment was set to 50 $mV.s^{-1}$. The resulting curves are shown in Figure II-22.

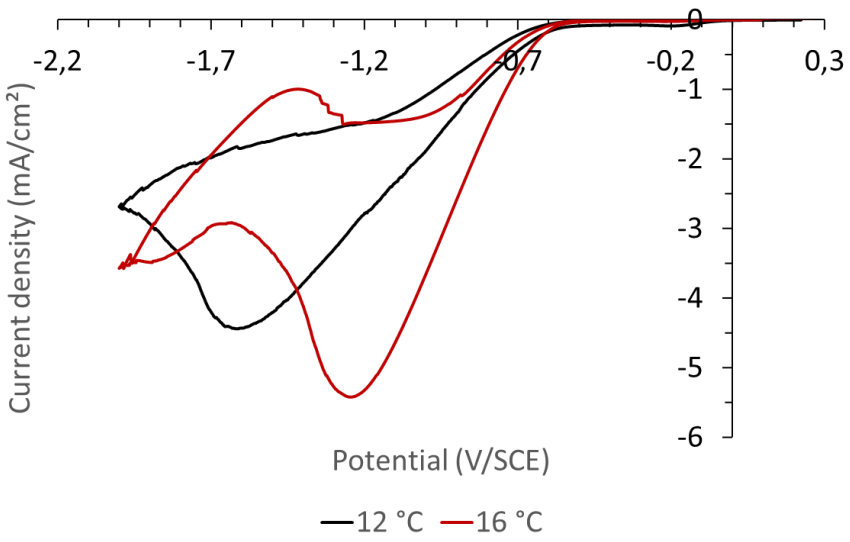

Figure II-22. *Cyclic voltammogram on Au working electrode in HCl at 12°C (black) and 16°C (red) at a scan rate of 50 mV.s^{-1}.*

As shown in the obtain voltammogram (see Figure II-22), current density starts to increase at the same potential at both bath temperatures 12 and 16°C. However, the reduction rate of the protons is faster at 16°C compared to 12°C. At fixed potential, the current displays an obvious increase with cell temperature, confirming that HER at Au electrode is an activated process [26].

To summarize, the cobalt electroplating process on gold may be impacted indirectly by the bath temperature. This impact is explained by the variation of the HER current when the temperature changes. Thus, the current efficiency of Co deposition on Au is affected. Finally, at a fixed potential, the current efficiency of Co is higher at lower temperatures.

II.4 Conclusion

- Voltammetric studies in *Cowave* cobalt chemistry have been performed on gold working electrode using electrochemical quartz crystal microbalance. The main statements are:
  - Cobalt deposition on a gold electrode process is a complicated mechanism due to several parasitic reactions.
  - The potential of cobalt deposition on gold is approximately -0.8 $V_{/Ag/AgCl}$.
  - Cobalt deposition occurs simultaneously with the hydrogen evolution reaction (HER).
  - Hydrogen evolution reaction impacts the cobalt deposition by reducing its current efficiency (CE%). The higher CE% recorded is 73%.
  - A second parasitic reaction is H_2O reduction. This reaction takes place at high negative overpotentials. H_2O reduction may form hydroxides at the cathode/electrolyte interface.
  - EQCM shows that cobalt and proton reduction are in competition during all the process.
  - The mechanism reactions proposed are:

$$2H^+_{(aq)} + 2e^- \rightarrow H_{2\,(g)}$$

$$Co^{2+}_{(aq)} + 2e^- \rightarrow Co_{(s)}$$

$$2H_2O_{(l)} + 2e^- \rightarrow H_{2\,(g)} + 2OH^-_{(aq)}$$

- Cobalt nucleation is investigated by applying the Scharifker–Hills model resulted in the following findings:
  - Cobalt nucleation is instantaneous at -1.1, -1.2, and -1.3 $V_{/Ag/AgCl}$.
  - The experimental curves of nucleation do not follow the theoretical curves for the other potentials due to HER competition with cobalt deposition.
- The impact of cobalt ions concentration is studied using electrochemical quartz crystal microbalance. The main results are:
  - Increasing cobalt concentration suppresses the HER reaction by increasing its overvoltage.
  - The cobalt deposition is delayed in diluted solutions.
  - The mass deposition rate is faster in more concentrated cobalt electrolyte.

- Electroplating bath temperatures are examined by studying the impact of T° on proton reduction. The new findings are:
  - The cobalt electroplating process on gold may be impacted indirectly by the bath temperature. This impact is explained by the variation of the HER current when the temperature changes.
  - The current efficiency of Co deposition on Au is affected by bath temperature.
  - The lower the bath temperature, the higher the current efficiency.
- The following statements are set after an investigation of the additive impact on cobalt deposition:
  - EQCM confirms that the additive added in Cowave chemistry suppresses the cobalt deposition.
  - It would be interesting to further develop this study by investigating the impact of the additive on nucleation and growth.
- The annealing effect on cobalt film composition is inspected by XPS, the outcomes are:
  - Annealing reduces oxygen amount in the deposited cobalt film.
  - Annealing improves the cobalt film by decreasing its electrical resistivity.
- Cobalt film reactivity in acidic and alkaline solutions is investigated in different conditions (O_2 saturated and de-aerated bath). Using EQCM and XPS, it was found that:
  - Cobalt is dissolved in acidic solutions due to dissolved oxygen presence.
  - The dissolution rate in acidic media is considerable (from 0.5 to 3.2 nm/min)
  - The immersion of cobalt film in O_2 saturated alkaline buffer (pH=10) results in the formation of hydroxides species. This formed film reaches saturation after 10 minutes of immersion. However, the cobalt mass remains unchanged in the alkaline de-aerated solution.
  - XPS depth profiling confirms the Co hydroxides formation after immersion in alkaline O_2 saturated solution.

II.5 References

[1] A. L. Rominiyi, M. B. Shongwe, and B. J. Babalola, “Development and characterization of nanocrystalline cobalt powder prepared via high energy ball milling process,” *IOP Conf. Ser. Mater. Sci. Eng.*, vol. 430, p. 012029, Oct. 2018, doi: 10.1088/1757-899X/430/1/012029.

[2] M. Li and J. Lu, “Cobalt in lithium-ion batteries,” *Science*, vol. 367, no. 6481, pp. 979–980, Feb. 2020, doi: 10.1126/science.aba9168.

[3] Schlesinger M, Paunovic M. Modern electroplating. John Wiley & Sons; 2011

[4] A. Vicenzo and P. L. Cavallotti, “Growth modes of electrodeposited cobalt,” *Electrochimica Acta*, vol. 49, no. 24, pp. 4079–4089, Sep. 2004, doi: 10.1016/j.electacta.2004.04.001.

[5] L. Caillard, J. Vigneron, M. Thiam, A. Lakhdari, F. Raynal, and A. Etcheberry, “Investigation of Cu/TaN and Co/TaN Barrier-Seed Oxidation by Acidic and Alkaline Copper Electroplating Chemistry for Damascene Applications,” *J. Electrochem. Soc.*, vol. 165, no. 10, pp. D439–D443, 2018, doi: 10.1149/2.0761810jes.

[6] A. Etcheberry *et al.*, “X-Ray Photoelectron Spectroscopy Estimation of Cobalt Seed Layer Reactivity Toward Air Exposure: A Challenge?,” *ECS Trans.*, vol. 97, no. 1, pp. 149–156, May 2020, doi: 10.1149/09701.0149ecst.

[7] V. Mevellec, D. Suhr, and L. RELIGIEUX, “Electrolyte and method for electrodepositing copper onto a barrier layer,” WO2014044942A1, Mar. 27, 2014.

[8] M. A. Rigsby, T. A. Spurlin, and J. D. Reid, “The Multi-Functional Role of Boric Acid in Cobalt Electrodeposition and Superfill,” *J. Electrochem. Soc.*, vol. 167, no. 11, p. 112507, Jul. 2020, doi: 10.1149/1945-7111/aba640.

[9] E. Gileadi and V. Tsionsky, “Studies of Electroplating Using an EQCM. I. Copper and Silver on Gold,” *J. Electrochem. Soc.*, vol. 147, no. 2, p. 567, 2000, doi: 10.1149/1.1393234.

[10] I. Flis-Kabulska, “Electrodeposition of cobalt on gold during voltammetric cycling,” p. 8.

[11] A. Guha, N. M. Kaley, J. Mondal, and T. N. Narayanan, “Engineering the hydrogen evolution reaction of transition metals: effect of Li ions,” *J. Mater. Chem. A*, vol. 8, no. 31, pp. 15795–15808, Aug. 2020, doi: 10.1039/C9TA12926J.

[12] A. J. Bard and L. R. Faulkner, *Electrochemical methods: fundamentals and applications*, 2nd ed. New York: Wiley, 2001.

[13] Z. Liang Bao and K. L. Kavanagh, “Aligned Co nanodiscs by electrodeposition on GaAs,” *J. Cryst. Growth*, vol. 287, no. 2, pp. 514–517, Jan. 2006, doi: 10.1016/j.jcrysgro.2005.11.077.

[14] Y. Hu and Q. Huang, “Effects of Dimethylglyoxime and Cyclohexane Dioxime on the Electrochemical Nucleation and Growth of Cobalt,” *J. Electrochem. Soc.*, vol. 166, no. 1, pp. D3175–D3181, 2019, doi: 10.1149/2.0241901jes.

[15] N. Ramos-Lora, L. H. Mendoza-Huizar, and C. H. Rios Reyes, “COBALT ELECTRODEPOSITION ONTO STAINLESS STEEL 304 FROM AMMONIACAL SOLUTIONS,” *J. Chil. Chem. Soc.*, vol. 56, no. 2, pp. 631–634, 2011, doi: 10.4067/S0717-97072011000200001.

[16] J. Wu, F. Wafula, S. Branagan, H. Suzuki, and J. van Eisden, “Mechanism of Cobalt Bottom-Up Filling for Advanced Node Interconnect Metallization,” *J. Electrochem. Soc.*, vol. 166, no. 1, pp. D3136–D3141, 2019, doi: 10.1149/2.0161901jes.

[17] J. T. Matsushima, F. Trivinho-Strixino, and E. C. Pereira, “Investigation of cobalt deposition using the electrochemical quartz crystal microbalance,” *Electrochimica Acta*, vol. 51, no. 10, pp. 1960–1966, Feb. 2006, doi: 10.1016/j.electacta.2005.07.003.

[18] X. Zhou, Y. Wang, Z. Liang, and H. Jin, “Electrochemical Deposition and Nucleation/Growth Mechanism of Ni–Co–Y2O3 Multiple Coatings,” *Materials*, vol. 11, no. 7, p. 1124, Jul. 2018, doi: 10.3390/ma11071124.
[19] P.-H. Haumesser, Nucleation and growth of metals: from thin films to nanoparticles. London: ISTE Press Ltd ; Elsevier, 2016.

[20] K. Raeissi, A. Saatchi, and M. A. Golozar, “Effect of nucleation mode on the morphology and texture of electrodeposited zinc,” p. 8.

[21] D. Grujicic and B. Pesic, “Electrochemical and AFM study of cobalt nucleation mechanisms on glassy carbon from ammonium sulfate solutions,” *Electrochimica Acta*, vol. 49, no. 26, pp. 4719–4732, Oct. 2004, doi: 10.1016/j.electacta.2004.05.028.

[22] S. Basavanna and Y. Arthoba Naik, “Electrochemical studies of Zn–Ni alloy coatings from acid chloride bath,” *J. Appl. Electrochem.*, vol. 39, no. 10, pp. 1975–1982, Oct. 2009, doi: 10.1007/s10800-009-9907-1.
[23] M. Srivastava, V. K. W. Grips, and K. S. Rajam, “Electrochemical deposition and tribological behaviour of Ni and Ni–Co metal matrix composites with SiC nano-particles,” *Appl. Surf. Sci.*, vol. 253, no. 8, pp. 3814–3824, Feb. 2007, doi: 10.1016/j.apsusc.2006.08.022.
[24] J. Torrent-Burgués and E. Guaus, “Effect of tartaric acid in the electrodeposition of zinc,” *J. Appl. Electrochem.*, vol. 37, no. 5, pp. 643–651, Mar. 2007, doi: 10.1007/s10800-007-9296-2.
[25] N. Di, A. Damian,1, F. Maroun and P. Allongue “Influence of Potential on the Electrodeposition of Co on Au(111) by In Situ STM and Reflectivity Measurements ,” *J. Electrochemical Society*, September 2016. DOI: https://doi.org/10.1149/2.0091612jes.
[26] Z. Tang, L. Liao, Y. Zheng, J. Kang, and Y. Chen, “Temperature Effect on Hydrogen Evolution Reaction at Au Electrode,” *Chin. J. Chem. Phys.*, vol. 25, no. 4, pp. 469–474, Aug. 2012, doi: 10.1088/1674-0068/25/04/469-474.

CHAPTER III Cobalt thin film behavior

CHAPTER III COBALT THIN FILM BEHAVIOR 84

III.1 INTRODUCTION 85

III.2 ANNEALING AND BATH PH IMPACT ON DEPOSITED COBALT FILM 88

III.2.1. Impact of Annealing 89

III.2.2. Impact of bath pH 92

III.3 COBALT FILM REACTIVITY TOWARD AIR-EXPOSURE 94

III.4 COBALT FILM REACTIVITY IN CHEMISTRIES 100

III.4.1. Reactivity vs copper plating chemistries 100

III.4.2. Reactivity vs acidic solutions 107

III.4.3. Reactivity vs alkaline solutions 109

III.5 CONCLUSION 114

III.6 REFERENCES 115

III.1 Introduction

The use of XRay-Photoemission Spectroscopy is the material characterization that has been privileged in this thesis work. There are many reasons for this specific choice. The first is that XPS is a surface analysis that uses photoemission information from the first 10 nanometers of matter with a predominance (over 90% of total intensity) of the contribution from the first three nanometers. This specificity means that this approach can be used for all electrolytic Co deposits, whether 5 nm or several hundred. aveni® for all their Co.

"aveni" already had all the information from XRD on the crystalline quality of its films before and after thermal annealing. So we did not systematically look at the crystal line quality of all of our films that we knew their crystallography. We only have a simple routine check that turned out to be what we expected. These XRD analyzes were supplemented by SEM-EDX morphological and chemical observations. Then we focused on the systematic XPS characterization of all our films or others provide by aveni's collaborations.

Indeed one of the objectives of this thesis was to progress as a priority on the mastery of the physical-chemistry of the surface of Co films, particularly when they are ultra-thin in the form of a seed layer. XPS was therefore the most suitable characterization: for its probe depth, but above all for its ability to quantitatively assess chemical shifts and therefore the different chemical environments at their origins. The nature, the thickness of the oxides, their reactivity vis-a-vis the deposit solutions are all points that are not clearly established for the Cu / Co or Co/Co connections. Only the XPS is able, even as an *ex–situ* technique, to provide the best chemical information on the fate of Co seed layers but also on the recovery of Co deposits.

Morover in this privileged surfacic chemical context an opened question was the effect of the thermal annealing in partial hydrogen atmosphere. Aveni knew that its layers annealing under hydrogen seems to smoothen out the surface and promote a somewhat coarser crystallite size. This increase in grain size will reduce the electrical resistivity of the deposited film, which is a key parameter in the microelectronic industry. J. Kelly et al. [1] worked on the annealing effect on cobalt films. They concluded that annealing reduces impurity in electroplated films. Nevertheless the literature did not provide any quantitative information about the post annealing surface chemistry in interaction with a presumably reductive atmosphere. So in complement of the XRD demonstration of the crystallinity benefits obtained by thermal annealing we decide in this thesis, again by XPS, to provide information about the final chemistry of aveni film after annealing.

Moreover, the physico-chemistry properties of cobalt electrodeposits are greatly affected by the above electrodeposition conditions. One of these conditions' critical parameters is the pH of electrolyte, which plays a significant role in cobalt electrodeposition [2]. By XPS, the impact of three bath pH's is studied to evaluate its impact on cobalt oxides amounts.

In this very challenging context of microelectronic, the control of the Co surface chemistry and particularly its oxidation process are probably the more strategic. Conformal Co seed characteristics (i.e. electronic conductivity), preceding the following filling chemistry, are partially related to Co surface oxide behavior toward the filling step. Its understanding, then its control, will be determinant to obtain a perfect and reliable filling process of aggressive structures.

In this context, it is important to perform as selective as possible experiments which provide controlled and reproducible evolution of XPS responses toward oxidation features on metallic Co. Knowledge of the cobalt oxide response for XPS analysis is rather established nevertheless the kinetic of metallic Cobalt oxidation is poorly investigated. It is particularly true for oxidation processes toward the air interaction. The difficulty is associated to the disposal of an oxide free cobalt to start a quantitative kinetic study of the cobalt oxidation process. This point is very important when we consider the beginning of the via filling stage over a Co seed layer. In this chapter we propose a topic on this matter. To collect quantitative information, it is important to start from reference samples and their following evolutions. So we chose to be able to strat from a pure Co metallic surface which is then exposed to air interaction as reference support for a careful oxidation investigation. So with this objective we developed for this thesis an adapted and novel experimental method as metallic Co is quasi instantaneously oxygen reactive as we will see below, we defined as initial surfaces, a fresh metallic Co surfaces obtained after Argon ion bombardment (sputtering process). Samples are then exposed to air in a dedicated and well adapted chamber with varying exposure time. The evolution of the initial Co metallic XPS response is then monitored versus time exposure to provide quantitative as possible information about the trends and the kinetic of the oxidation of the Co surfaces.

As several metals can be deposited on the cobalt seed layer, copper is generally used in the damascene process. The integrity of the cobalt seed layer before and during electrodeposition is a key parameter to achieve defect-free metal with a high-quality interface. To fill vias and trenches with copper, electrodeposition is typically performed using acidic chemistry (pH<2)

that uses a combination of additives to serve specific purposes in the metallization process [3]–[5].

With this aspect in mind, a new, innovative chemistry has been developed by aveni® to achieve void-free filling of aggressive structures while preserving the interface quality between each metal stack layer [6]–[8]. This chemistry is alkaline and relies on organometallic complexes (copper ligands) for bottom-up filling. Such an approach enables the elimination of the copper seed layer and allows plating directly onto the cobalt seed layer. The cobalt layer, therefore, acts as a passivating layer to prevent TaN oxidation, as a liner to ensure a good interface between TaN and copper, and as a conducting seed layer to allow electrochemical deposition. This newly developed alkaline chemistry has a pH of 9.1, while acidic chemistries typically have a pH below 2.

In this chapter, a cobalt thin film of 3 nm is investigated by dipping in three different solutions. Acidic copper chemistry, aveni's alkaline copper chemistry, and acidic copper-less chemistry are used as dipping solutions. X-ray photoelectron spectroscopy is used to characterize the 3 nm cobalt film's physical-chemistry when exposed for 5 seconds in the solutions cited before.

After investigating the dipping impact by XPS, electrochemical quartz crystal microbalance is used to deposit a well-controlled cobalt film thickness and study its reactivity in different solutions. Three following buffers are used; Alkaline buffer pH=10, acidic chemistry pH=1, and pH=4.

So in this introduction of Chapter III, we have presented all the key points of the Co/Co or Cu/Cu, which are mainly concerned then governed by the Co film's surface chemistry, which can all be addressed by quantitative XPS /XPS profiling approaches.

III.2 Annealing and bath pH impact on deposited cobalt film

Cobalt has a very rich photoemission response; nevertheless very complex to analyze when discussing the oxide phases of the alloys in which Co is involved. The structuring of chemical shifts for different chemical environments is very similar to that of Fe, Ni, Cu. The simulations of the XPS peaks are delicate for all these metals and are the subject of divergences or even confrontations. The purpose of this thesis is not to go into the details of the procedure for simulating Co signals emitted by partially or fully oxidized surfaces. We will work on continuous fundraising with standard algorithms while keeping the conditions and constraints always constant, which allows easy comparisons. The points detailed in this paragraph report the description of the energy distributions of photo-pic and Auger lines accessible with excitation with an aluminum anode (1486.6 eV) cobalt-based film, whatever its composition, will emit a certain number of lines which will all be usable. However, the Co2p region with a perfectly resolved spin-orbit coupling is by far the most exploited in the literature. We will also use this massif in our presentation.

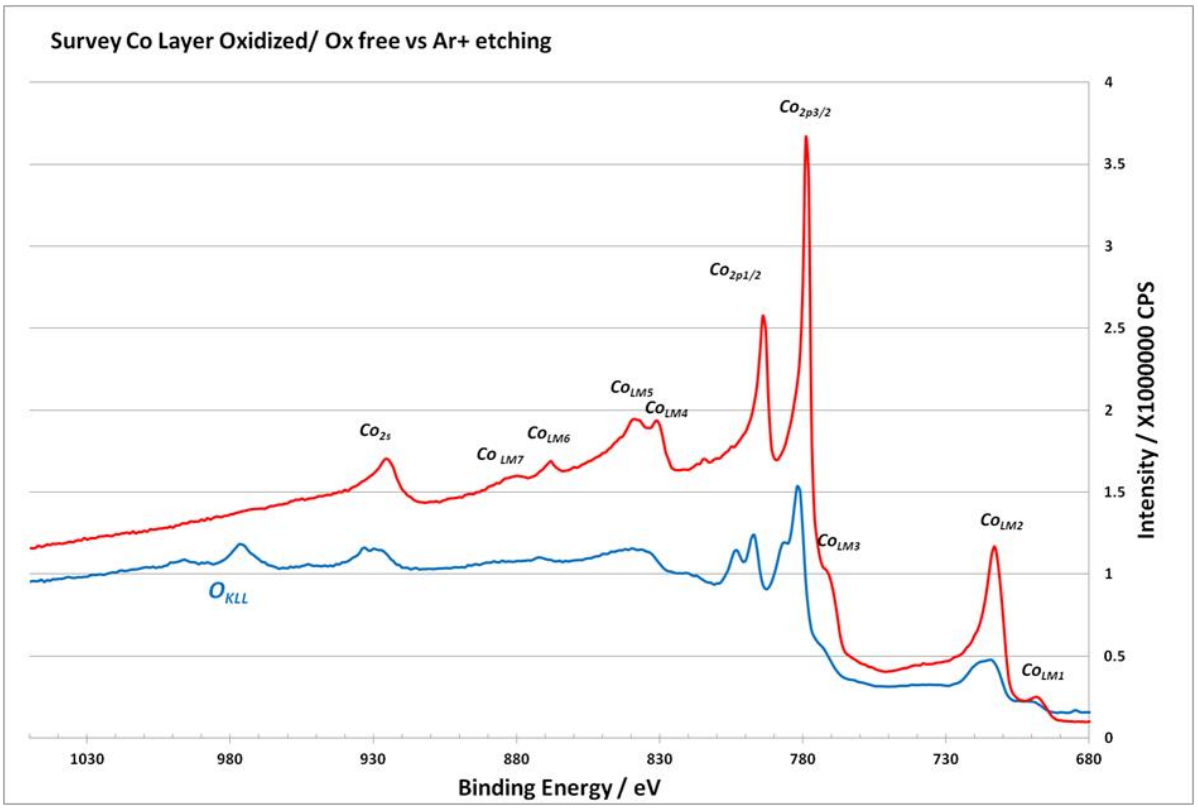

Figure III-1. *Spectra of photo peaks and Auger line in the 680-1050 eV binding energy range; blue line is associated to an oxidized Co surface (after annealing) red line is associated to a pure metallic surface obtained after sufficient Ar^+ bombardment and elimination of oxide traces.*

For Co films, Co3p, Co3s, Co2p, Co2s are the cores levels that are observed. The Co3d line is in the Valence band region. The spectra are also very rich in Auger line that are LMM lines. All the Auger lines are shown in the spectral region presented in Figure III-1.

III.2.1.Impact of Annealing

To investigate the Co film obtained by *Cowave*, XPS is used to analyze two samples of 400 nm deposited cobalt. The first film is analyzed as deposited. The second one is annealed at 450°C for 1 min. The annealing is performed under 4% H_2 in N_2 in rapid thermal annealing (RTA) ANNEALSYS AS-Micro furnace. For each sample, two analysis levels are performed—the first without Ar^+ sputtering to analyze the extreme surface. The second level is analyzed after 30 seconds of Ar^+ sputtering. The goal of this level is to eliminate the carbon contamination of the surface and analyze only the cobalt bulk. Figure III-2 shows the normalized Co2p spectra of two samples with and without annealing at t=0 and t=30 s second of Ar^+ sputtering.

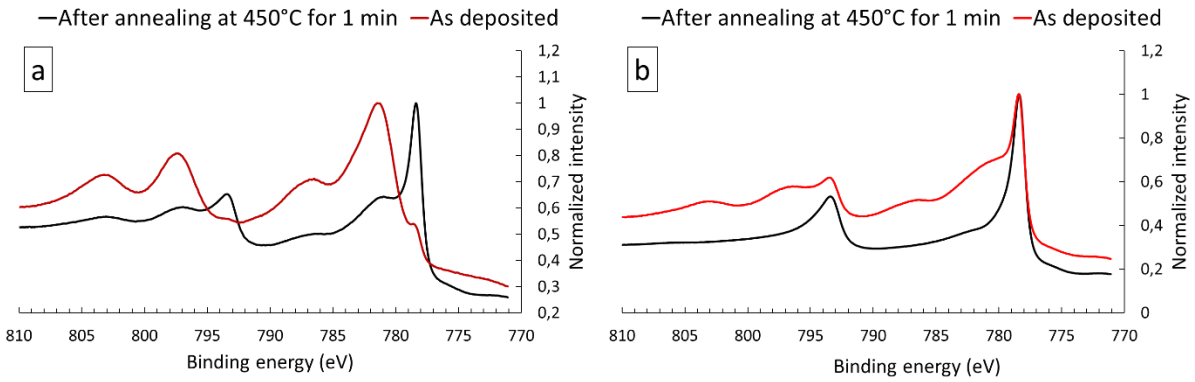

Figure III-2. *Normalized Co2p spectra of the as-deposited (red) and the annealed sample (black) without Ar^+ sputtering (a) and after 30 seconds of Ar^+ sputtering (b).*

The Co2p spectra are composed of two peaks at ~778.2 eV and 781 eV related to metallic cobalt and oxides, respectively. After annealing, the 778.2 eV peak related to metallic cobalt is intense compared to the 781 eV one. However, this result is inversed for the as-deposited sample. From Figure III-2.b, the spectra after sputtering show that after annealing, the Co2p peak is typical of metallic cobalt. While, in the as-deposited sample, the contribution of cobalt oxide at high energy is always present. This indicates that annealing impacts the chemical composition of the deposited film by reducing the oxygen amount. This result is confirmed in Figure III-3.

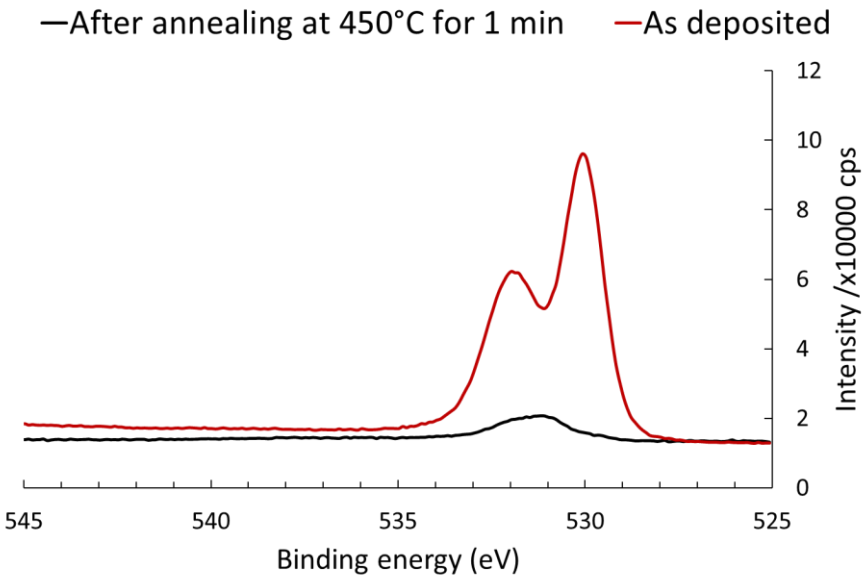

Figure III-3. *O1s spectra of the as-deposited and the annealed sample at t=30 s of Ar^+ sputtering.*

It is noticed that the intensity of O1s spectra decreased approximately by a factor of five after annealing.

The spectra of the Figure III-2 are normalized, which means that these results do not provide us an idea about the amount of Co in the film. In order to investigate the Co amounts, the spectra Co2p before and after annealing are presented in Figure III-4.a. After 30 s of Ar^+ sputtering, we noticed that the peaks intensity of the Co metallic is approximately doubled after annealing. This result can be explained either by the carbon screening due to carbon contamination or by the effect of the reduction of cobalt oxide due to annealing. To investigate precisely this result, the C1s spectra of both samples before and after annealing are shown in Figure III-4.b. The results of C1s shows that the intensities at both samples (before and after annealing) are almost the same; this result allowed us to eliminate the screening effect of carbon and confirm the reduction effect of annealing. For both samples, the C1s spectra have a double contribution. The first contribution, at low energy is related to C-C bonds (~284.8 eV). The second contribution, which we suggest is associated with a mix of C-O and C=O bonds at (~286 and ~289 eV). These contributions need more investigation of high-resolution spectra to associate it precisely to the corresponding environment. The second observation in Figure III-4.b concern the binding energy shift, in XPS the energy shift of C1s can be associated with the film's conductivity, and we are confident that the annealing increases the electrical conductivity of the film due to previous four-point probe measurements. However, the

attribution of the C1s binding energy shift remains partially unclear and requires further explorations of HR C1s spectra.

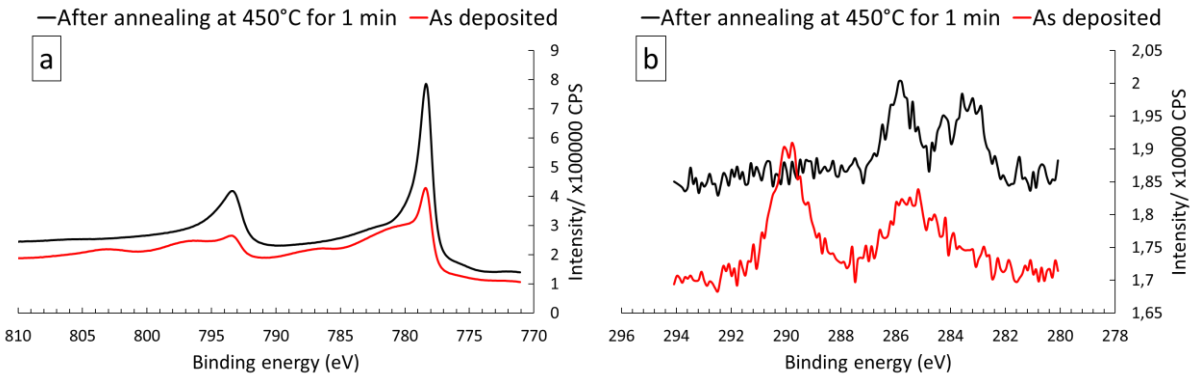

Figure III-4. *Co2p (a) and C1s (b) spectra of the as-deposited (red) and the annealed sample (black) after 30 seconds of Ar^+ sputtering.*

XPS results show us the importance of annealing on the chemical composition of the obtained film. To study the impact of annealing on grain size, X-ray Diffraction (XRD) is used on 200 nm cobalt films. The first analysis is performed on an as-deposited cobalt film. The second analysis was on an annealed cobalt film with the same annealing parameters used in the XPS study (450°C for 1 minute in 4% H_2 in N_2).

For this study, we suppose that the widening of the spectra is related only to the crystallite size effect. As cobalt is oriented 111, the measurement in the plane cannot be done on a low angle reflection. A 70° tilt is preferred for this analysis (see Figure III-5).

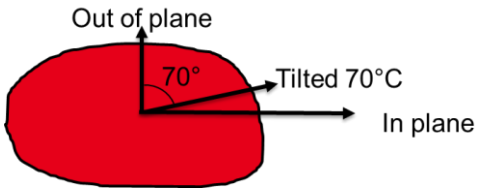

Figure III-5. *XRD analysis plan*

For calculation, the Scherrer method is used according to Eq. III-1.

$$DCD = \frac{0.9.\lambda}{\beta.cos\theta} \qquad \textit{Eq. III-1}$$

Where: λ is the X-ray wavelength; β is the line broadening at half the maximum intensity (FWHM); θ is the Bragg angle and 0.9 is a dimensionless shape factor.

Figure III-6 shows the texture of the as-deposited and annealed Co films using X-ray diffraction (XRD). It is clear that annealing enhances the film texture at each angle.

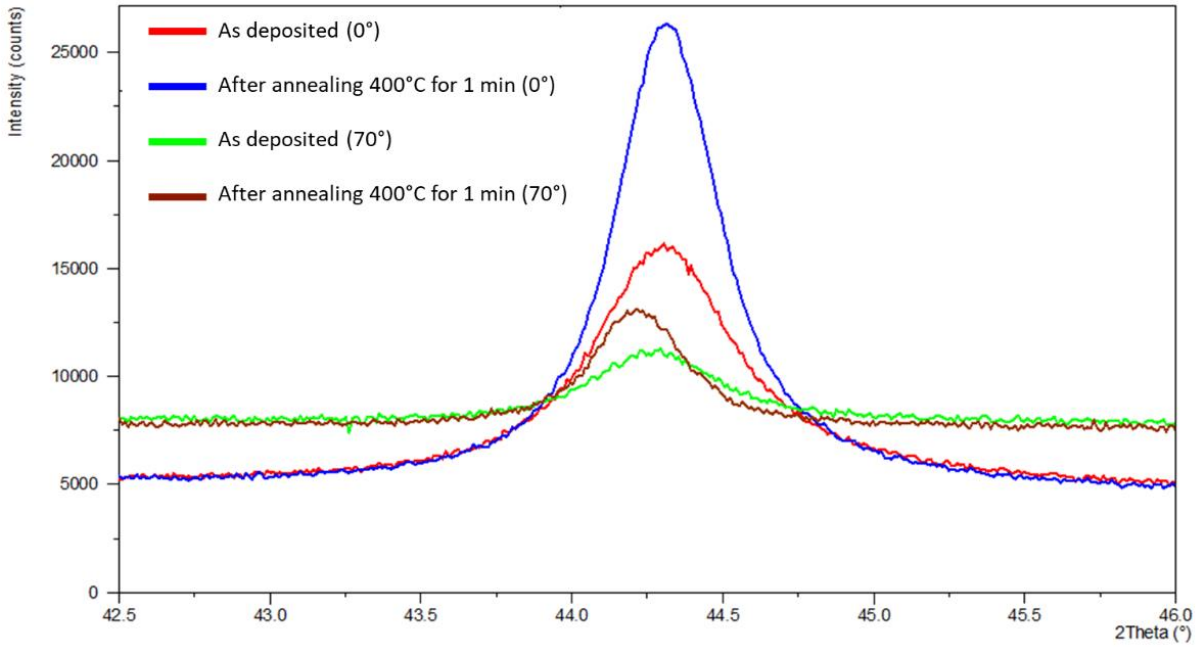

Figure III-6. *X-ray diffraction data for as-deposited and annealed Co films at 0° and 70° of analysis angle.*

The data obtained are presented in Table III-1. The results confirm that the grain size increase after annealing. The size changes from 29.4 nm before annealing to 62.3 nm after annealing.

Table III-1. *XRD data of as-deposited and annealed cobalt film*

Sample	Tilt (°)	Position (°)	Area	FWHM (°)	DCD (angst.)
As deposited	0	44.265	1265	0.539	231
Annealed	0	44.275	1757	0.336	431
As deposited	70	44.232	305	0.459	294
Annealed	70	44.179	372	0.305	623

III.2.2.Impact of bath pH

The strict control of the solution pH is critical to the quality of the cobalt deposit. An extremely low pH value will cause excessive hydrogen evolution reaction, leading to pitting corrosion problems. On the other hand, if the pH of the solution is too high, a cobalt hydroxide layer may be formed, which reduces the electrical properties of the deposit [9].

To evaluate the pH impact on cobalt film composition, three substrates of 400 nm of cobalt are electrochemically deposited on Co seed (3 nm)/TaN barrier/Tetraethyl orthosilicate (TEOS).

To deposit the cobalt film, Cowave is used with three different pH values pH=2.2, pH=3.2, and pH=4.7. Tetraethylammonium hydroxide (TEOH) is used to increase the initial pH value of Cowave and obtain pH=3.2 and pH=4.7. The 400 nm thick Co layer is introduced in an ultra-high vacuum (UHV) chamber of a XPS NEXSA Thermo Fisher Spectrometer. The XPS measurements were performed using a monochromatic Al Kα source. Calibration of the spectrometer was performed to give a metal $Au4f_{7/2}$ line at Binding energy (BE)= 83.95 eV. The spectrometer dispersion is verified using the ASTM-E-902-94 standard procedure using Cu and Au Samples. X-Ray spot sizes of 400µm, High resolution (20 eV) Constant Energy Analyzer Mode (CAE) with 0.1 eV as energy step, are used for the spectra recording. Data are processed using the Thermo Fischer Avantage@ software.

Figure III-7.a shows Co2p spectra of cobalt electroplated film obtained at different Cowave pH values.

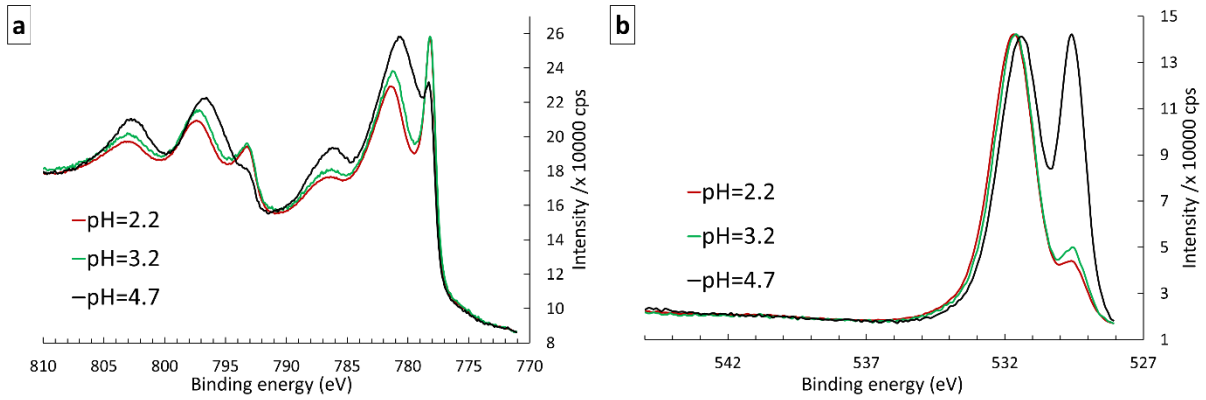

Figure III-7. *Co2p spectra (a) and O1s spectra (b) of cobalt deposited at different pH values.*

In Figure III-7.a, three similar regions for the $Co2p_{3/2}$ and $Co2p_{1/2}$ core levels are observed. The first peak at 778.2 eV is associated with the metallic cobalt response. The second peak is observed at approximately 781 eV. This peak is corresponding to cobalt oxides. At pH=2.2 and pH=3.2, the Co metallic peak is more intense than the oxides peak. However, at pH=4.7, the oxides peak intensity exceeds the Co metallic peak. Comparing the oxides peak intensity, it is clear that as the pH increase, more oxides are formed. To evaluate this phenomenon, the O1s spectra of the same samples are shown in Figure III-7.b. In the O1s spectra, two peaks are present at 529.5 eV and 531.5 eV. The peak at low energy is related to metal oxide. This peak

is more intense at pH=4.7. The second peak is related to other oxides environments. It can be concluded that in the first 10 nm of the deposited film, the cobalt is more oxidized at pH=4.7 compared to pH=2.2 and pH=3.2.

To investigate the bulk of the electrodeposited film, Ar^+ beam sputtering (2000 eV, 10 mA, crater size ~2 mm x 2 mm) is used. The etching time is set to 60 seconds. We suppose that the Ar^+ etching rate is the same for all three samples. Figure III-8 shows the obtained O1s spectra.

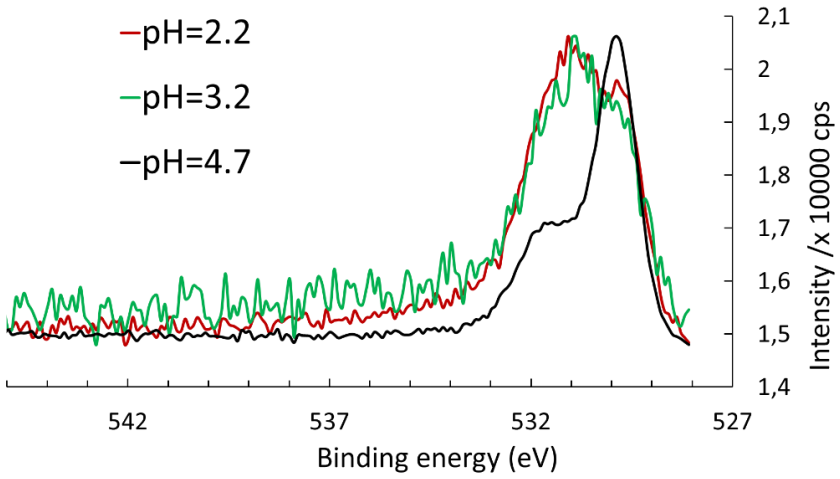

Figure III-8. *O1s of the electrodeposited film at different pH baths after 60 seconds of Ar^+ sputtering.*

Two peaks are present for the three analyzed samples. However, the peak at low energy is intense at pH=4.7 compared to the other pH's. This result is also confirmed by the amount of oxygen at pH=4.7, which is four times more than the oxygen amount at pH=2.2 and pH=3.2. After 60 seconds of sputtering, the oxygen amount is totally related to cobalt. This due to the elimination of the oxygen linked to carbon contamination at this level of etching.

The electrochemical solution pH impacts the oxygen amount of the deposited film. This result is confirmed by XPS. After investigation of the three pH values, it was found that pH=2.2 is the best pH solution to obtain a cobalt film with low oxygen amount. The oxygen amount formed at pH=4.7 could also be related to cobalt hydroxide [9].

III.3 Cobalt film reactivity toward air-exposure

The understanding of the film electrodeposition mechanism is essential. Coupling electrochemistry and microbalance brought us very interesting results, which allowed us to control the deposited cobalt film. However, the deposition mechanism on itself is not enough.

In this thesis, the structure used for electroplating is shown in Figure III-9. The control of the Co surface chemistry and particularly its oxidation process are strategic. Conformal Co seed

characteristics (i.e., electronic conductivity) preceding the following filling chemistry are partially related to Co surface oxide behavior toward the filling step. Its understanding, then its control, will be determinant to obtain a perfect and reliable filling process of aggressive structures. Recently Q.*T. Le et. al*, [10] have considered the place of the Co surface chemistry toward different cleaning solutions, combining chemical consideration with optical and electrical ones. They provide interesting results about the role of the dissolved oxygen concentration and the nature of the acidic formulation in the modulation of the observed etching rates. One main result is that the oxide nature, analyzed by X-ray photoelectron spectroscopy (XPS) is a key parameter for the explanation of the observed variations.

Figure III-9. *Substrate used for electroplating.*

As illustrated in Figure III-9, the cobalt seed is only 3 nm. This critical thickness is exposed to both air and chemistry during electroplating. This cobalt seed layer is exposed to air during the assembly of the cathode before the electroplating in minireactor, and to chemistry when immerged in Cowave acidic chemistry before launching the electrical process. To assess the cobalt seed film behavior when exposed to air, a 400 nm of cobalt is electrochemically deposited on Co seed (3 nm)/TaN barrier/Tetraethyl orthosilicate (TEOS). The 400 nm thick Co layer (step 1 Figure III-10) is introduced, with its native oxide, in ultra-high vacuum (UHV) chamber of a XPS NEXSA Thermo Fisher Spectrometer. The XPS measurements were performed using a monochromatic Al Kα source.

As a reference sample, a totally deoxidized Co surface is obtained with an Ar^+ beam sputtering (2000 eV, 10 mA, crater size ~2 mm x 2 mm) (step 2 Figure III-10). The initial oxide free bulk metallic Co is then checked by XPS (step 3 Figure III-10). Starting from this surface, we explore again using XPS, the consequences of different air exposure times inside the etching crater. Air exposure is performed in the entrance preparation chamber of the spectrometer (step 4 Figure III-10). The sample was transferred from the analysis chamber in the entrance one under UHV. Again, the chamber was vented and filled with pure nitrogen, then the chamber

was opened for different time air exposures. The chamber was closed again and was pumped, then the sample after its time-controlled exposure was transferred for a new XPS characterization (step 5 Figure III-10). According to the air exposure time, the oxide growth mechanism's kinetic can be evaluated by comparison between the different spectra taken on the same point. Note that the position accuracy of the sample manipulator allows successive analyses in the same sample position at less than 5 µm, inside the etching crater.

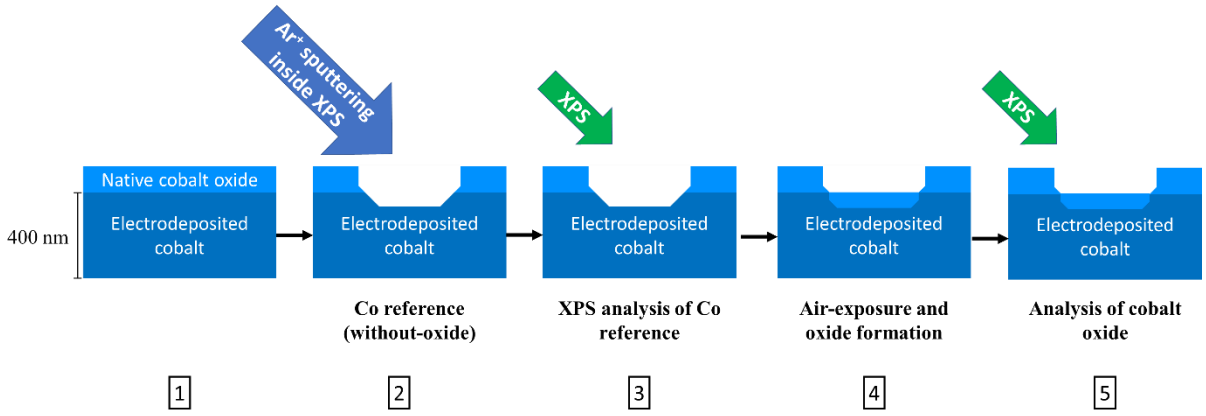

Figure III-10. *Schematic of Co-Air reactivity study using XPS 400µm spot size.*

Figure III-11 shows how the Ar^+ sputtering modifies the initial as grown Co surface. Starting from a typical oxidized Co surface, we show three sequential etching levels that demonstrate that the initial Co2p binding energy repartition is strongly modified and reaches a steady-state after 120 seconds of abrasion.

The associated XPS response is specific of a metallic deoxidized surface. Note that this new response inside the crater is stable under UHV conditions. The binding energy repartition is constituted of three similar regions for the $Co2p_{3/2}$ and $Co2p_{1/2}$ core levels. At low BE, a first narrow peak is always observed (~778.2 eV). It is associated to the response of the metallic network. Note that every time this peak is present on the initial surface meaning that the oxide even for long oxidation time is thin at the XPS scale. As the etching time increases this peak becomes more and more intense until its stationary height (120 seconds). A second broad peak close to 780 eV and third one close to 786.6 eV are related to the top oxide over layer. These double linked structures decrease as the etching time increases to be eliminated when the low binding energy component reaches its stationary state. So, the Ar^+ beam etching allows obtaining a well reproducible metallic cobalt all over the crater surface. This cobalt layer will serve as a reference surface for this study.

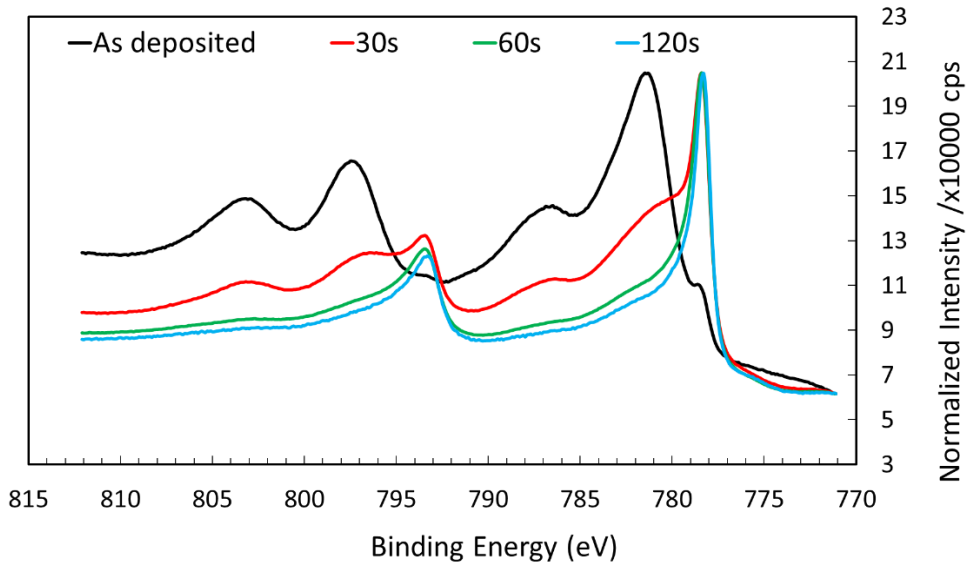

Figure III-11. *Co2p spectra evolution during Ar^+ sputtering. Spectra are obtained after different etching times.*

Starting from this surface, we explore again by XPS, consequences of different air-exposure times using the entrance preparation chamber of the spectrometer as a reactor. According to the time air-exposure, the kinetic of the oxide growth mechanism can be evaluated, as shown in Figure III-12.

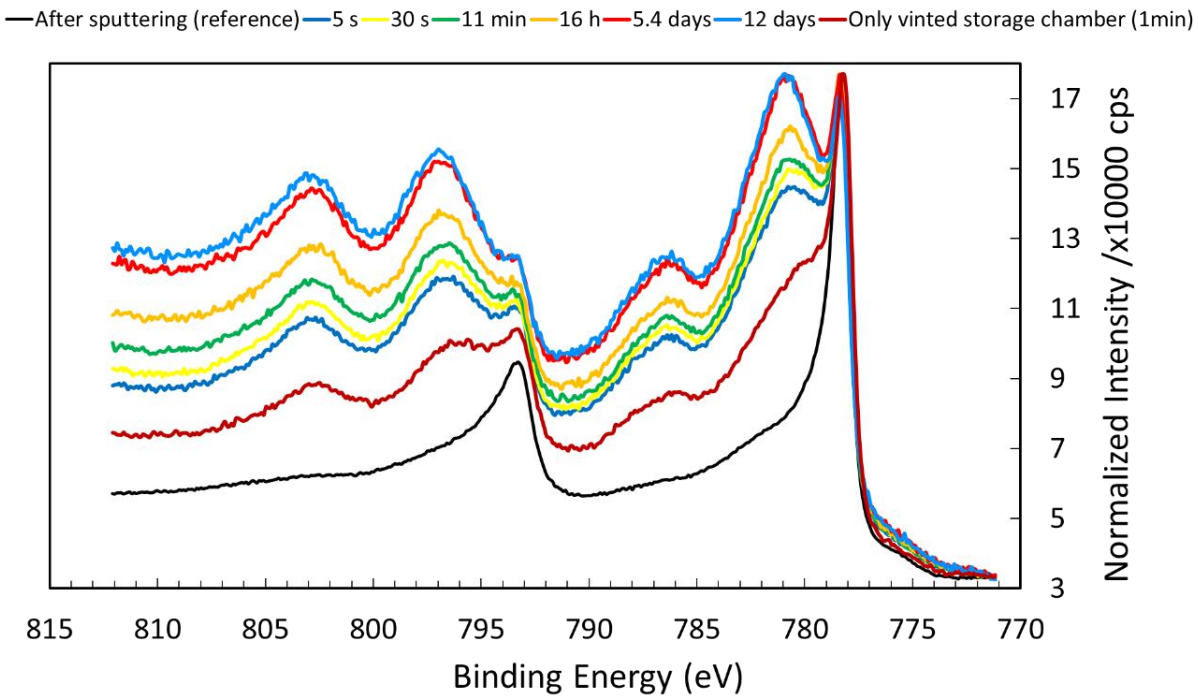

Figure III-12. *Co2p spectra at different air-exposure time.*

Our results clearly show that the metallic Co surface evolves very quickly toward an ultra-thin (nm range) oxide capping layer whose thickness will increase progressively with the time

of air exposure. A main result is that the metallic signal of the buried metallic Co is always present even for very long-time air-exposure (here 12 days). These results indicate a phenomenological trend over the oxide thickness limitation. In our specific study, using our kinetic features associated to the progressive increase of the oxide Co2p contributions (as described above), we demonstrate a very reproducible evolution in time as in spectral modifications of the Co2p energy distribution. Considering in detail the relative evolutions of the Co2p region, it is obvious that a consequent Co2p modification is observed only during the entrance chamber filling by N_2 gas before the opening of the chamber for air interaction. This intermediated oxidation feature can be explained by small leakage in the gas filling circuit. It illustrates that the metallic surface is hypersensitive to residual oxygen amount. Starting from this initial point it is also clear that short chamber opening time (5 seconds) generate again a large increase of the oxide contribution confirming the strong initial reactivity of metallic Co toward oxygen. Then for longer time air exposures the trends to a surface oxidation on the same point decrease progressively indicating as a limiting oxide thickness. This observation is consistent with other observations performed on the Co seed layer or in our electroplated Co layer. Concerning the nature of the oxide, O1s illustrated in Figure III-13 should be investigated.

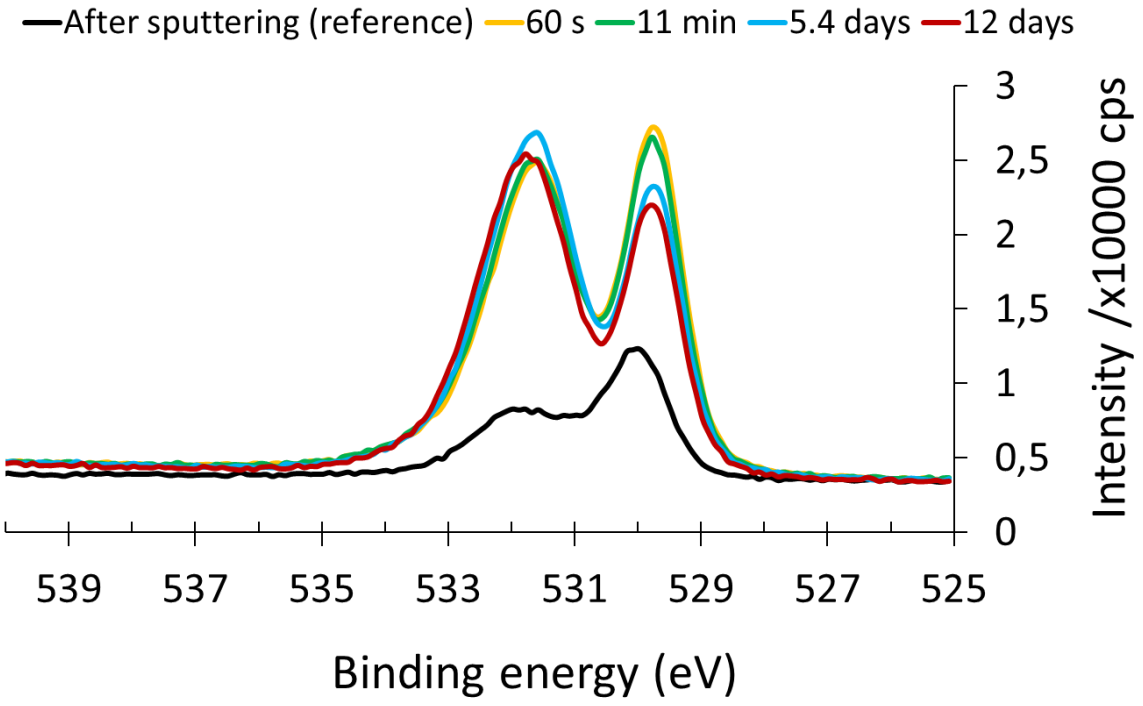

Figure III-13. *O1s spectra at different air-exposure time.*

Figure III-13 describes the evolution of the O1s spectra of the deposited Co at different air-exposure times. The binding energy repartition is constituted of two regions for the O1s spectra. At low BE, a first peak is observed (~529.6 eV). It is associated to the response of the metal oxide. This peak is present even in the initial surface (after sputtering). However, the intensity of this peak is very weak, meaning that a small amount of oxide is present on the Co film even after sputtering. This is supposed to be related to the dissolved oxygen in the XPS chamber. The second peak is observed at (~531.5 eV). As there has clearly been little work done to understand cobalt oxides chemical environment, it is difficult to confirm the nature of this peak. However, the most accurate conclusion is that there are two oxide types present in our film. A part of the peak at high energy is associated to carbon contamination.

From Figure III-13, we can see that the O1s peaks intensity change as a function of air-exposure time. The intensity of the O1s peak at low energy is decreasing when the film is exposed to air for long time (12 days). However, the peak's intensity at high energy increase at long time air-exposure. The atomic compositions of the analyzed levels are illustrated in Table III-2.

Table III-2. *Chemical composition of cobalt films at different air-exposure durations.*

Atomic %	After sputtering (reference)	t=30 s	t=60 s	t=11 min	t= 5.4 days	t= 12 days
Cobalt	79.29	48.07	46.05	43.13	32.40	24.56
Oxygen	15.81	39.8	39.31	40.62	42.01	44.37
Carbon	4.90	12.13	14.63	16.25	25.59	31.08

From the above results (see Table III-2), our estimation of the oxidation kinetic of metallic Co demonstrates a very high reactivity toward oxygen followed by a stabilization of the oxide amount. The oxygen amount passes from ~15.8% to approximately 40% after only 30 s of air-exposition. The carbon contamination amount is also increasing due to the exposition time of the sample to air. The confirmation of the presence of a metallic signal presented under the oxide response also indicates the limitation of its thickness which is in the nanometer range.

Concerning the nature of the oxide layer, we can already assume, considering the literature [11][12], that a mixture of CoO and $Co(OH)_2$ must be considered as resulting from our oxidation process.

III.4 Cobalt film reactivity in chemistries

III.4.1.Reactivity vs copper plating chemistries

In this study, integrations using cobalt (typical seed) planar film stack was exposed to alkaline and acidic plating chemistries for a short time that are typical of the actual processes to assess their stability. The objective of this study is to highlight the different chemical and physical mechanisms occurring during the first steps of an electroplating process. Blanket coupon samples with a thin layer of either cobalt, deposited on a thin layer of TaN, were analyzed using X-ray photoelectron spectroscopy (XPS) before and after exposure to the electroplating solutions.

The samples were fabricated in a cleanroom environment. One integration scheme was studied, using monocrystalline silicon <100> substrate on which 200 nm of thermal SiO_2 oxide was grown. A 2 nm barrier TaN layer is first deposited using CVD. Finally, 3 nm of Co is deposited by CVD corresponding to the integrations illustrated in Figure III-14.

Figure III-14. *Integration used for dipping in chemistries study.*

All substrates were stored in a nitrogen environment. To assess their behavior in contact of the solutions before and during the process, two copper plating solutions and a copper-less variant were used in this study in dipping conditions, as described below (see Table III-3). The first copper solution has a pH of 2 and will be referred to as the "Acidic copper solution". It consists of 5 g/l of $CuSO_4$ pentahydrate with 50 ppm of HCl, to which H_2SO_4 is added to reach a pH of 2. PEG 200 ppm. Molar weight of 600 g/mol is added as a suppressor and 1 ppm of bis(sodiumsulfopropyl)disulfide (SPS) is used as an accelerator. Before use, nitrogen gas is thoroughly bubbled through the acid solution for 15 minutes to remove the dissolved oxygen. A copper-less acidic variant (the same components at the same concentration except for copper) has also been studied. The second copper plating solution has a pH of 9.1 and will be further referred to as the "Alkaline copper solution". It is a proprietary solution developed by aveni®,

which is described here [6]. The solution is a combination of three different ligands in a Copper-sulfate-based solution. An additional organic component is added to adjust the pH to 9.1.

Table III-3. *List of experimental tests performs during this study.*

Initial substrate	Chemical treatment	Time
SiO_2/TaN (2 nm)/ Co (3 nm)	No	/
	Alkaline copper solution (with copper)	5 seconds
	Acidic solution (with copper)	5 seconds
	Copper-less acidic solution (without copper)	5 seconds

The processing protocol of the substrate in the solutions is as follows (see Figure III-15): the substrate is introduced into the solution for 5 seconds. The substrate is then thoroughly rinsed with deionized water and dried with nitrogen, and it is then quickly mounted in a sample holder and introduced into the XPS system for analysis.

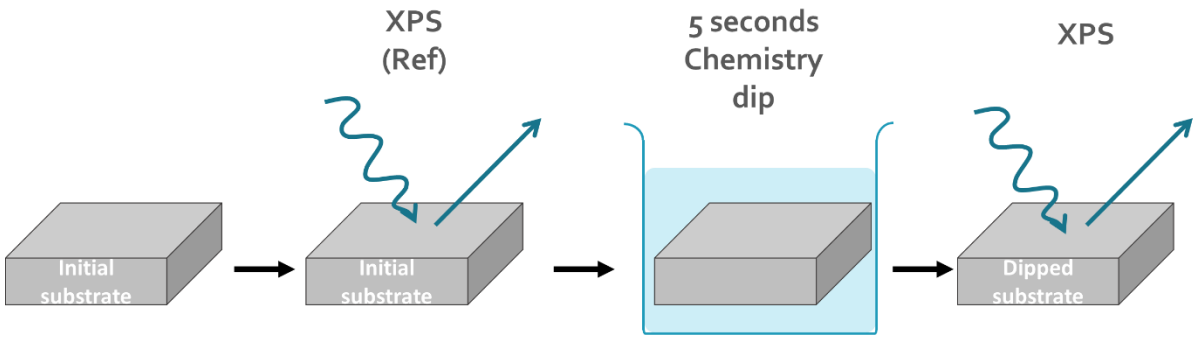

Figure III-15. *Diagram of chemistry dipping study of substrate A (3 nm Co seed) and B (10 nm Co seed) using XPS.*

The substrate is investigated in four conditions: no treatment, 5 seconds in acidic copper solution, 5 seconds in alkaline copper solution, and 5 seconds in copper-less acidic solution. XPS surface chemical analyses are carried out with a Thermo Electron K-Alpha spectrometer using a monochromatic Al-Kα X-Ray source (1486.6 eV). The Thermo Electron K-Alpha spectrometer procedure was used to calibrate the spectrometer and verified using Cu and Au samples following the ASTM-E-902- 94 standard procedure. Acquisition parameters of high energy resolution photopeaks are: 400 µm spot size, 12 kV primary energy, 6.0 mA emission intensity, Constant Analyzer Energy mode (CAE) 50 eV or 10 eV with 0.1 eV or 0.05 eV

energy step size, respectively. Data are processed using the Thermo Fisher scientific Avantage© data system. XPS composition is obtained using a Shirley background subtraction and Sensitivity Factors from Avantage© library, taking account for the transmission factor and inelastic mean-free paths.

The Figure III-16 shows specifically the Co2p region spectrum of the non-treated substrate (black) and the dipped substrate for 5 seconds in the different chemistries: acidic copper treatment (orange), acidic copper-less (green), and alkaline copper solution (blue). In all treatments, the sample contains two peaks, Co oxides at ~781.4 eV and metallic Co at approximately 778.0 eV [13]. The presence of the two peaks in the initial substrate means that even in the initial state, the substrate is oxidized. From Figure III-16, the ratio between cobalt metal and cobalt oxide is increased after alkaline treatment. This can be explained by the slow etch rate of the cobalt native oxide layer by the alkaline solution. However, after dipping in acidic copper-less chemistry, the ratio Co/Co-oxides are lower compared to the alkaline copper solution. Concerning the dipped cobalt in the copper acidic chemistry, the Co2p peak decreased hugely in intensity, which means that acidic copper solution etches almost all the cobalt seed.

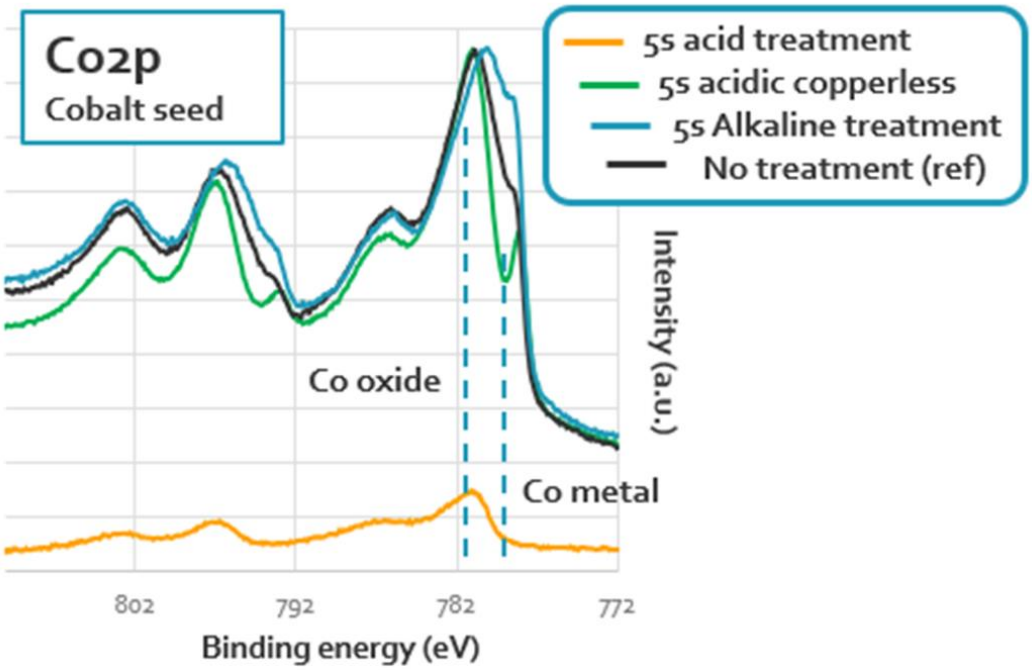

Figure III-16. *Co2p XPS spectra of 5 seconds dipped Co seed in different chemistries: acidic copper solution (orange), acidic copper-less (green), alkaline copper solution (blue), and no treatment (black).*

To investigate the behavior of cobalt film after dipping, the atomic compositions of different samples are obtained from the XPS survey and is presented in Table III-4.

The results show the presence of Co, O, C, and Ta. The presence of oxygen can be related either to cobalt oxides or to carbon contamination. However, the tantalum is detected even in the initial substrate because of the XPS analysis depth, which is ~10 nm. The ratio Co/Ta gives us an idea of the etching phenomenon. This ratio passed from 12.06 to 3.06 after dipping in copper-less acidic solution, which means that the latter solution etches the cobalt film. Concerning acidic copper solution, the ratio pass from 12.06 to 1.28, and the same behavior as the acidic is observed. In the alkaline copper solution, the Co/Ta ratio pass from 12.06 to 13.5 which means that the etching rate is very low compared to acidic solutions. One of the mechanism responsible for cobalt etching is the dissolution of cobalt, as shown in Eq. III-2 in an acidic medium and Eq. III-3 in an alkaline medium in the presence of oxygen [14].

$$Co + 2H^+ \rightarrow Co^{2+} + H_2 \qquad \textit{Eq. III-2}$$

$$Co + \frac{1}{2}O_2 + H_2O \rightarrow Co^{2+} + 2OH^- \qquad \textit{Eq. III-3}$$

Table III-4. *The atomic composition obtained from XPS survey for different treatment in chemistries.*

Treatment	Co2p	Cu2p	O1s	C1s	Ta4f	Co/Ta
No	24.61	/	51.66	21.7	2,04	12.06
Alkaline copper solution (with copper)	36.03	1.55	41.10	17.65	2.67	13.5
Acidic solution (with copper)	15.43	5.42	47.19	19.90	12.05	1.28
Copper-less acidic solution (without copper)	24,95	/	48,01	18.89	8.15	3.06

After analyzing the atomic composition, the high-resolution spectra of Cu2p3 are presented in Figure III-17. As shown, the Cu2p peak at 933 eV is not present in non-dipped cobalt film. However, this peak intensity increases drastically after dipping in acidic copper chemistry compared to the sample dipped in the alkaline copper solution. We suppose that another mechanism that can be responsible for this rapid etching in copper acidic chemistry is hinted in the $Cu2p_{3/2}$ high resolution spectra in Figure III-17. In the alkaline case there is also a smaller peak at 734 eV that corresponds to copper (II) oxide. These results suggest that there is a

galvanic displacement of the cobalt metal into the copper metal on the surface [14]. This is a very fast reaction using the acidic solution, resulting in a copper metal layer. The suggested equation of the reaction occurring is the following (see Eq. III-4):

$$Co + Cu^{2+} \rightarrow Co^{2+} + Cu \qquad \textit{Eq. III-4}$$

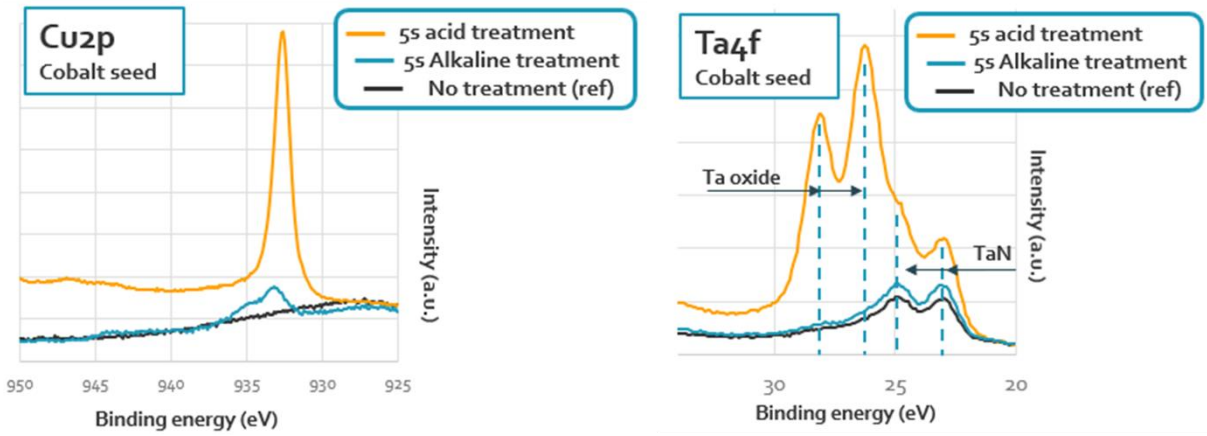

Figure III-17. *Cu2p (left) and Ta4f (right) XPS spectra of 5 seconds dipped Co seed in different chemistries: acidic copper solution (orange), alkaline copper solution (blue), and no treatment (black).*

The same phenomenon is occurring in the alkaline solution as well. However, in the alkaline solution, the deposition rate is significantly slower (due to the lower Cu^{2+} ions concentration as well as the stabilization of copper ions by ligands) than in the acidic solution, yielding a thin copper oxide layer due to the prevalence of hydroxide ions at high pH that can facilitate the following reaction (Eq. III-5):

$$Cu^{2+} + 2HO^{-} \rightarrow CuO + H_2O \qquad \textit{Eq. III-5}$$

The contribution of each mechanism (galvanic displacement and chemical etching) in the case of the acid solution can be evaluated from the results obtained when dipping the substrate 5s in the copperless acid chemistry. The observed relative stability of the cobalt seed in the copper-less acid chemistry compared to the acid plating solution suggest that the galvanic displacement is the highest contributor to the rapid degradation of the cobalt layer and the subsequent barrier oxidation.

The Ta4f spectrum of the non-treated cobalt and the sample dipped in the alkaline copper solution presented in Figure III-17 show peaks at 23 eV and 25 eV corresponding to the TaN. In both substrates, there is no peaks at 26 eV and 28 eV, which correspond to Ta oxide (Ta_2O_5). Comparing the two spectra (non-treated and alkaline chemistry treatment), there is a slight increase (~15%) of the peak area that can be attributed to the slow etching of the copper and cobalt seed. With a thinner seed, photoelectrons originating from the TaN have a higher

probability of escaping. Thus, the peak intensity increases. In the case of samples dipped in acidic chemistry, a much larger increase of the overall peak intensity of the TaN layer is observed that can be attributed to the thinning of the seed layer caused by rapid etching. The presence of both nitride peaks at 23 eV and 25 eV and oxide peaks at 26 and 28 eV in both integrations suggest that the TaN layer is partially oxidized. The ratio between the non-treated cobalt and alkaline case the TaN/Ta_2O_5 ratio is roughly 2. However, it is 0.35 for the acidic case with an overall peak area increase by 1000%. This signals a severe instability of the cobalt seed in acidic chemistry even after only 5 seconds [15]. These results show that the copper deposited through galvanic displacement by the acidic chemistry does not prevent the oxidation of the underlying TaN as seen in Figure III-17. This can be explained by the fact that the copper deposited is probably not continuous.

Confirmation of alkaline solution compatibility with direct-on-cobalt approach is obtained with electrodeposition test on aggressive structures with a SiO2/TaN/Co stack integration. This has been done using aveni solution and SEM results are reported in Figure III-18. Such integration must be used with the help of pre-treatment such as plasma cleaning to remove cobalt oxide that can induce interface defects after copper plating. We show a void free copper filling of structure that have a 21 nm opening without any visible defects. We can also distinguish by contrast the copper filling with the Cobalt seed layer (with the TaN barrier). This highlights the potential use of alkaline copper chemistries with cobalt seed on advanced damascene structures.

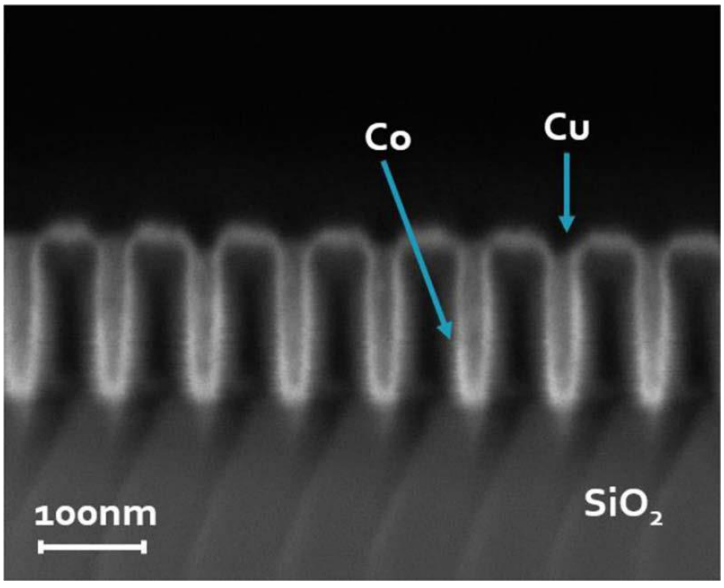

Figure III-18. *SEM image of TaN/Co stack after copper filling using electrochemical deposition with aveni® solution. Structures have an opening of 21nm after Co metallization and before copper plating. Image is obtained at a working distance of 2,6mm and with an accelerating voltage of 2kV. Magnification is at 100k.*

It is evident that the 3 nm cobalt seed layer is exposed to acidic chemistry Cowave before applying the electrical process. The time of immersion depends extremely on the electroplating operator, and it is so important to understand the behavior of the Co film in acidic chemistries.

It was noticed that the cobalt film is etched in the Cowave chemistry, and to evaluate this phenomenon confirmed by the thermodynamic data of Co^{2+}/Co (-0.28 V) and $H^{+}/H2$ (0.0 V). EQCM is used to deposit Co film using Cowave VMS chemistry by applying chronoamperometry at 1.5 $V_{Ag/AgCl}$ for 1 minute.

After obtaining a cobalt film with a thickness of approximately 145 nm, this latter is kept immersed in the deposition solution for 120 min at open circuit potential while the thickness is recorded via EQCM. Figure III-19 shows the evolution thickness of cobalt film during the process of deposition (CA -1.5 V for 1 minute) and the dissolution at OCP. This study confirms the dissolution of cobalt in Cowave chemistry with a dissolution rate obtained by a linear trendline of approximately -1.5 nm/min. The second important statement is the non-uniformity of the dissolution, as shown at the electrode surface (see Figure III-19). Two hypotheses are made for this phenomenon. The first one is that the dissolution rate is higher at the center of the electrode than the edges. The second is that the deposited cobalt thickness is higher at the edges than the center; thus, the cobalt is dissolved in the center at a higher rate.

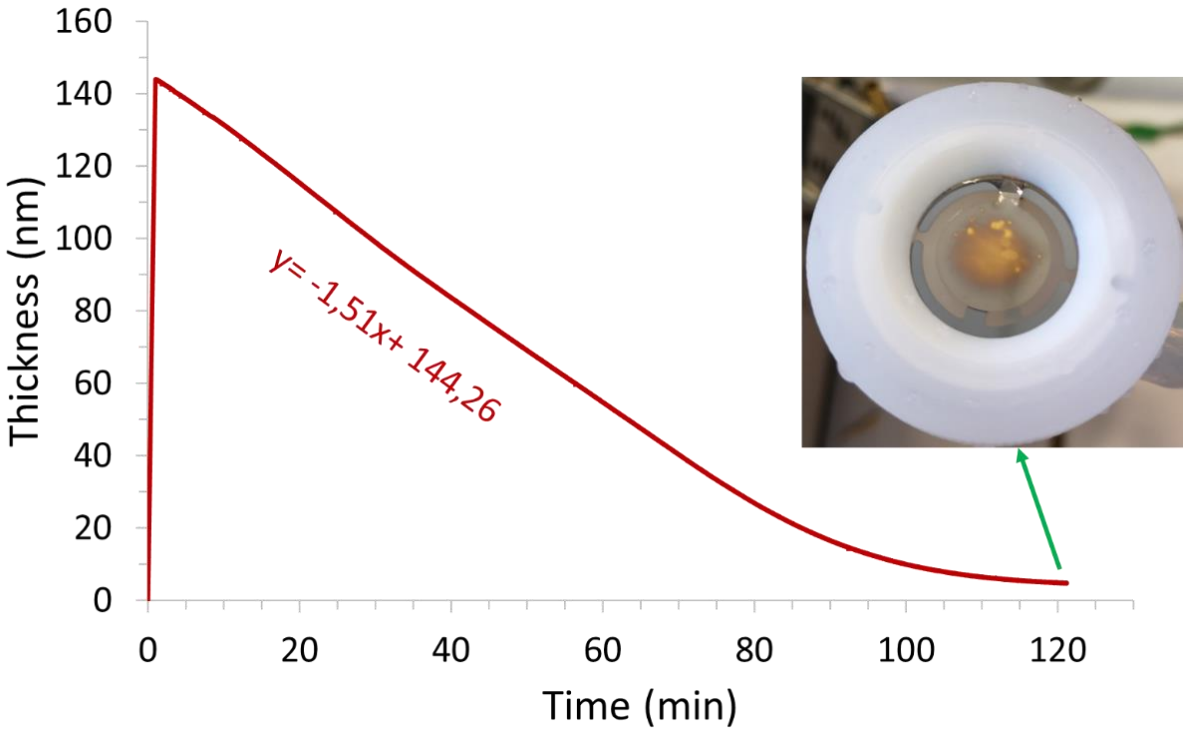

Figure III-19. *Dissolution of the cobalt film deposited in Cowave VMS (chronoamperometry -1.5 V for 1 minute) and dissolved at open circuit potential.*

A design of experiments is set up to assess how the Co seed layer behaves when exposed to different chemistries. This with coupling quartz micro-balance and electrochemistry. First, a cobalt layer is deposited on the Au working electrode (1.37 cm^2) by applying a chronoamperometry technique. -1.5 $V/_{Ag/AgCl}$ is applied for 30 seconds between the Au working electrode and AgCl reference electrode. A platinum sheet of 3 cm^2 is used as a counter electrode. The applied chronoamperometry process leads to the deposit ion of a cobalt film. This film is well controlled using electrochemical quartz crystal microbalance. After cobalt deposition, the working electrode is rinsed with deionized water and directly immersed in different chemistries. All immersions were performed under open circuit potential. The volume is 100 ml, and the chemistries used are presented in Table III-5.

Table III-5. *Chemistries used for immersion tests.*

Solution	Composition	$[H^+]$	$[OH^-]$	pH	O_2 in solution	Estimation of $[O_2]$ at 20°C [16]
A	H_2SO_4	10^{-1} M	/	1	- Saturated	5.6×10^{-4} M
					- Residual	-
B	Buffer by Specpure®	10^{-4} M	/	4	- Saturated	5.6×10^{-4} M
					- Residual	-
C	Buffer by Specpure®	/	10^{-4} M	10	- Saturated	5.6×10^{-4} M
					- Residual	-

As dissolved oxygen is an essential parameter, the immersion is investigated in both oxygen saturated and de-aerated solutions. Oxygen saturation is obtained by O_2 bubbling for 10 minutes before immersion. De-aeration is achieved by bubbling N_2 or Ar for 20 minutes before immersion, as well as during immersion. In the experiment's conditions, we assume that it is difficult to obtain a total de-aeration due to the uncovering of the solution tank.

III.4.2.Reactivity in acidic solutions

The thickness is calculated from mass change by taking into consideration the density of metallic cobalt 8.9 $g.cm^{-3}$. The thickness variation of the cobalt film immersed in pH=1 (solution A) and pH=4 (solution B) solutions are presented in Figure III-20 and Figure III-21, respectively.

Figure III-20 describes the evolution of the thickness of the cobalt film deposited on a gold working electrode after immersion in solution A. A noticeable decrease of cobalt thickness in both saturated O_2 and de-aerated chemistries is seen. This result is associated to the cobalt dissolution governed by the reaction (Eq. III-6) below:

$$Co_{(s)} + 2e^- \rightarrow Co^{2+}_{(aq)} \qquad \textit{Eq. III-6}$$

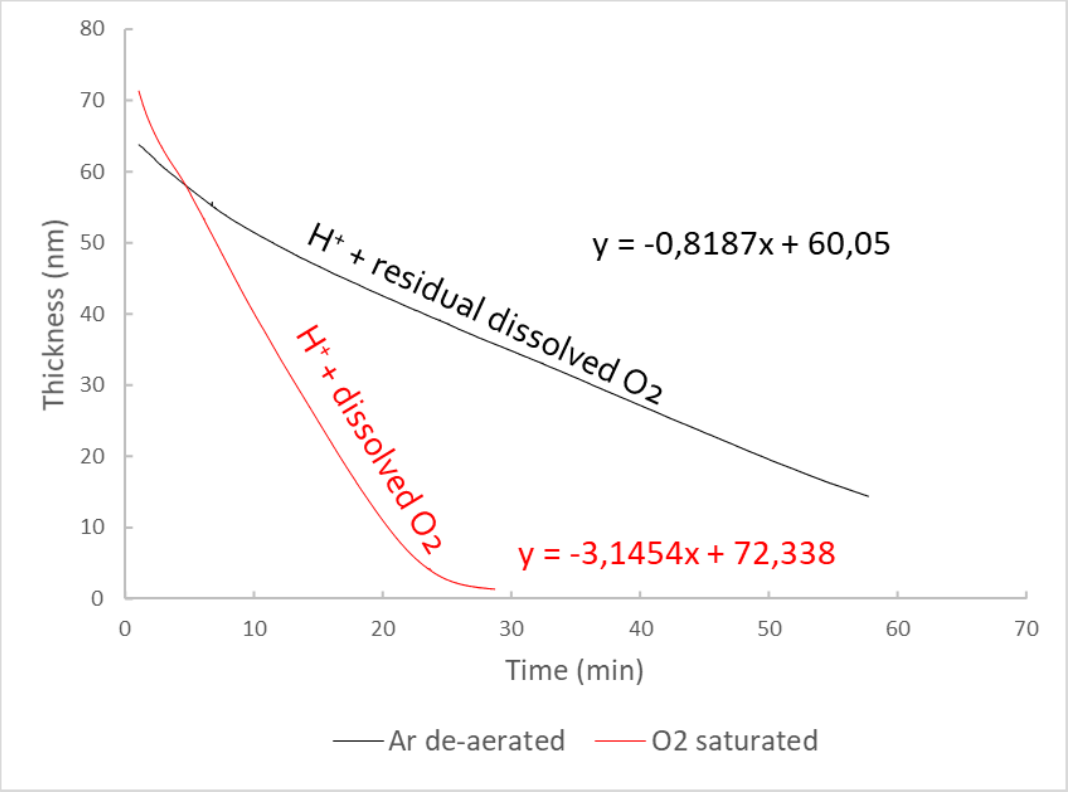

Figure III-20. *Thickness change of cobalt film immersion in pH=1 solution in partially de-aerated solution (black) and in O_2 saturated solution (red).*

The graph shows that Co dissolution occurs with different kinetics in both solutions. The dissolution rate is higher in saturated oxygen solution. To quantify this dissolution rate, a linear trendline is added to the linear parts of the curves to estimate the Co dissolution as a function of time. The dissolution rate in the de-aerated solution is approximately 0.82 nm/min. However, this rate is almost four times bigger (3.15 nm/min) in the O_2 saturated solution. These results confirm that the cobalt is dissolved in acidic media (solution A and B), and this dissolution is highly impacted by the O_2 concentration in solutions. In the case of cobalt dipped in pH=4 (solution B) solution, the same behavior is observed (see Figure III-21).

The dissolution rates are calculated by adding a linear trendline. The obtained dissolution rates are 0.45 and 3.14 nm/min in de-aerated and saturated O_2 solution, simultaneously. It is clear that the dissolution rate in oxygen saturated media is approximately the same in solution A and solution B. Despite the H^+ concentration variation from pH=1 to pH=4, the dissolution rates are in de-aerated solution are almost the same (0.45 and 0.82 nm/min). Considering that the amount of dissolved oxygen in de-aerated solutions are not well controlled, these dissolution rates difference is related to the amount of dissolved oxygen in chemistries. Thus, the amount of oxygen governs the kinetics of dissolution in acidic media.

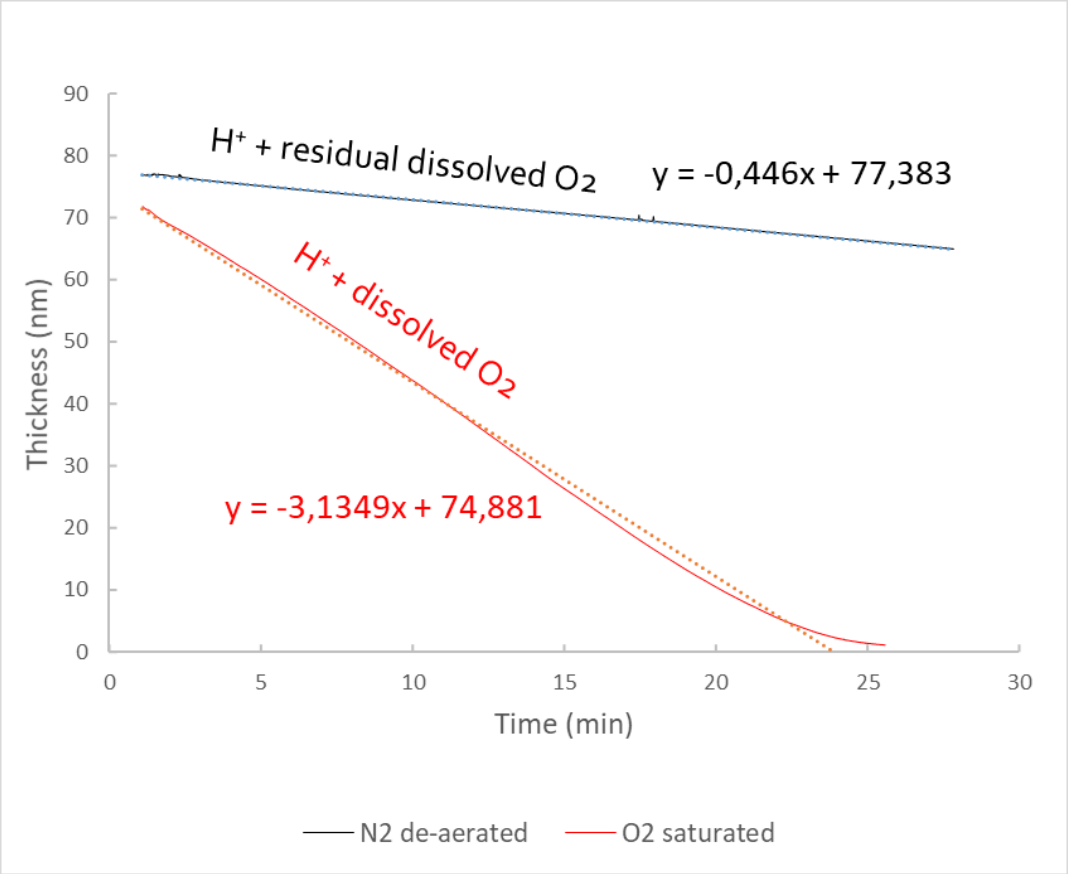

Figure III-21. *Thickness change of cobalt film immersion in pH=4 solution in partially de-aerated solution (black) and O_2 saturated solution (red).*

III.4.3.Reactivity vs alkaline solutions

The cobalt seed layer serves as a conducting layer in the electroplating process. As this layer is exposed to acidic chemistries, it can also be exposed to alkaline solutions during electroplating. For that reason, a study was performed in alkaline pH=10 buffer solution (solution C). This study consists firstly of depositing cobalt on a gold electrode. Then, the obtained layer is immersed in alkaline solution C. During this study, EQCM is used to track the mass change. The mass is tracked instead of thickness due to the unknowledge of the density.

Figure III-22 shows the mass change-time evolution of the immersed Cobalt film in the alkaline buffer pH=10 (solution C).

When Co is immersed in the de-aerated solution C, the mass of deposited cobalt remains unchanged (about 80 µg). However, a change in mass is observed after immersion in the O_2 saturated solution C. The mass evolution-time graph in O_2 saturated solution C is constituted of three parts. A first mass increase by 2.32 µg/min from 1 to 5 minutes. A second mass increase by 3.14 µg/min from 5 to 9 minutes, and finally, a steady mass plateau is recorded.

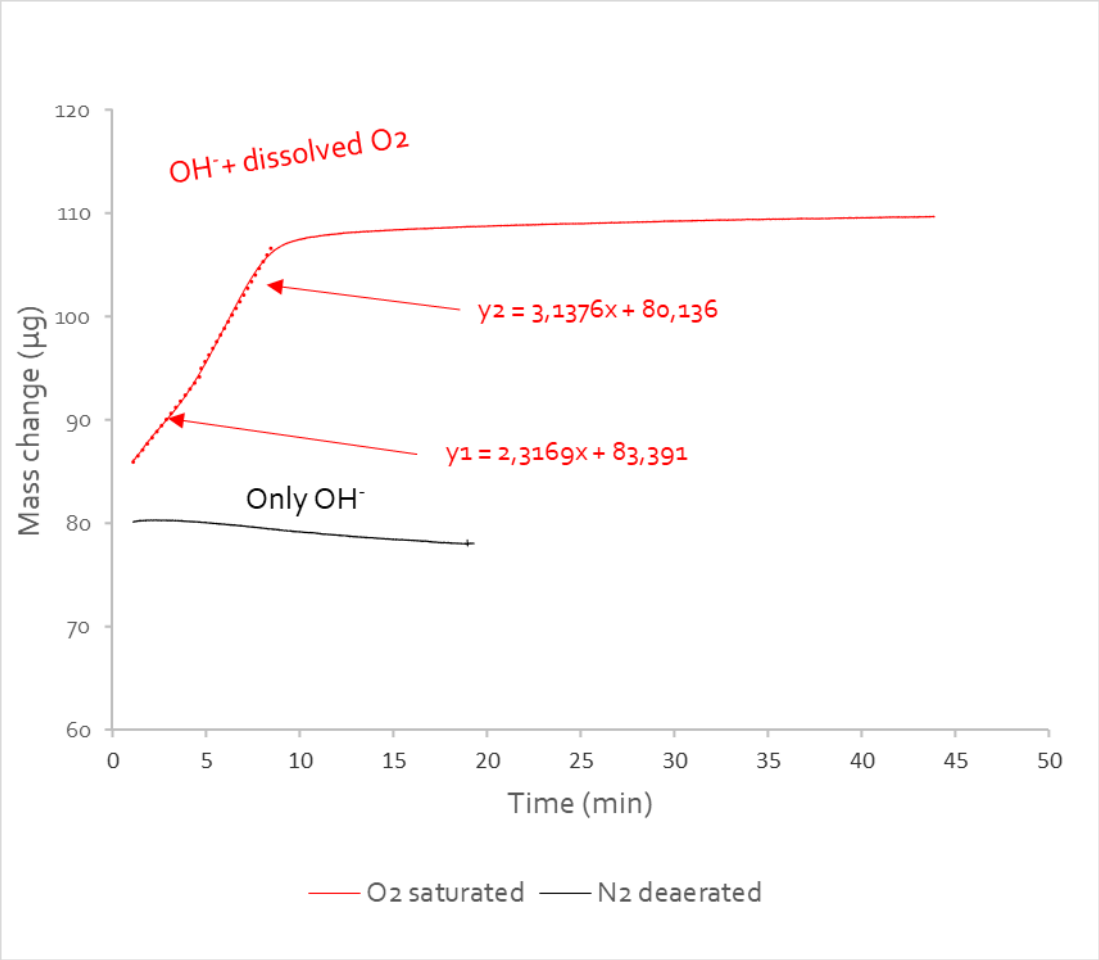

Figure III-22. *Mass change of cobalt film immersion in pH=10 solution in partially de-aerated solution (black) and O2 saturated solution (red).*

The mass increase is significant for the formation of new species. As shown in Figure III-22, these species are formed with two different rates, 2.32 and 3.14 µg/min. At pH=10, the possibility of hydroxide formation is not negligible.

Therefore, a mechanism hypothesis is proposed which is described in Eq. III-7, Eq. III-8 and Eq. III-9.

First step: $Co \rightarrow Co^{2+} + 2e^-$ *Eq. III-7*

And $O_2 + 2H_2O + 4e^- \rightarrow 4OH^-$ *Eq. III-8*

Second step: $Co^{2+} + 2OH^- \rightarrow Co(OH)_2$ Eq. III-9

The first reaction is demonstrated during the immersion in solution A and solution B. In the second step, we suppose that the Co hydroxides formation is instantaneous after Co dissolution. Then, the proposed mechanism is shown in Figure III-23.

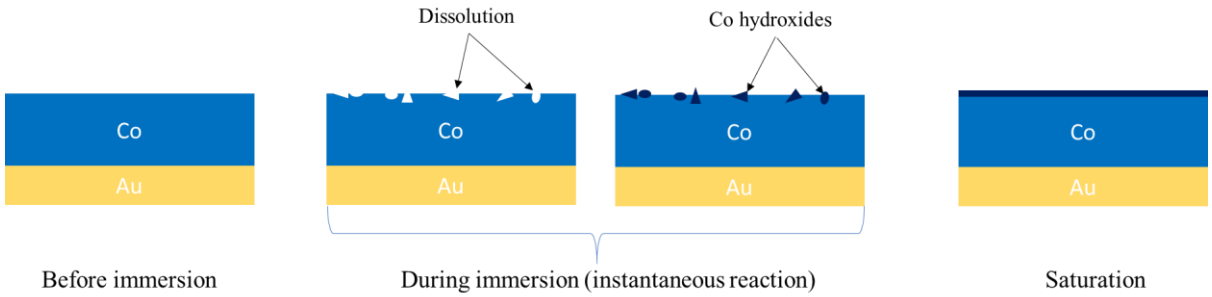

Figure III-23. *Proposed mechanism of Co hydroxides formation.*

According to the cobalt Pourbaix diagram in Figure III-24, at pH10 the species formed is most probably cobalt hydroxide ($CoOH_2$).

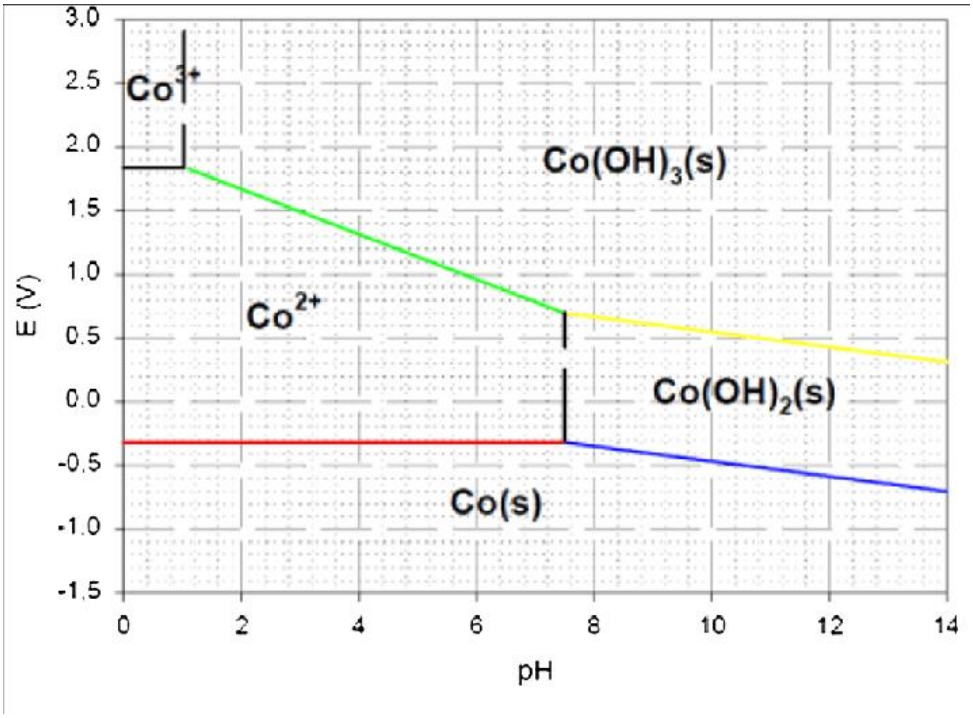

Figure III-24. *Cobalt Pourbaix diagram.*

The mass of the formed film is approximately 25 µg. XPS allowed the identification of chemical composition change after immersion. A depth profiling analysis is performed using Ar^+ sputtering on both non immersed and immersed Co film to compare their chemical composition. Figure III-25 shows the depth profiles of non-immersed cobalt (as deposited) and immersed cobalt in solution C (pH=10, saturated O_2).

Figure III-25 shows that for the first 200 seconds of etching time, the cobalt amount is higher in non-immersed cobalt film compared to the immersed cobalt. However, the oxygen amount is higher in the immersed cobalt film. These results confirm that the composition is different in both samples. The second interesting difference concern the gold amount. For the as-deposited cobalt, the apparition of gold is noticed after 400 seconds of sputtering. However, the gold apparition in the immersed cobalt is obtained after 600 seconds of etching. Supposing that the etching rate is almost the same on both samples, this difference in etching time is related only to the thickness difference.

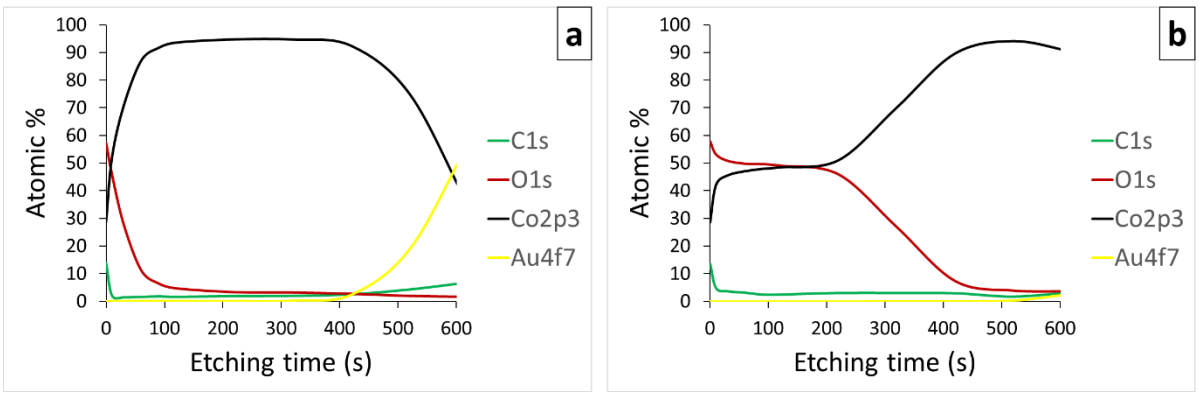

Figure III-25. *XPS depth profile of as-deposited cobalt (a) and cobalt immersed in solution C (b).*

The carbon amount is a little bit higher in the immersed cobalt. This difference is supposed to be related to the carbonate's presence in solution C. This result is confirmed by C1s spectra.

Co2p high-resolution spectra show that for the immersed cobalt film, the metallic cobalt contribution appears only after 200 s of sputtering (see Figure III-26). However, this contribution is obtained for all levels from the beginning of the non-immersed sample.

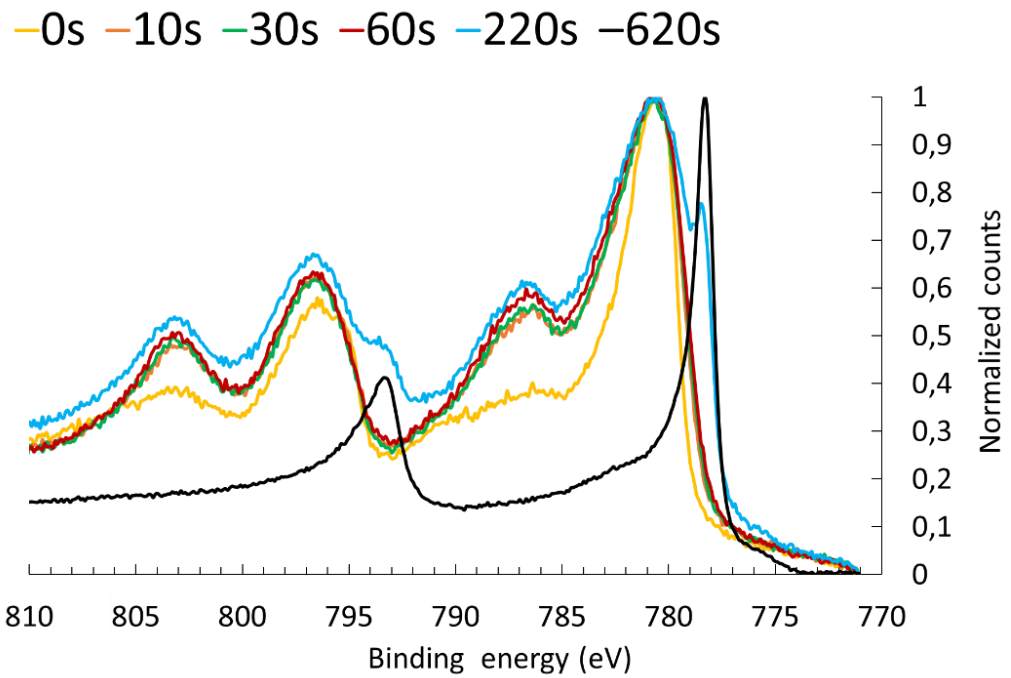

Figure III-26. *Co2p depth profiling of the immersed cobalt sample in solution C.*

EQCM results demonstrate the dissolution of cobalt film when immersed in acidic media. These results should be taken into consideration as the cobalt seed layer is only 3 nm in thickness. The operator should not expose the cobalt seed layer in non-de-aerated acidic chemistry for more than 1 minute. Knowing that it is complicated to obtain a fully de-aerated solution, especially in the industry where large solution volumes are manipulated. The operators should carefully control the immersion time during electroplating. XPS results also confirm the hypothesis of new species' formation when cobalt film is immersed in an alkaline solution saturated with dissolved oxygen.

III.5 Conclusion

- The annealing effect on cobalt film composition is inspected by XPS, the outcomes are:
  - Annealing reduces oxygen amount in the deposited cobalt film.
  - Annealing improves the cobalt film by decreasing its electrical resistivity.
- The impact of electrolyte pH on cobalt film is evaluated, the results are:
  - The oxygen amount increases by four times in pH=4.7 compared to pH=2.2 and 2.3. This amount of oxygen can be associated with cobalt hydroxide.
- Cobalt film reactivity in acidic and alkaline solutions is investigated in different conditions (O_2 saturated and de-aerated bath). Using EQCM and XPS it was found that:
  - Cobalt is dissolved in Cowave chemistry. Thus the time of immersion before process application should be considered.
  - It seems that the dissolution is not uniform, or the deposition thickness is not uniformly distributed.
  - Cobalt is dissolved in acidic buffers due to dissolved oxygen presence.
  - The dissolution rate in acidic media is considerable (from 0.5 to 3.2 nm/min)
  - The immersion of cobalt film in O2 saturated alkaline buffer (pH=10) results in the formation of hydroxides species. This formed film reaches saturation after 10 minutes of immersion. However, the cobalt mass remains unchanged in the alkaline de-aerated solution.
  - XPS depth profiling shows that Co hydroxides can be formed after immersion in alkaline O_2 saturated solution.
- Cobalt film reactivity toward air exposure is assessed; the main results are:
  - Co2p XPS results showed a huge oxide contribution only after 30 seconds of air exposure.
  - The cobalt layer oxidizes quasi instantaneously.
  - The cobalt-oxide thickness seems to be steady after 5.4 days, and its thickness is ultra-thin (nm range)
  - We think that cobalt coupon storage under N_2 does not prevent cobalt oxide formation but prevents only carbon contamination. This is because of the queue time between taking out the cobalt from the electrolyte and storing it is superior to 30 seconds.

III.6 References

[1] J. Kelly *et al.*, "Annealing and Impurity Effects in Co Thin Films for MOL Contact and BEOL Metallization," *J. Electrochem. Soc.*, vol. 166, no. 1, pp. D3100–D3109, 2019, doi: 10.1149/2.0151901jes.

[2] S. Ali and M. Salim, "Effect of pH at Early Formed Structures in Cobalt Electrodeposition," *Asian J. Chem.*, vol. 25, no. 8, pp. 4137–4140, 2013, doi: 10.14233/ajchem.2013.11031.

[3] J. J. Kelly, C. Tian, and A. C. West, "Leveling and Microstructural Effects of Additives for Copper Electrodeposition," *J. Electrochem. Soc.*, vol. 146, no. 7, pp. 2540–2545, Jul. 1999, doi: 10.1149/1.1391968.

[4] T. P. Moffat, D. Wheeler, and D. Josell, "Electrodeposition of Copper in the SPS-PEG-Cl Additive System," *J. Electrochem. Soc.*, vol. 151, no. 4, p. C262, 2004, doi: 10.1149/1.1651530.

[5] P. M. Vereecken, R. A. Binstead, H. Deligianni, and P. C. Andricacos, "The chemistry of additives in damascene copper plating," *IBM J. Res. Dev.*, vol. 49, no. 1, pp. 3–18, Jan. 2005, doi: 10.1147/rd.491.0003.

[6] L. Religieux, P. Blondeau, and D. Suhr, "Copper Electrodeposition Bath Containing an Electrochemically Inert Cation," Jun. 18, 2015.

[7] V. Mevellec, D. Suhr, and L. RELIGIEUX, "Electrolyte and method for electrodepositing copper onto a barrier layer," WO2014044942A1, Mar. 27, 2014.

[8] J. Gonzalez and H. Monchoix, "Method and Compositions for Direct Copper Plating and Filling to Form Interconnects in the Fabrication of Semiconductor Devices," Aug. 30, 2007.

[9] M. Başkan, M. Erdoğan, I. Karakaya, " Effects of pH and Cobalt Concentration on the Properties of Nickel – Cobalt Alloy Plating" 18th International Metallurgy & Materials Congress, 2016.

[10] Q. T. Le, E. Kesters, Y. Akanishi, M. H. van der Veen, A. Mizutani, and F. Holsteyns, "Effect of Cleaning Chemistries on Cobalt: Surface Chemistries and Electrical Characterization," *Solid State Phenomena*, 2018.

[11] M. C. Biesinger, B. P. Payne, A. P. Grosvenor, L. W. M. Lau, A. R. Gerson, and R. St. C. Smart, "Resolving surface chemical states in XPS analysis of first row transition metals, oxides and hydroxides: Cr, Mn, Fe, Co and Ni," *Appl. Surf. Sci.*, vol. 257, no. 7, pp. 2717–2730, Jan. 2011, doi: 10.1016/j.apsusc.2010.10.051.

[12] Finn Reikowski, Fouad Maroun, Ivan Pacheco, Tim Wiegmann, Philippe Allongue, Jochim Stettner, and Olaf M. Magnussen "Operando Surface X-ray Diffraction Studies of Structurally Defined Co3O4 and CoOOH Thin Films during Oxygen Evolution " American Chemical Society, 2019.

[13] J. S. Fang, L. Y. Lin, C. L. Wu, Y. L. Cheng, and G. S. Chen, "Effects of Additives on Electrochemical Growth of Cu Film on Co/SiO2/Si Substrate by Alternating Underpotential Deposition of Pb and Surface-Limited Redox Replacement by Cu," *J. Electron. Mater.*, vol. 46, no. 11, pp. 6677–6684, Nov. 2017, doi: 10.1007/s11664-017-5692-5.

[14] B. D. Anderson and J. B. Tracy, "Nanoparticle conversion chemistry: Kirkendall effect, galvanic exchange, and anion exchange," *Nanoscale*, vol. 6, no. 21, pp. 12195–12216, 2014, doi: 10.1039/C4NR02025A.

[15] K. Hamaguchi, T. Tsuchiyama, and J. Matsushita, "Oxidation of Tantalum Nitride," *Mater. Sci. Forum*, vol. 761, pp. 125–129, Jul. 2013, doi: 10.4028/www.scientific.net/MSF.761.125

[16] H. Patel and R. T. Vashi, “Chapter 2 - Characterization of Textile Wastewater,” in *Characterization and Treatment of Textile Wastewater*, H. Patel and R. T. Vashi, Eds. Boston: Elsevier, 2015, pp. 21–71.

General Conclusion

In this thesis, the first objective was to study cobalt electrodeposition using Cowave acidic chemistry to understand its mechanism for interconnection applications. For this purpose, we used in this study a three-electrode electrochemical cell composed of a platinum counter electrode, a gold working electrode and a silver chloride reference electrode. The second objective was to study thin cobalt films' reactivity to assess the cobalt seed layers' behavior towards air and chemistry.

In this thesis work, we focused on four main points: i) understanding of the cobalt electrodeposition process and the existing parasitic reactions by being sure of the reliability of the electrochemical measurements, ii) effect of concentration, pH, temperature, and additive on cobalt electrodeposition, iii) effect of air exposure on the reactivity of cobalt deposited film, iiii) effect of immersion in chemistries on thin cobalt films.

Added values

The first approach adopted consists of an electrochemical investigation of cobalt using voltammetric techniques. The electrochemical investigation of this metal appears to be complicated due to the presence of parasitic reactions. Therefore, we have set up a new measurement protocol combining electrochemistry and quartz microbalance to assess the cobalt electrodeposition process.

Cyclic voltammetry measurements conducted on a gold working electrode in Cowave acidic solution revealed a maximum current efficiency of 75%. Thus, the remained percentage of 25% is related to the parasitic reaction. This phenomenon is confirmed by electrochemical quartz crystal microbalance and these parasitic reactions are identified as the hydrogen evolution reaction due to proton reduction and H_2O reduction. During cobalt electrodeposition, bubbles are noticed at the interface of the working electrode. These bubbles seem to behave as insulators, which impact the current collection on the working electrode and can also impact the cobalt deposited physico-chemistry. It is supposed that these bubbles are H_2 bubbles and they can be associated with hydrogen evolution reaction.

XPS investigation on cobalt films deposited in different electrolyte pH’s shows a higher amount of oxygen at higher pH’s. This phenomenon is probably due to the formation of cobalt hydroxides at higher pHs and maybe because of H_2O reduction that increases local pH. Consequently, it is recommended not to exceed a pH of 3.

We have shown through using the electrochemical quartz crystal microbalance that we can control the thickness and the mass during cobalt electrodeposition. This will give us the possibility to deposit a nanometric cobalt layers with a minimal thickness deviation.

The work on the reactivity of the cobalt film is investigated by using XPS. An approach is developed by using spectrometer entry to expose Cobalt film to air within controlled times. In this study, the Co2p and O1s spectra are explored to determine the amount of oxygen evolution as a function of air-exposure. It was found that in only 30 seconds of air-exposure, a huge native oxide is formed and its thickness nearly reaches saturation. This result puts into question the storage of cobalt coupons under nitrogen, which is supposed to protect the cobalt from oxidizing. However, according to this study, it only serves to protect against carbon contamination.

The electrochemical quartz crystal microbalance allowed us to determine the different data concerning the deposition rate and thickness. By depositing a controlled nanometric cobalt thickness on a gold working electrode, a study of immersion impact on cobalt film behavior is investigated. We used three solutions to simulate the different chemistries used in microelectronic (alkaline and two acidic chemistries). For each solution two oxygen concentration conditions are used, a fully saturated dissolved oxygen, and a de-aerated solution. It was found that cobalt is etched in acidic chemistry with a dissolution rate of approximately 3 nm/min. These results require us to be very careful about the time of immersion of the cobalt seed layers before starting the electrodeposition process. On the other side, new film growth is noticed during the immersion of cobalt film in alkaline saturated oxygen solution. The formed film can be associated with Co hydroxides.

Outlooks

These results allow us to consider many perspectives on the scientific and technical aspects of the cobalt electrodeposition. Indeed, questions on whether the formed hydrogen bubbles during electroplating impact the cobalt film and can cause so-called hydrogen embrittlement or no. Further studies on the quantification of hydrogen in cobalt are necessary.

In this work, we have studied the electrochemical impact of the additive on cobalt electroplating; it is interesting to perform a study on cobalt nucleation and growth at different additive concentrations. It is also interesting to study the impact of additive on microstructure of the electrodeposited Co film.

Extensive work has been done on the dissolution of cobalt thin film in acidic chemistry. It was found that the dissolution is higher at the center of the working electrode. An EDX study of the surface of deposited cobalt may be of interest to evaluate the thickness distribution by calculating the ratio Co/Au in different points of the working electrode as described in picture.

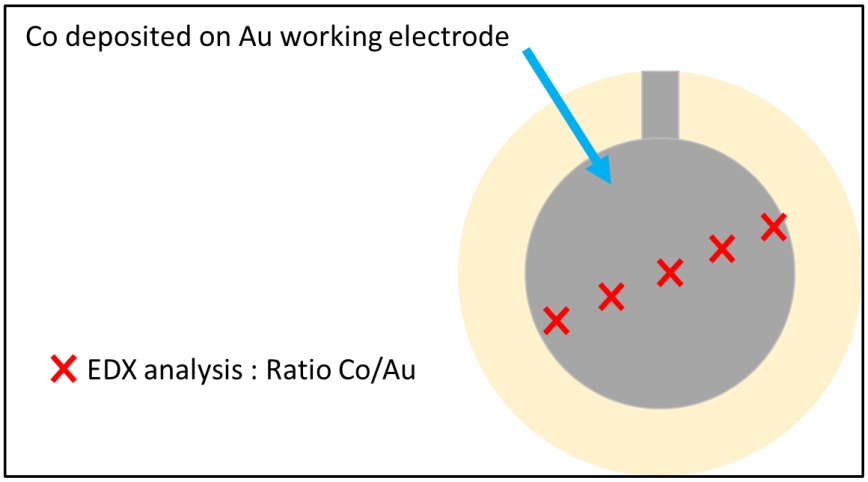

List of figures

Figure I-1. Complementary Metal-Oxyde-Semiconductor (CMOS) cross section diagram. S: source, G: gate, D: drain..... 20
Figure I-2. Evolution of MOS transistor counts over the years [credit: Licensed under CC-BY the author Max Roser]..... 21
Figure I-3. CMOS global structure. 23
Figure I-4. Metallization layers in interconnections. 24
Figure I-5. Single and dual damascene process. 25
Figure I-6. Dual damascene patterning - Via first approach. 26
Figure I-7. Sidewall electron scattering in copper wires (CD < 55 nm). 28
Figure I-8. Failure mechanisms for Cu interconnects. 29
Figure I-9. Materials comparison for narrow and wide features made by Aplied Materials. . 30
Figure I-10. Copper vs cobalt line resistivity as a function of CD, (Applied Materials). 30
Figure I-11. Cobalt process cycle..... 32
Figure I-12. Co/CoO and Cu/Cu2O Ellingham diagram with corrosion pressure equilibrium. 33
Figure I-13. Pourbaix diagram of Cu (left) and Co (right) showing stability and instability domains in water. 34
Figure I-14. Two electrodes electrochemical cell used in industry. 34
Figure I-15. Factors affecting current. 35
Figure I-16. Major current waveforms used in electrodeposition, (A) direct current (B) rectangular pulse current and (C) periodic reversed pulse current..... 38
Figure I-17. Concentration profile at the cathode for pulse plating conditions: \delta_P, pulsating diffusion layer thickness; \delta_S, stationary diffusion layer thickness; \delta_N, Nernst diffusion layer thickness [20]. 39
Figure I-18. Nucleation and growth diagram during electrodeposition 39
Figure I-19. Molecular structures of three accelerators: (a) ZPS, (b) SPS, and (c) MPS. 41
Figure I-20. Diagram of the adsorption behavior of additives [9]. 42
Figure I-21. Structure of a commercial leveler (Janus Green B). 42
Figure I-22. Different scenarios in electroplating. (a) faster deposition, (b) conformal deposition rate and (c) faster deposition rate at the bottom. 43
Figure I-23. Diffusion type in the bottom and the edges. 44
Figure I-24. Velocity variation between the top and the bottom of the via. 45

Figure II-1. Cyclic voltammogram for Au substrate at 20 mV/s in VMS Cowave bath 55
Figure II-2. Voltammograms on Au: in Cowave VMS (black) and HCl (red) at pH2.2, scan rate 20 $mV.s^{-1}$ 56
Figure II-3. Voltammogram of Au electrode: in Cowave VMS chemistry (black) and associated delta frequency variation (red), scan rate 20 $mV.s^{-1}$. 57
Figure II-4. Mass change of applied potentials vs. AgCl on Au working electrode in Cowave VMS solution. 58
Figure II-5. Thickness evolution at applied potentials vs AgCl on Au working electrode in Cowave VMS. 59
Figure II-6. Cyclic voltammogram of Au electrode in Cowave VMS 0.04 M (black), 0.02 M (blue), 0.01 M (red), at a scan rate of 20 $mV.s^{-1}$ 61
Figure II-7. Current limiting of Co2+ vs cobalt concentration for Cyclic voltammogram of Au electrode in Cowave VMS 0.04 M (black), 0.02 M (blue), 0.01 M (red), at a scan rate of 20 $mV.s^{-1}$ 62
Figure II-8. Cobalt mass evolution vs time and associated potential on gold electrode in Cowave VMS 0.04 M (black), 0.02 M (blue), 0.01 M (red), scan rate = 20 $mV.s^{-1}$ 63
Figure II-9. Cyclic voltammograms on Au electrode at different vertex potentials at a sweep rate of 20 $mV.s^{-1}$ in Cowave VMS electrolyte solution. 64
Figure II-10. The applied process to study the reactions on Co working electrode. 66
Figure II-11. Cyclic voltammetry on deposited cobalt in Cowave VMS; scan rate 20 mV.s-1 : 1^{st} cycle (black), 10^{th} cycle (blue) and 18^{th} cycle (red). 67
Figure II-12. Corresponding mass change on cobalt working electrode in Cowave VMS, scan rate 20 mV. 68
Figure II-13. Applied process to investigate cobalt deposition on Au vs Co substrate. 69
Figure II-14. cyclic voltammogram in Cowave VMS on: gold in the 1st cycle (black), on cobalt in the 2nd cycle. 69
Figure II-15. Zoomed area of mass change in Cowave VMS: on gold working electrode vs cobalt working electrode. 70
Figure II-16. hydrogen evolution on gold substrate (left) and on deposited cobalt (right). ... 70
Figure II-17. The calculation method of cathodic and anodic charge Q_c and Q_a, simultaneously. 71
Figure II-18. Impact of applied potentials on current efficiency of cobalt reduction 73
Figure II-19. Hydrogen evolution reaction at -2.4 $V/_{Ag/AgCl}$ in Cowave VMS solution. 74
Figure II-20. j-t curves of cobalt deposition at different step potentials on gold electrode. ... 74

Figure II-21. Dimensionless curves of the cobalt deposition process on a gold working electrode: (a) -1.1 V; (b) -1.2 V and (c) -1.3 V/$_{Ag/AgCl}$. 76
Figure II-22. Cyclic voltammogram on Au working electrode in HCl at 12°C (black) and 16°C (red) at a scan rate of 50 mV.s^{-1}. 78
Figure III-1. Spectra of photo peaks and Auger line in the 680-1050 eV binding energy range; blue line is associated to an oxidized Co surface (after annealing) red line is associated to a pure metallic surface obtained after sufficient Ar^+ bombardment and elimination of oxide traces. 88
Figure III-2. Normalized Co2p spectra of the as-deposited (red) and the annealed sample (black) without Ar^+ sputtering (a) and after 30 seconds of Ar^+ sputtering (b). 89
Figure III-3. O1s spectra of the as-deposited and the annealed sample at t=30 s of Ar^+ sputtering. 90
Figure III-4. Co2p (a) and C1s (b) spectra of the as-deposited (red) and the annealed sample (black) after 30 seconds of Ar^+ sputtering. 91
Figure III-5. XRD analysis plan 91
Figure III-6. X-ray diffraction data for as-deposited and annealed Co films at 0° and 70° of analysis angle. 92
Figure III-7. Co2p spectra (a) and O1s spectra (b) of cobalt deposited at different pH values. 93
Figure III-8. O1s of the electrodeposited film at different pH baths after 60 seconds of Ar^+ sputtering. 94
Figure III-9. Substrate used for electroplating. 95
Figure III-10. Schematic of Co-Air reactivity study using XPS 400µm spot size. 96
Figure III-11. Co2p spectra evolution during Ar^+ sputtering. Spectra are obtained after different etching times. 97
Figure III-12. Co2p spectra at different air-exposure time. 97
Figure III-13. O1s spectra at different air-exposure time. 98
Figure III-14. Integration used for dipping in chemistries study. 100
Figure III-15. Diagram of chemistry dipping study of substrate A (3 nm Co seed) and B (10 nm Co seed) using XPS. 101
Figure III-16. Co2p XPS spectra of 5 seconds dipped Co seed in different chemistries: acidic copper solution (orange), acidic copper-less (green), alkaline copper solution (blue), and no treatment (black). 102

Figure III-17. Cu2p (left) and Ta4f (right) XPS spectra of 5 seconds dipped Co seed in different chemistries: acidic copper solution (orange), alkaline copper solution (blue), and no treatment (black)..... 104
Figure III-18. SEM image of TaN/Co stack after copper filling using electrochemical deposition with aveni® solution. Structures have an opening of 21nm after Co metallization and before copper plating. Image is obtained at a working distance of 2,6mm and with an accelerating voltage of 2kV. Magnification is at 100k. 105
Figure III-19. Dissolution of the cobalt film deposited in Cowave VMS (chronoamperometry -1.5 V for 1 minute) and dissolved at open circuit potential. 106
Figure III-20. Thickness change of cobalt film immersion in pH=1 solution in partially de-aerated solution (black) and in O_2 saturated solution (red). 108
Figure III-21. Thickness change of cobalt film immersion in pH=4 solution in partially de-aerated solution (black) and O_2 saturated solution (red). 109
Figure III-22. Mass change of cobalt film immersion in pH=10 solution in partially de-aerated solution (black) and O2 saturated solution (red). 110
Figure III-23. Proposed mechanism of Co hydroxides formation. 111
Figure III-24. Cobalt Pourbaix diagram. 111
Figure III-25. XPS depth profile of as-deposited cobalt (a) and cobalt immersed in solution C (b). 112
Figure III-26. Co2p depth profiling of the immersed cobalt sample in solution C. 113
Figure 0-1. Principle of the photoemission spectroscopy 129
Figure 0-2. XPS survey spectrum of electrodeposited cobalt layer on gold working electrode using Cowave VMS 130
Figure 0-3. Mini reactor set up. 131
Figure 0-4. Mini reactor head set-up. 132

List of Table

Table II-1. Diluted solutions 60
Table II-2. Anodic charges and current densities ratios of diluted solutions vs. Cowave VMS solution 62
Table II-3. Cathodic and anodic charges as a function of vertex potential 65
Table II-4. cathodic and anodic charge values 71
Table II-5. j_m and t_m of j-t curves for cobalt deposited at -1.1, -1.2, and -1.3 $V/_{Ag/AgCl}$. 75
Table III-1. XRD data of as-deposited and annealed cobalt film 92
Table III-2. Chemical composition of cobalt film at different air-exposure time 99
Table III-3. List of experimental tests performs during this study. 101
Table III-4. The atomic composition obtained from XPS survey for different treatment in chemistries. 103
Table III-5. Chemistries used for immersion tests. 107

List of Acronyms

Ag/AgCl silver/silver chloride reference electrode.

ALD atomic layer deposition.

AR aspect ratio between the depth and the width of a structure.

CA chronoamperometry.

CD critical dimension.

CE counter electrode.

CMP chemical mechanical polishing.

CVD chemical vapor deposition.

ECD electrochemical deposition.

EDX energy dispersive X-ray spectroscopy.

EM electromigration.

EQCM electrochemical quartz crystal microbalance.

IC integrated circuit.

PVD physical vapor deposition.

RDE rotating disk electrode.

RE reference electrode.

SEM scanning electron microscopy.

SPS bis(sodiumsulfopropyl)disulfide.

TSV through silicon via.

WE working electrode.

XPS X-ray photoelectron spectroscopy.

Appendix I Surface and bulk Characterization

X-ray Photoelectron Spectroscopy (XPS) is a non-destructive surface analysis technique that allows determining the chemical nature and composition of a material. This technique, which is based on the use of the photoelectric effect, was developed in the 1950s.

The XPS analysis results from the interaction of photons of hυ energy with electrons occupying well-defined energy in a material. By analyzing the energies of the ejected electrons (photoelectric effect), the corresponding binding energies can be identified. This technique of analysis thus makes it possible to identify all the elements of the periodic table except hydrogen and helium (because H and He do not possess core electrons). This is one of the reasons why the XPS has become one of the essential tools for carrying out rigorous studies in surface chemistry.

Principle of photoemission

Photoelectron spectrometry consists in sending a beam of photon X of energy hυ onto the surface of the sample to eject electrons from the core levels of the atoms. The ejected photoelectrons are collected and analyzed according to their kinetic energy using a hemispheric analyzer. The basic principle of the method is shown in Figure ***0-1*** and is based on the principle of conservation of incident photon energy which is expressed as follows

$$h\nu = E_c + E_l + \Phi_s$$

With :

hν : energy of the incident photon (h being Planck's constant and ν the frequency of the incident photon)

E_C: kinetic energy of the photoelectron

E_l: binding energy of the core level

Φ_s: output work

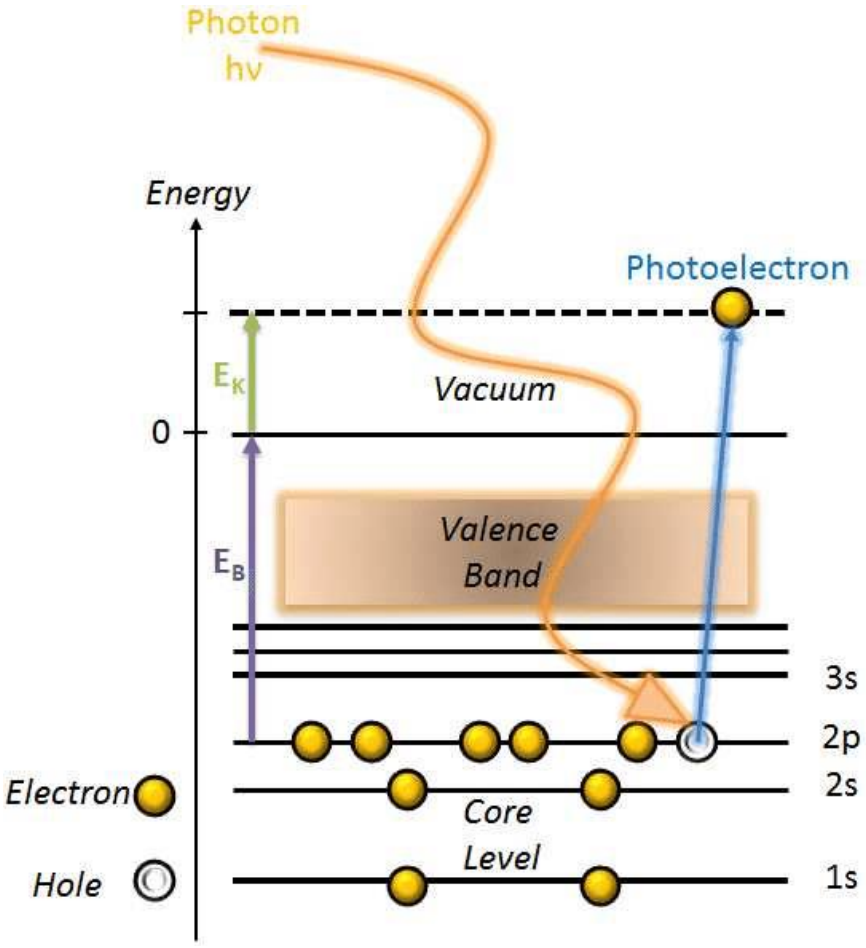

***Figure 0-1**. Principle of the photoemission spectroscopy*

The spectrometer's output work is intrinsic to each instrument and is generally determined by using reference materials such as copper, silver or gold. Thus, the knowledge of the output work Φs and the energy of the photon source hν allows accessing by the measurement of the kinetic energy Ec of a photoelectron, to the link energy EL of the corresponding electronic level.

The interest of analyzing the binding energy is that photoelectrons' binding energy is sensitive to the chemical environment of the atoms from which they come. At first glance, it increases with the degree of oxidation of the analyzed atom or material. It is then possible not only to determine the surface chemistry of the sample through the electronic structure and the chemical environment, but also to quantify the elements present in the different layers, to measure the thickness of the surface layers, and even to perform chemical profile reconstructions when the spectrometer allows it. This characterization technique is adapted to the sample's surface study since the mean free path of the photoelectrons emitted in the matter is very low (i.e. of the order of the nanometer). Thus, the depth of analysis is about 10 nm.

Spectra interpretation

The information contained in an XPS spectrum (survey) is numerous and varied, which requires extensive processing for the quantification of the elements. Figure ***0-2*** shows the raw XPS spectrum of a cobalt sample surface analysis. This spectrum shows several peaks of photoelectron emission, corresponding to the different electron levels of each of the elements present in the material and the extreme surface. The knowledge of the binding energies associated with each peak makes it possible to know the different atoms present.

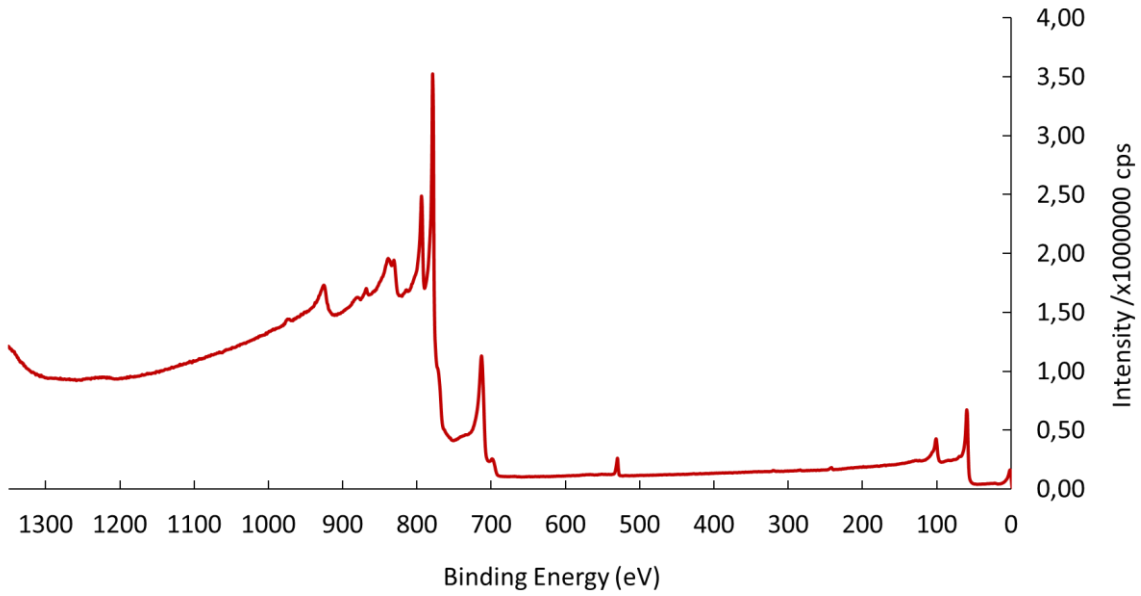

Figure 0-2*. XPS survey spectrum of electrodeposited cobalt layer on gold working electrode using Cowave VMS*

Appendix II Mini reactor set up

Substrate preparation

The coupons used for electroplating have a size of 33 x 33 mm and they are cut from 300mm diameter silicon wafers following an internal procedure. The substrate integrations used in this chapter are:

- Dielectric Tetraethyl Orthosilicate (TEOS) which easily converts to silicon dioxide upon the addition of water
- Thin barrier (1~3nm) TaN or TiN whose role is to control electromigration
- Ta or Ti layer to allow the adhesion of metal seed layer
- Cobalt metal seed layer with dimensions between 3 nm and 10 nm to assist electroplating and avoid discontinuities. The active electrochemical area is 7.54 cm^2.

Electrodeposition tool

After the coupons cutting procedure, the substrates are ready to be introduced into the plating bath. In our studies, the mini reactor contains 800ml of plating chemistry (see Figure ***0-3***). The mini reactor is composed of a tank, an anode (Ø=40mm) of copper or cobalt (it depends on the electrolyte bath). Co anode is used for Cowave to replenish cobalt ions consumed by electrodeposition. A vertical cathode rotation set up and a recirculation system with flowmeter are connected to minireactor.

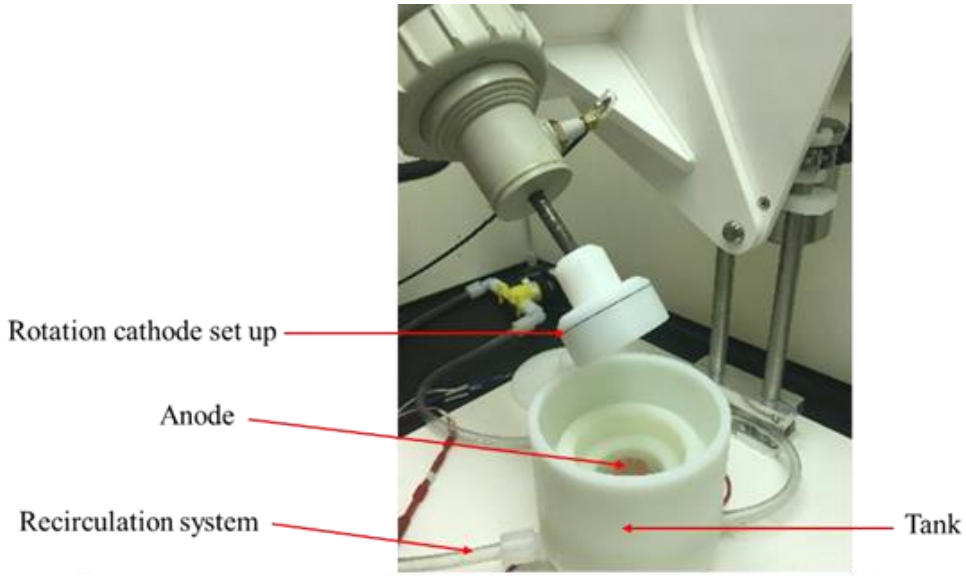

Figure 0-3*. Mini reactor set up.*

The mini-reactor head is made of 4 compartments: metallic support, a front-side and a back-side plastic heads and a sealing joint (see Figure ***0-4***).

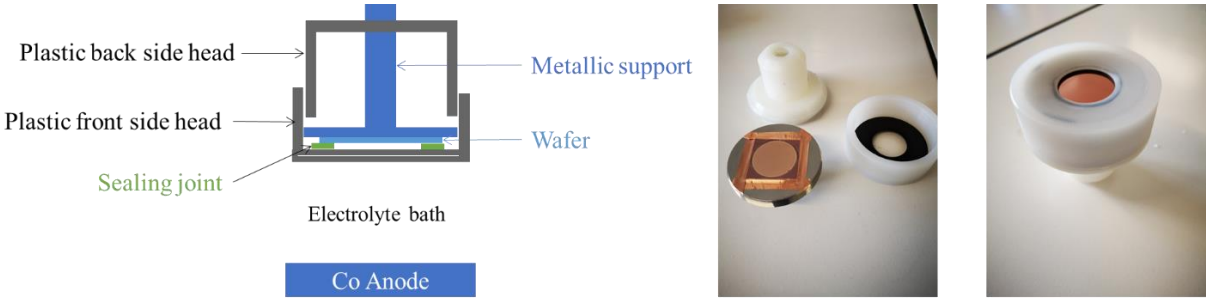

Figure 0-4. *Mini reactor head set-up.*

The coupon is connected electrically to the metallic support using four copper tape strips. Mini-reactor maintenance is performed every month by checking the conductivity of the anode and cathode connections using a multimeter and by controlling the rotation speed using a chronometer. Every three months, the repeatability is verified by processing 5 coupons with the same chemistry and compare the resistivity values and the thickness of the deposited film. The distance between the anode and cathode is an essential parameter; it should always be the same. It is also checked once a month.

Résumé

Cette thèse présente le dépôt électrochimique du cobalt comme une alternative au remplacement du cuivre dans le processus de double damascène dans les interconnexions en microélectronique. Le cobalt peut réduire la résistivité électrique des interconnexions dont les dimensions critiques (CD) sont inférieures à 15 nm. Dans les structures CD = 15 nm, le pourcentage du remplissage métallique est d'environ 33% avec du cuivre alors qu'il est de 87% pour le cobalt. Cette différence est liée à l'épaisseur des couches dites de barrière et du liner, qui sont essentielles pour contrôler l'électromigration et assurer l'adhésion de la couche de « seed » de cuivre dans la structure finale. Toutefois, lorsque l'on utilise du cobalt, la couche barrière peut être réduite tout en contrôlant l'électromigration en raison du libre parcours moyen plus faible du cobalt par rapport à celui du cuivre, et la couche de revêtement peut être éliminée. C'est dans ce contexte que s'inscrit la première partie de cette thèse qui est consacré à la théorie de la métallisation dans les interconnexions, elle comprend aussi les évolutions et les défis de la microélectronique avancée.

Dans la deuxième partie, cette thèse vise à étudier l'électrodéposition du cobalt en utilisant la chimie acide développée par la société aveni®. Cette étude repose sur les techniques de voltampérométrie cyclique pour maitriser le dépôt et la dissolution du cobalt sur une électrode de travail en or. Par la suite, l'impact de la concentration en Co2+ sur le processus de dépôt du cobalt est exploré en associant la voltamétrie cyclique à la microbalance électrochimique à cristal de quartz (EQCM). Cette étude révèle la présence du dégagement du dihydrogène lors de l'électrodéposition du cobalt en chimie acide. Ensuite, le rendement faradique de l'électrodépôt du cobalt et la nucléation du cobalt sur l'électrode d'or sont étudiés en chimie acide. Ces études nous ont permis de maitriser le processus d'électrodéposition et de contrôler à l'échelle nanométrique les épaisseurs de Co déposées. Pour déposer du cobalt dans des structures d'interconnexion, une fine couche « seed » de Co (~3 nm) est nécessaire pour assurer la conductivité électrique. Son rôle est essentiel car elle revêt la fonction de cathode dans le processus d'électrodéposition. Cette fine couche est néanmoins exposée à plusieurs interfaces, celle de l''air (avant immersion dans le bain électrolytique) et celle de la chimie acide avant l'électrodéposition de cobalt. Or, cette couche doit être continue afin d'assurer un remplissage homogène du cobalt, pour cela nous avons évaluer l'évolution de cette couche de cobalt.

Dans la troisième partie, cette thèse a pour but d'évaluer la réactivité du film de Co lorsqu'il est exposé à l'air, une stratégie a été mise au point utilisant la spectroscopie de photoélectrons par rayons X (XPS) et l'abrasion Ar+. Cette approche consiste à obtenir du cobalt métallique pur à l'intérieur de la chambre à ultravide de l'XPS en utilisant la pulvérisation de Ar+. Le film de cobalt obtenu sert d'échantillon de référence sans oxydes. Ensuite, le film de référence de cobalt est exposé à l'air pendant une courte durée et immédiatement analysé par XPS. La collecte des spectres XPS de Co2p à différents temps d'exposition à l'air permet de suivre la cinétique de la réoxydation du Co. Pour évaluer la réactivité du film de Co lorsqu'il est exposé aux solutions chimiques, plusieurs solutions tampons sont utilisées pour simuler les chimies utilisées en microélectronique (chimies 3 alcalines et acides). Cette étude requière au préalable le dépôt d'une couche nanométrique de cobalt par voltamétrie et EQCM. La stabilité du dit dépôt est suivi par EQCM au potentiel de circuit ouvert (OCP) dans les différents tampons dans deux conditions, désaérés et saturés en O2. Cette étude nous a permis d'une part de déterminer la vitesse de dissolution du cobalt en milieu acide et d'autre part de quantifier la formation d'hydroxydes de Co par XPS.

université PARIS-SACLAY | ÉCOLE DOCTORALE Interfaces: matériaux, systèmes, usages

Titre : Maitrise de l'électrodépôt de couches nanométriques de Cuivre et Cobalt pour lamétallisation des interconnexions en microélectronique

Mots clés : Electrodéposition, Cobalt, Interconnexion, Film mince, µ-balance, XPS.

Résumé : Cette thèse présente le dépôt électrochimique du cobalt comme une alternative au remplacement du cuivre dans le processus de double damascène dans les interconnexions en microélectronique. Le cobalt peut réduire la résistivité électrique des interconnexions dont les dimensions critiques (CD) sont inférieures à 15 nm. Dans les structures CD = 15 nm, le pourcentage du remplissage métallique est d'environ 33% avec du cuivre alors qu'il est de 87% pour le cobalt. Cette différence est liée à l'épaisseur des couches dites de barrière et du liner, qui sont essentielles pour contrôler l'électromigration et assurer l'adhésion de la couche de « seed » de cuivre dans la structure finale. Toutefois, lorsque l'on utilise du cobalt, la couche barrière peut être réduite tout en contrôlant l'électromigration en raison du libre parcours moyen plus faible du cobalt par rapport à celui du cuivre, et la couche de revêtement peut être éliminée. C'est dans ce contexte que s'inscrit **la première partie** de cette thèse qui est consacré à la théorie de la métallisation dans les interconnexions, elle comprend aussi les évolutions et les défis de la microélectronique avancée.

Dans la deuxième partie, cette thèse vise à étudier l'électrodéposition du cobalt en utilisant la chimie acide développée par la société aveni®. Cette étude repose sur les techniques de voltampérométrie cyclique pour maitriser le dépôt et la dissolution du cobalt sur une électrode de travail en or. Par la suite, l'impact de la concentration en Co2+ sur le processus de dépôt du cobalt est exploré en associant la voltamétrie cyclique à la microbalance électrochimique à cristal de quartz (EQCM). Cette étude révèle la présence du dégagement du dihydrogène lors de l'électrodéposition du cobalt en chimie acide. Ensuite, le rendement faradique de l'électrodépôt du cobalt et la nucléation du cobalt sur l'électrode d'or sont étudiés en chimie acide. Ces études nous ont permis de maitriser le processus d'électrodéposition et de contrôler à l'échelle nanométrique les épaisseurs de Co déposées.

Pour déposer du cobalt dans des structures d'interconnexion, une fine couche « seed » de Co (~3 nm) est nécessaire pour assurer la conductivité électrique. Son rôle est essentiel car elle revêt la fonction de cathode dans le processus d'électrodéposition. Cette fine couche est néanmoins exposée à plusieurs interfaces, celle de l''air (avant immersion dans le bain électrolytique) et celle de la chimie acide avant l'électrodéposition de cobalt. Or, cette couche doit être continue afin d'assurer un remplissage homogène du cobalt, pour cela nous avons évaluer l'évolution de cette couche de cobalt.

Dans la troisième partie, cette thèse a pour but d'évaluer la réactivité du film de Co lorsqu'il est exposé à l'air, une stratégie a été mise au point utilisant la spectroscopie de photoélectrons par rayons X (XPS) et l'abrasion Ar+. Cette approche consiste à obtenir du cobalt métallique pur à l'intérieur de la chambre à ultravide de l'XPS en utilisant la pulvérisation de Ar+. Le film de cobalt obtenu sert d'échantillon de référence sans oxydes. Ensuite, le film de référence de cobalt est exposé à l'air pendant une courte durée et immédiatement analysé par XPS. La collecte des spectres XPS de Co2p à différents temps d'exposition à l'air permet de suivre la cinétique de la réoxydation du Co. Pour évaluer la réactivité du film de Co lorsqu'il est exposé aux solutions chimiques, plusieurs solutions tampons sont utilisées pour simuler les chimies utilisées en microélectronique (chimies 3 alcalines et acides). Cette étude requière au préalable le dépôt d'une couche nanométrique de cobalt par voltamétrie et EQCM. La stabilité du dit dépôt est suivi par EQCM au potentiel de circuit ouvert (OCP) dans les différents tampons dans deux conditions, désaérés et saturés en O2. Cette étude nous a permis d'une part de déterminer la vitesse de dissolution du cobalt en milieu acide et d'autre part de quantifier la formation d'hydroxydes de Co par XPS..

Title : Control of nanometric copper and cobalt layers by electrodeposition for the metallization used in microelectronic interconnections

Keywords : Electroplating, Cobalt, Interconnections, Thin film, µ-balance, XPS

Abstract : In this thesis, the electrochemical deposition of cobalt is studied as an alternative to replacing copper in the dual-damascene process in microelectronic interconnections. Cobalt has the potential to reduce the electrical resistivity of interconnections whose critical dimensions (CD) are less than 15 nm. In CD = 15 nm structures, the percentage of metallic filling is about 33% with copper, while it is 87% for cobalt. This difference is related to the barrier and liner layers' thicknesses, which are essential to control electromigration and ensure the copper seed layer's adhesion in the final structure. However, when using cobalt, the barrier layer can be reduced while controlling electromigration due to the lower mean free path in cobalt than copper, and the liner layer can be skipped. That's the context of **the first part** of this thesis which is devoted to the theory of metallization in interconnections; it also includes the evolutions and challenges of advanced microelectronics.

In the second part, this thesis aims at studying the electrodeposition of cobalt using acidic chemistry developed by aveni®. This investigation consists at the first time of working on voltammetry techniques to take advantage of depositing and dissolving cobalt on a gold working electrode. Thereafter, the impact of Co2+ concentration on the cobalt deposition process is explored by associating cyclic voltammetry with the electrochemical quartz crystal microbalance (EQCM). This study reveals the presence of hydrogen evolution during the electroplating of cobalt in acid chemistry. Then, the faradic efficiency of the cobalt electrodeposition and the nucleation of cobalt on the gold electrode are studied in acid chemistry. These studies have allowed us to master the electroplating process and to control at the nanometer scale the thickness of deposited Co.

To deposit cobalt in interconnect structures; a Co thin seed layer (~3 nm) is required. Its role is essential because it acts as a cathode in the electroplating process. This thin layer is nevertheless exposed to several interfaces, that of air (before immersion in the electrolytic bath) and that of acid chemistry before cobalt electroplating. However, this layer must be continuous to ensure a homogeneous filling of the cobalt, for this reason we have evaluated the evolution of this cobalt layer.

In the third part, this thesis aims to assess the reactivity of the Co film when exposed to air, an engineered approach was developed using X-ray Photoelectron Spectroscopy (XPS) and Ar+ sputtering. This approach consists of obtaining pure metallic cobalt inside XPS ultra-high vacuum chamber using Ar+ sputtering. The obtained cobalt film will serve as a reference sample without oxides. Next, the reference Co film is exposed to air for a short time and immediately analyzed by XPS. The collection of Co2p spectra at different time air-exposure provides us the kinetic of reoxidation of Co, which is a key parameter. To evaluate the reactivity of the Co film when exposed to chemical solutions, several buffer solutions are used to simulate the chemistries used in microelectronics (alkaline and acidic chemistries). This study requires beforehand the deposition of a nanometric layer of cobalt by voltammetry and EQCM. The stability of the Co deposit is monitored by EQCM at open circuit potential (OCP) in different buffered solutions and under two conditions, deaerated and saturated in O2. This study allowed us, on the one hand to determine the dissolution rate of cobalt in acidic medium and on the other hand to quantify the formation of Co hydroxides by XPS.

Maison du doctorat de l'Université Paris-Saclay
2ème étage aile ouest, Ecole normale supérieure Paris-Saclay
4 avenue des Sciences,
91190 Gif sur Yvette, France